



Elettra Sincrotrone Trieste

X-ray Microscopy in photon transmission and emission, and multidisciplinary applications

Alessandra Gianoncelli

alessandra.gianoncelli@elettra.eu

- X-ray microscopes:
Full-field, STXM, projection
- Standard imaging technique and new advanced ones (CDI, Ptychography)
- Special attention to the TwinMic beamline (Elettra, Trieste)
- Multidisciplinary applications: life sciences, food science, environmental science, materials science, cultural heritage...

X-ray microscopy types

X-ray microscopy:
bridge between visible light microscopy and electron microscopies

Spatial resolution:

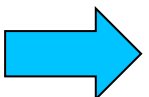
visible light microscopy < X-ray microscopy < electron microscopy

Air

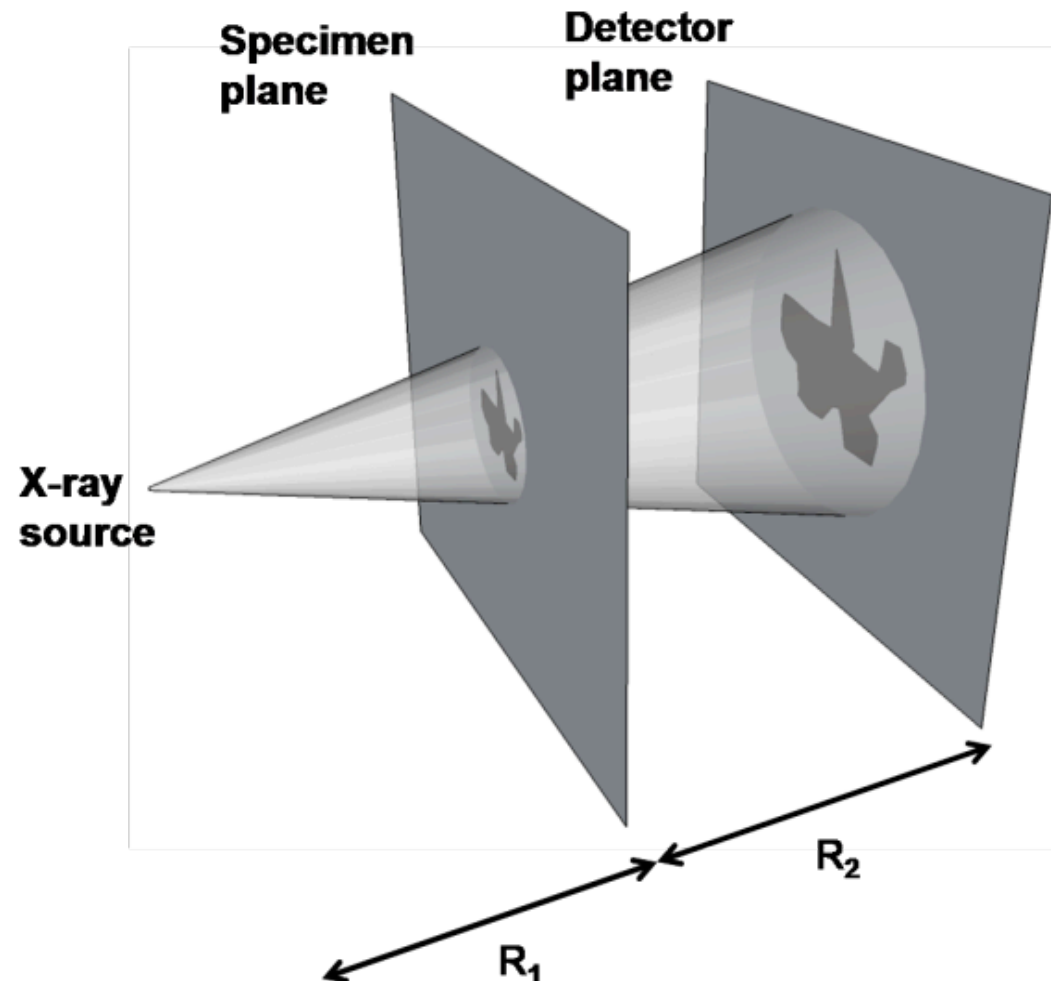
Vacuum
(or air)

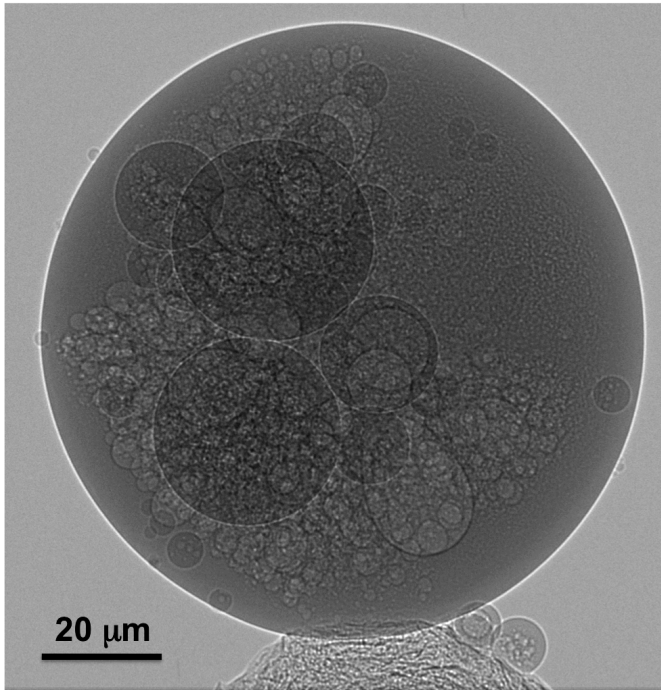
Vacuum

X-ray Microscopy vs Electron Microscopy:

- Easier sample preparation (no metalisation)
- Higher penetration depth of X-rays compared to electrons
  thicker samples can be analysed

Scheme of a projection microscope with the source to specimen plane distance R_1 and specimen to detector distance R_2





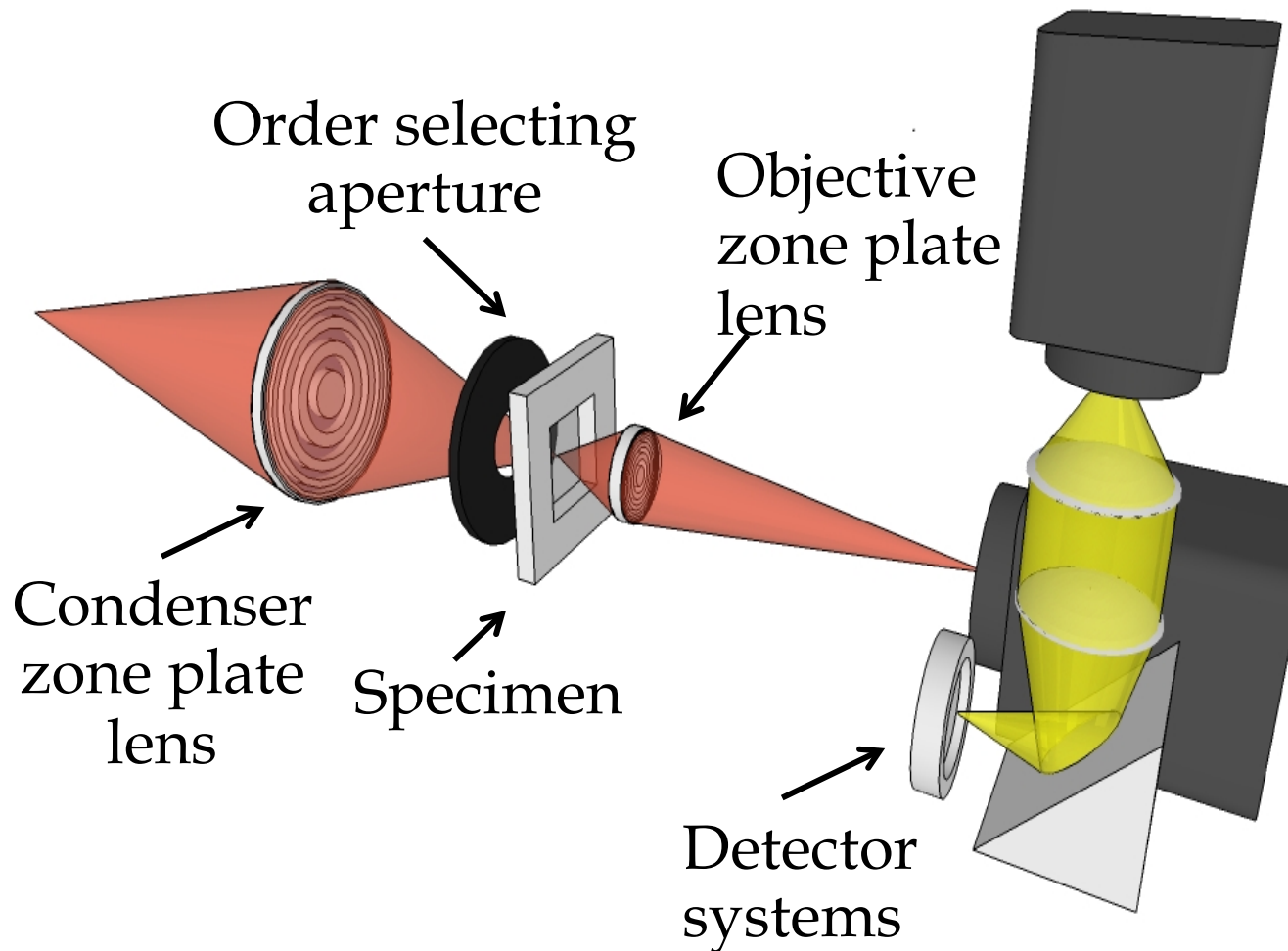
3D phase contrast dataset view, reconstructed cross section of part of a ceramisphere (projection X-ray microscope at the CSIRO, Australia).

The total collection time of the microtomogram was 10 h.

The diameter of the sphere is 110 μm

A state-of-the art instrument for projection microscopy, including phase-sensitive imaging and microtomography based on a converted scanning electron microscope, is reported for example by Mayo et al. (Mayo et al 2002; Mayo et al 2003).

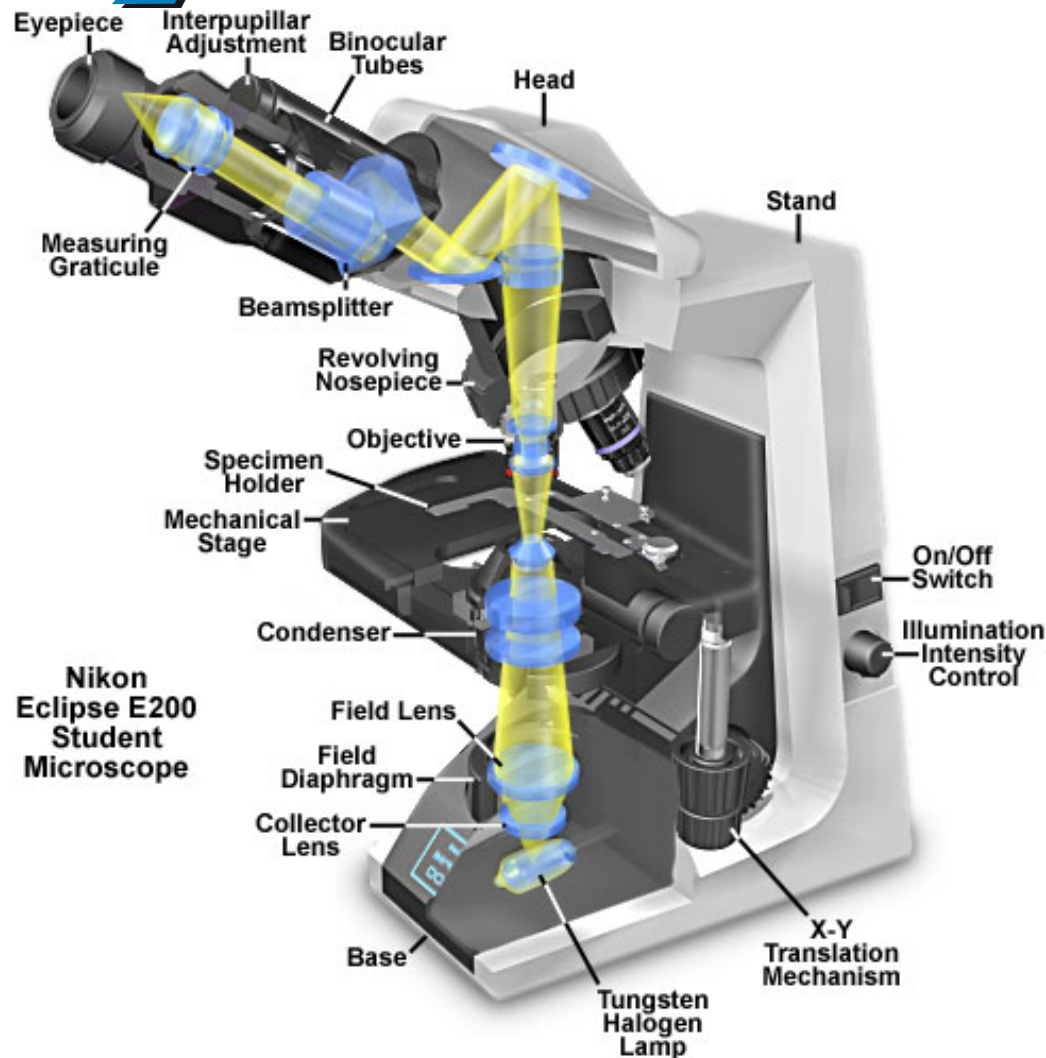
Full field Imaging mode



- Similar to conventional visible light microscope
- Analysis of morphology in transmission
- Fast imaging, dynamics, microtomography



Elettra
Sincrotrone
Trieste



Nikon
Eclipse E200
Student
Microscope

Full-field X-ray imaging or “one shot” X-ray image acquisition can be considered as the optical analogon to a visible light transmission microscope

BUT

Refractive index n is very close to unity and smaller than unity!!!

$$n = 1 - \delta(\lambda) - i\beta(\lambda) \lessapprox 1$$

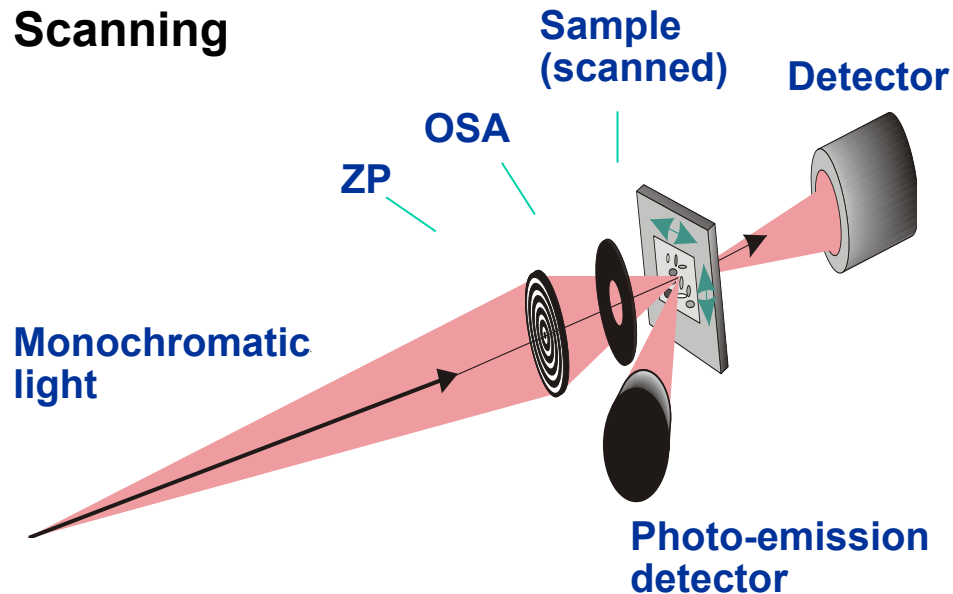
Cutaway diagram of a visible light microscope



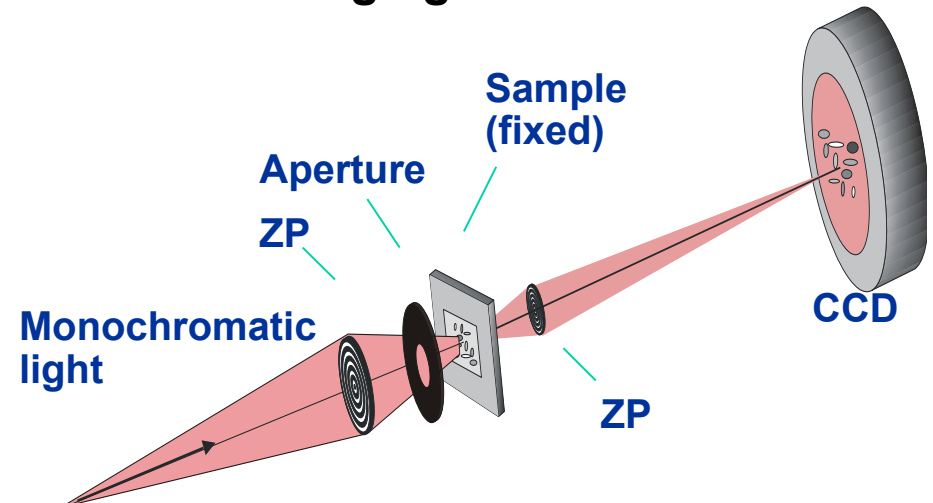
Elettra
Sincrotrone
Trieste

Background info: X-ray microscopy types

Scanning



Full-field imaging



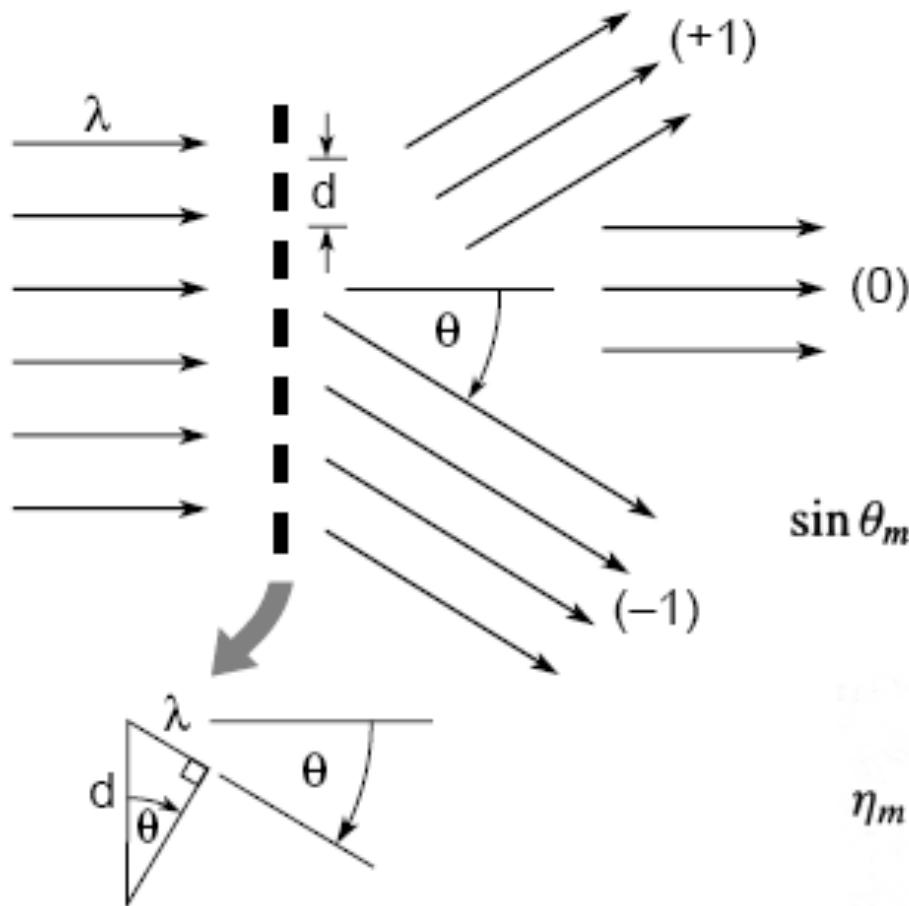
- + versatile detectors can run simultaneously;
- + easier optics set-up;
- long exposure time;
- complex electronics.

Ideal for spectromicroscopy

- + short exposure time;
- + higher resolution
- static system;
- complex optical alignment.

Ideal for dynamic studies
and tomography

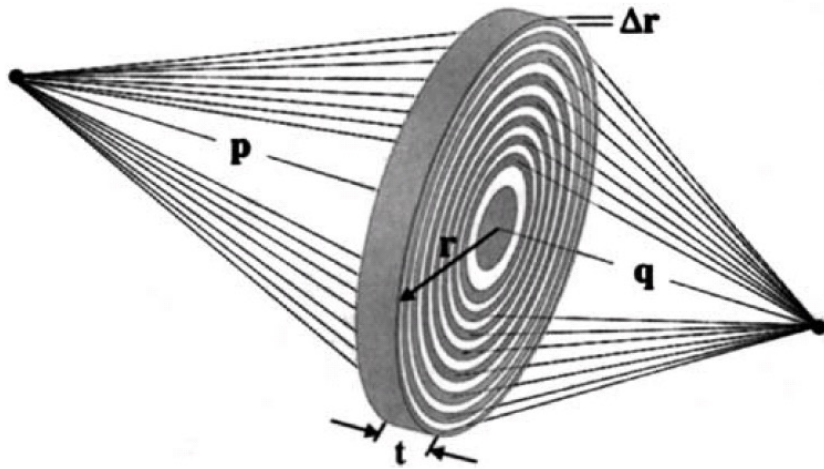
Background info: Diffraction by a grating



$$\sin \theta_m = \frac{m\lambda}{d} ; \quad m = 0, \pm 1, \pm 2, \pm 3, \dots \quad (9.2)$$

$$\eta_m = \begin{cases} \frac{1}{4} & m = 0 \\ 1/m^2\pi^2 & m \text{ odd} \\ 0 & m \text{ even} \end{cases} \quad (9.24)$$

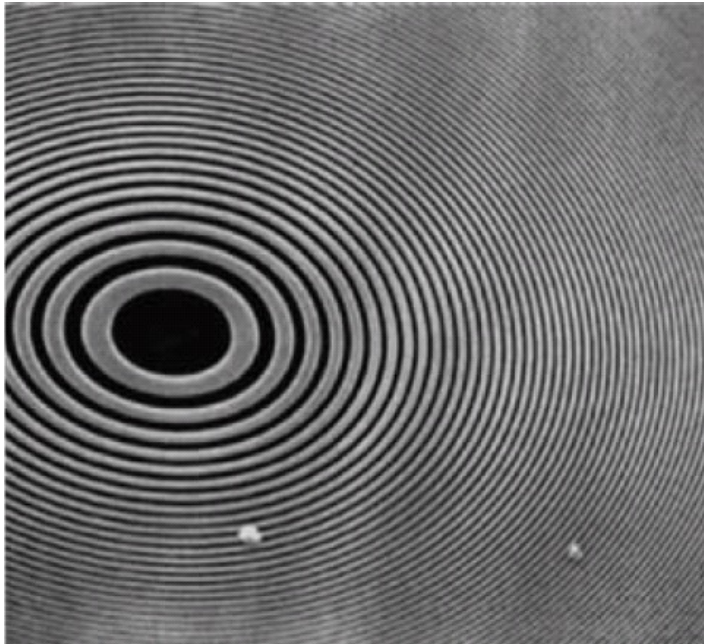
(50% absorbed)



Zone plate (ZP) is a circular diffraction grating with radially increasing line density

$$\frac{1}{f} = \frac{1}{p} + \frac{1}{q}$$

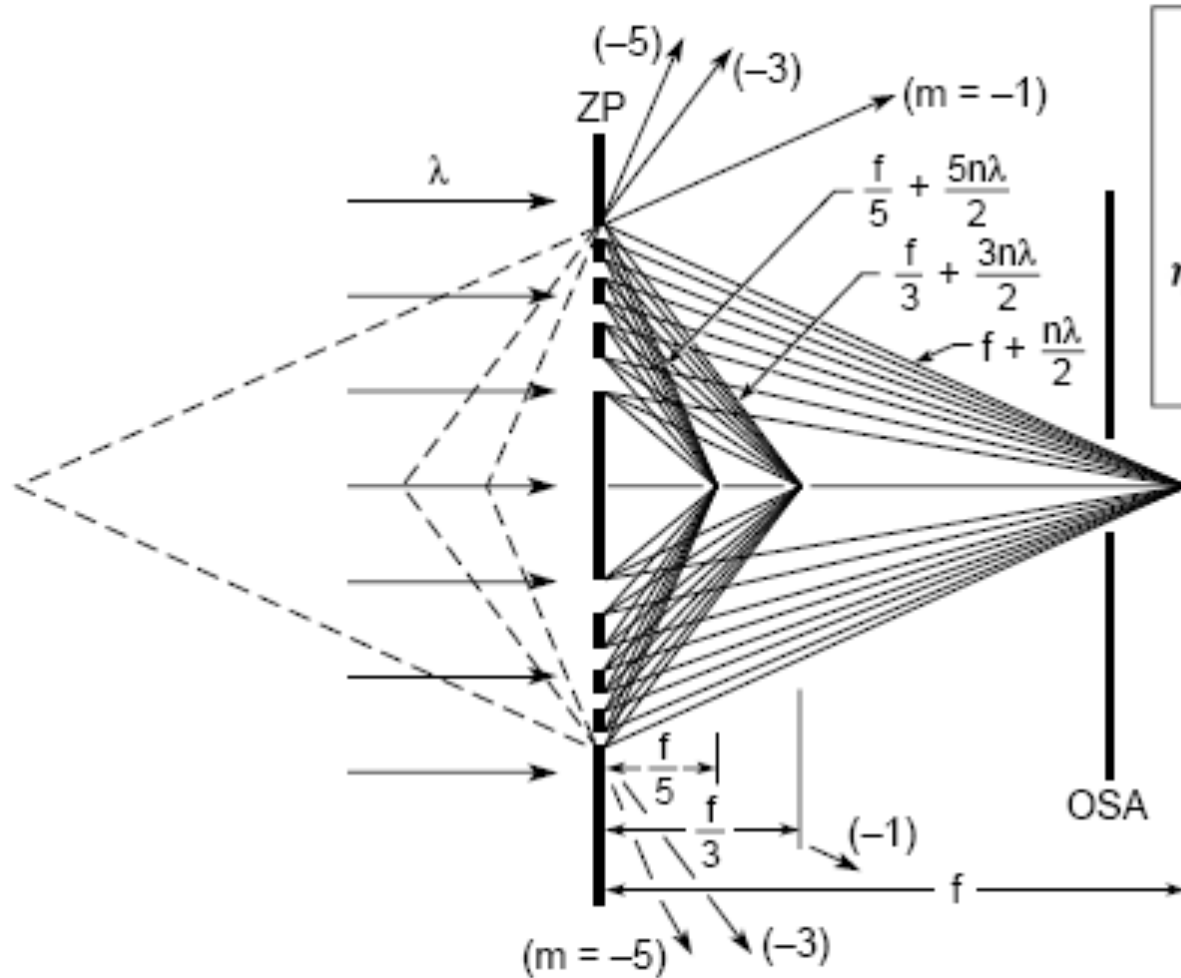
$$f = \frac{2r\Delta r}{\lambda}$$



$$NA \equiv \frac{r}{f} = \frac{\lambda}{2\Delta r}$$

$$\partial_{Rayleigh} = \frac{0.61\lambda}{NA} = 1.22\Delta r$$

Background info: Diffraction by a grating



$$r_n^2 \simeq mn\lambda f_m \quad (9.19)$$

$$\eta_m = \begin{cases} \frac{1}{4} & m = 0 \\ 1/m^2\pi^2 & m \text{ odd} \\ 0 & m \text{ even} \end{cases} \quad (9.24)$$

$$f_m = \frac{1}{m} \frac{r_N^2}{N\lambda}$$

$$f_m = \frac{1}{m} f_1$$

The complex refractive index

$$n = 1 - \frac{n_a r_e \lambda^2}{\pi} (f_1 + i f_2) \equiv 1 - \delta - i\beta \leq 1$$

**“Conventional refractive index”
describing phase change:**

$$\varphi(z) = \frac{2\pi}{\lambda} \delta z$$

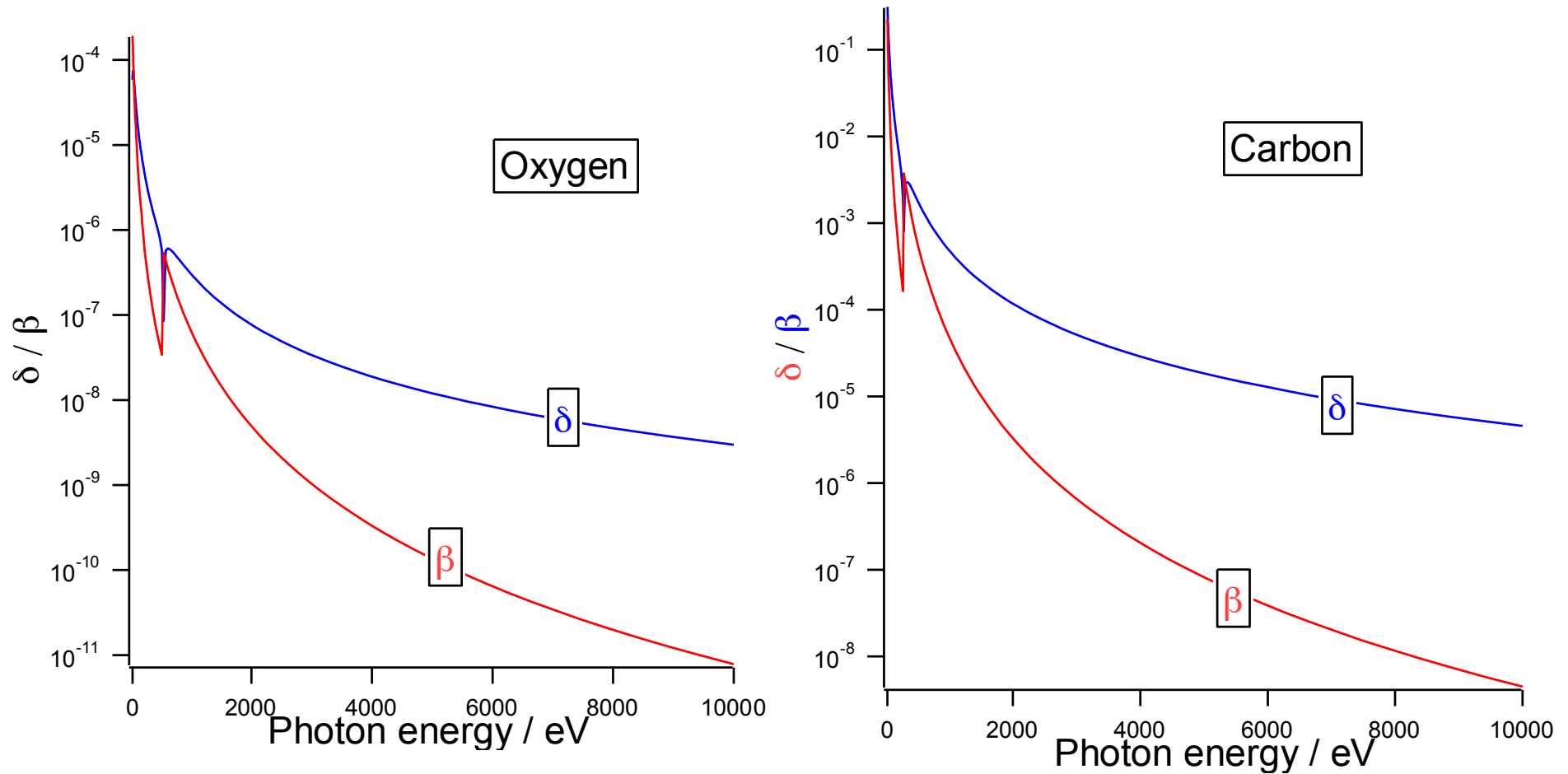
**Exploitation of phase contrasts
possible using X-rays ?
Lower radiation damage ?**

**Describing photoelectric
absorption with coefficient:**

$$\mu = \frac{4\pi}{\lambda} \beta$$

**Consequence:
Emission of Auger, photo-electrons
and fluorescence photons, but also
causes radiation damage
(energetic secondary electrons!)**

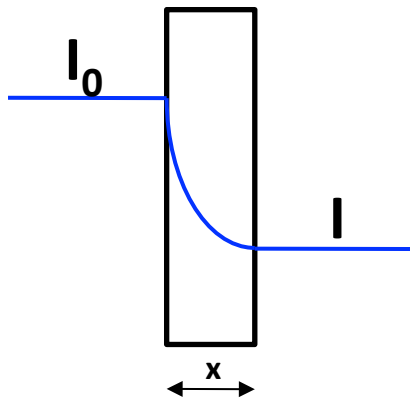
Delta versus beta



Delta is orders of magnitude larger !!!

Absorption mode

X-ray photons are selectively absorbed by the material according to its density and thickness
(ex. radiography)



Beer - Lambert' s law:

$$I = I_0 e^{-\mu x}$$

Phase contrast mode

Absorption can produce little contrast for light (transparent) materials or for materials with similar atomic number (similar attenuation factors).

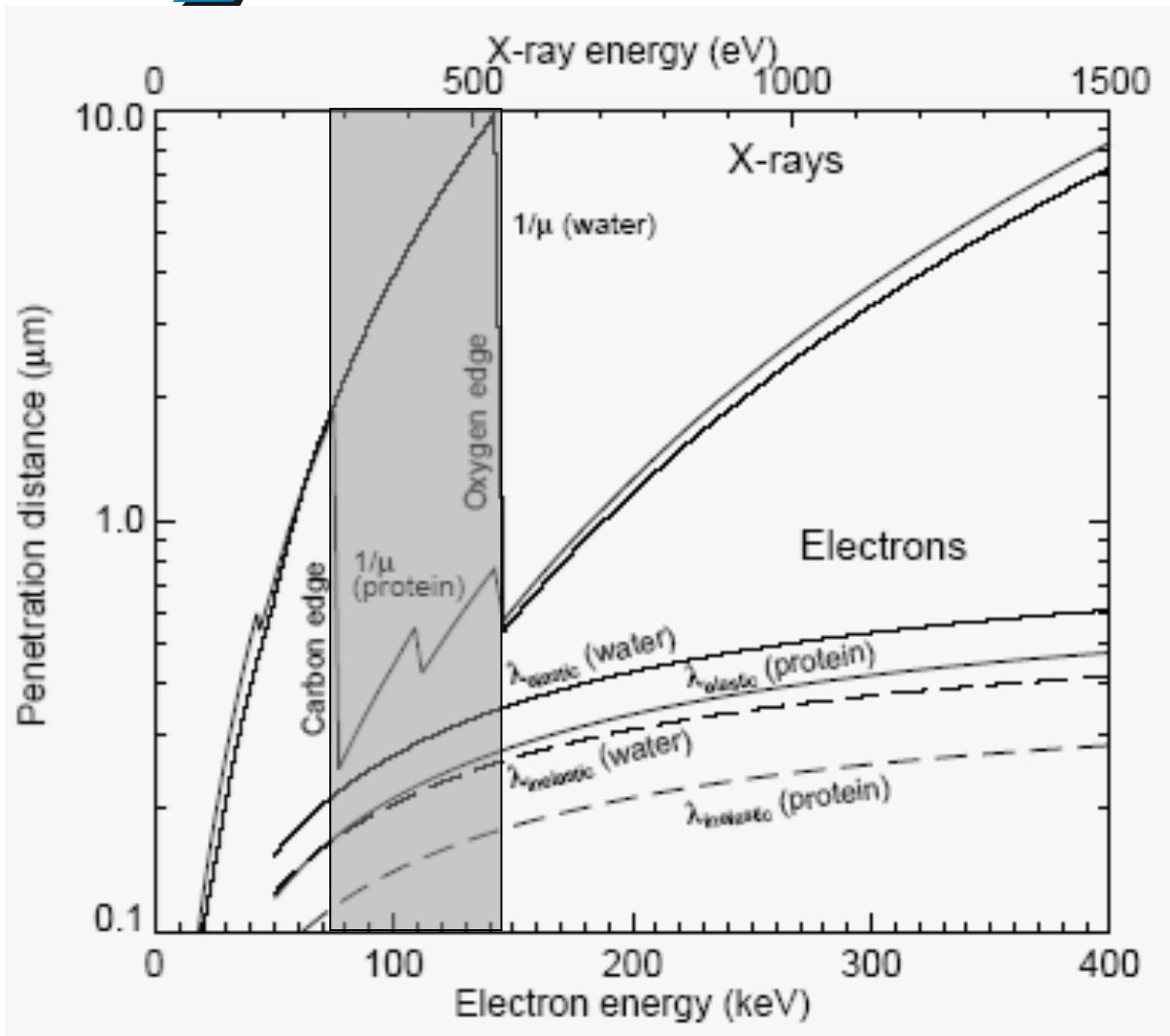
Moreover as the energy increases the contrast diminishes (absorption coefficient $\propto 1/E^3$)

Phase contrast is more sensitive to edges and borders in the sample

Contrast techniques using the real, phase-shifting part of the complex refractive index are in many cases superior to absorption contrast because:

- (i) the x-ray dose can be reduced dramatically
- (ii) the throughput is higher (the phase shift dominates the absorption in the x-ray regime)

Natural amplitude contrast between water and organic matter



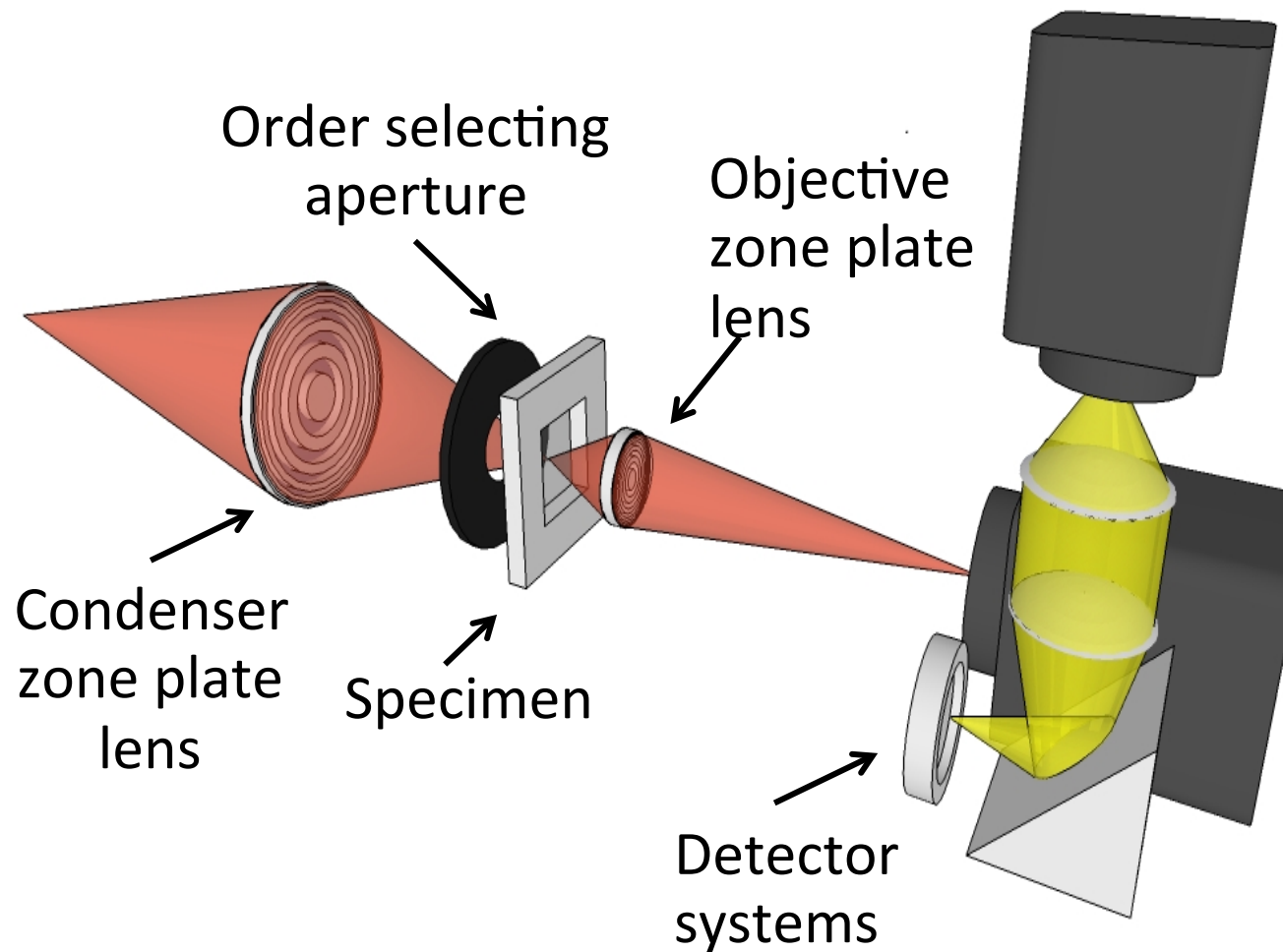
The “Water Window”:

Due to dramatic difference in the f_2 values of two materials, especially water and organic matter between the C and O K-absorption edges.

Note the penetration distance compared to electrons !!!

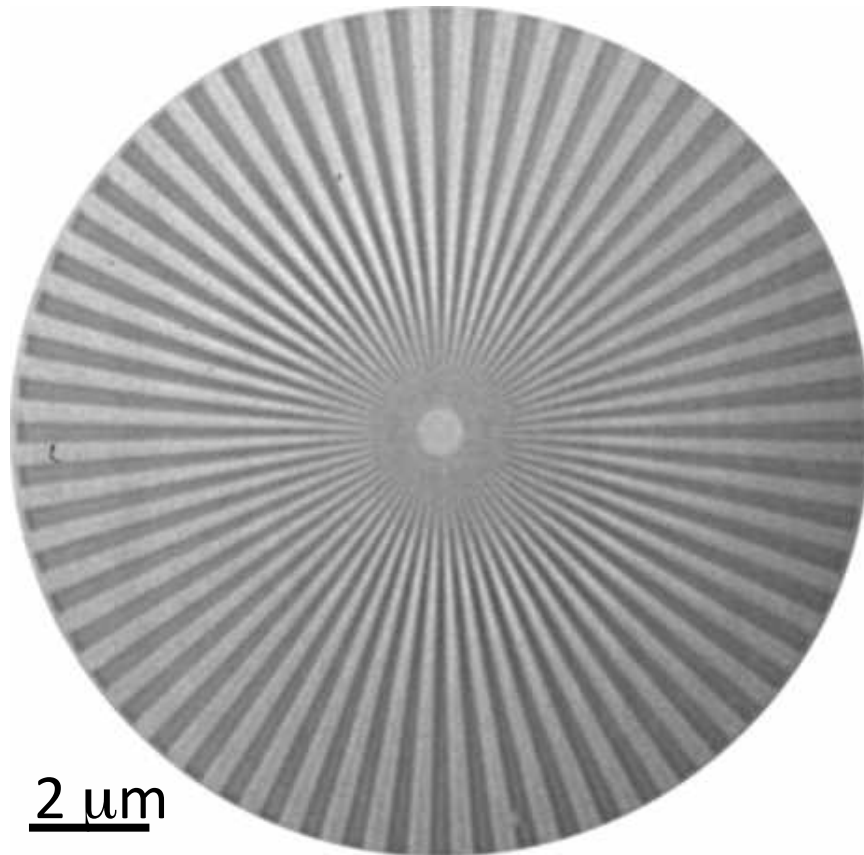
H. Wolter: *Spiegelsysteme streifenden Einfalls als abbildende Optiken fuer Roentgenstrahlen*, Ann. Phys. 10, 94-114, 286 (1952)

Full field Imaging mode

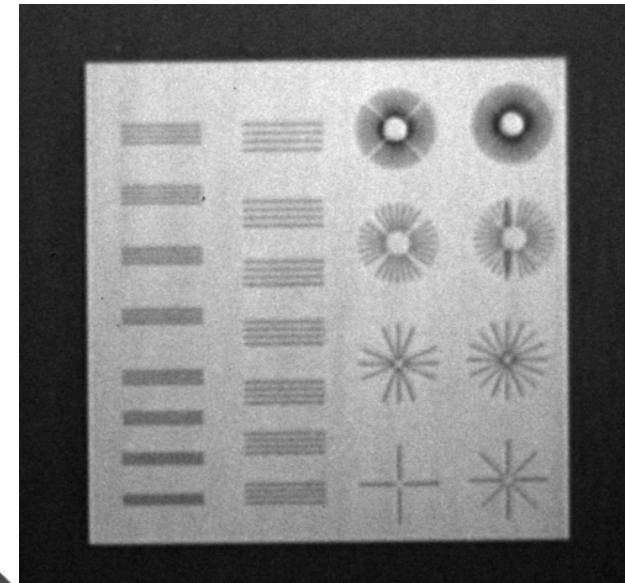


- Similar to conventional visible light microscope
- Analysis of morphology in transmission
- Fast imaging, dynamics, microtomography

Resolution tests in full-field imaging



ZP parameters:
110 μ m diameter
50 nm outer zones
 $f=3.2$ mm @ 720 eV
fabricated by TASC/
INFM



2 μ m

Test pattern with
30 nm features
(fabricated by
TASC/ INFM)

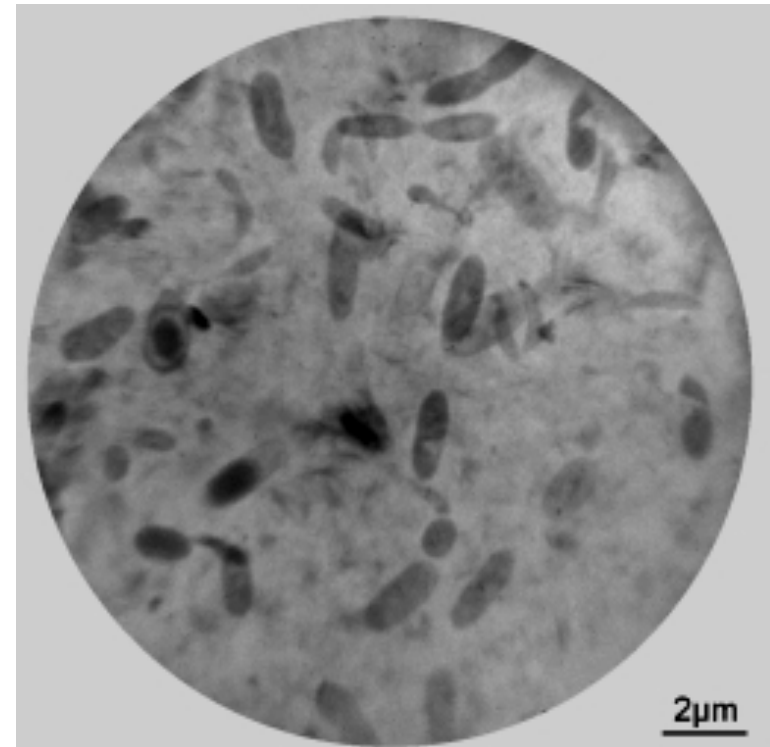
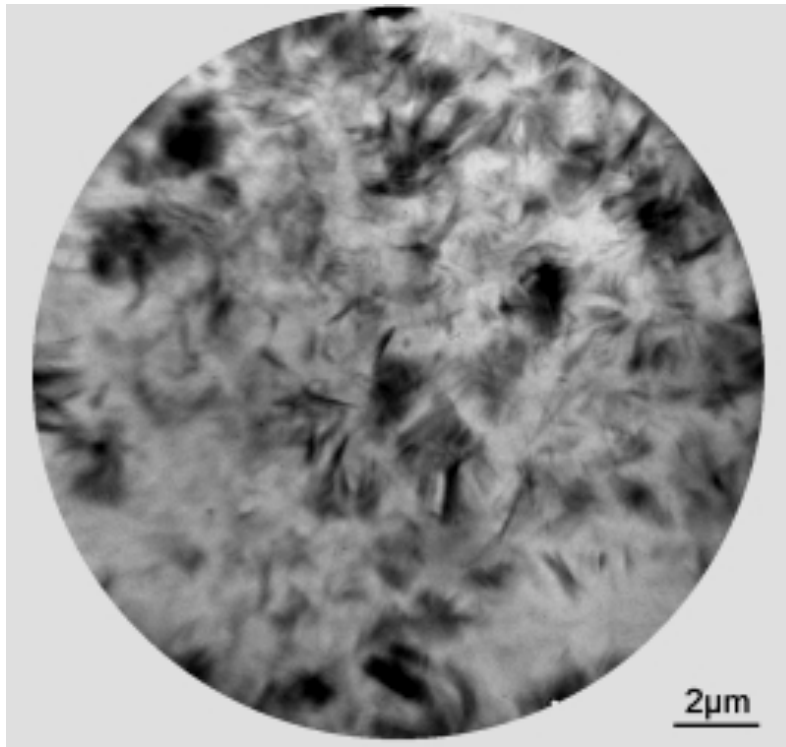
*Experiment performed by
M. Prasciolu and D. Cojoc, TASC/ INFM)*



Elettra
Sincrotrone
Trieste

Environmental science: Imaging in liquids

Bacteria and clay dispersion: Destruction of associations of clay particles by soil microbes

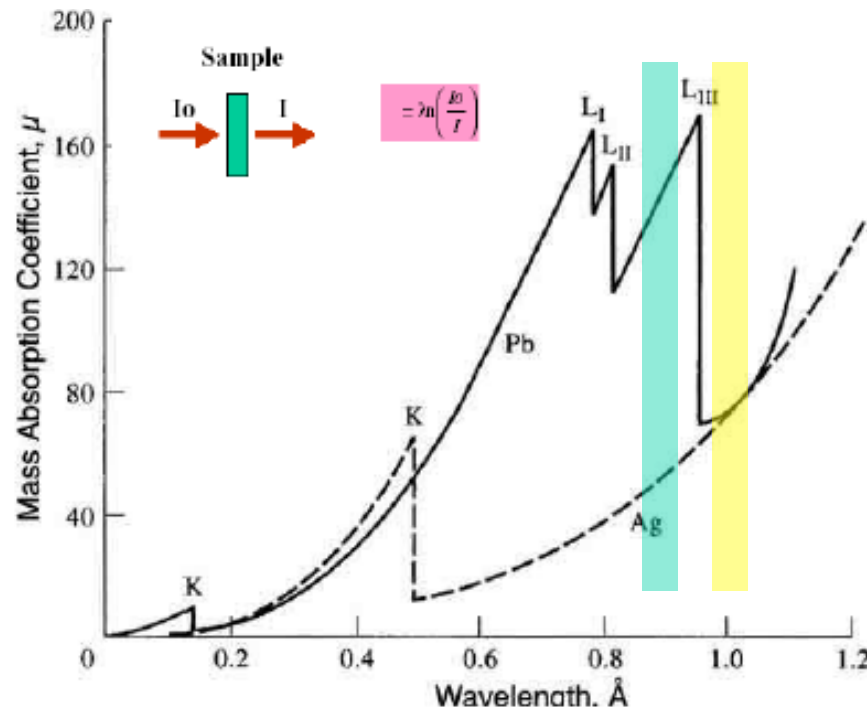


X-ray images acquired with the full-field imaging microscope at BESSY I @ 520 eV

Samples analysed in the natural hydrated state:
→ **no alteration of the environment of the sample**

J. Thieme et al., IRP, Uni Goettingen / G. Machulla, Uni Halle, D

Across edge imaging



Discontinuities due to absorption

The absorption occurs when the incoming X-rays are matching the electron binding energies

Absorption edges are fingerprints \Rightarrow they can be used to identify the chemical elements

By taking two images, one above and one below a specific absorption edge, the correspondent chemical element will give a high contrast difference in the two images

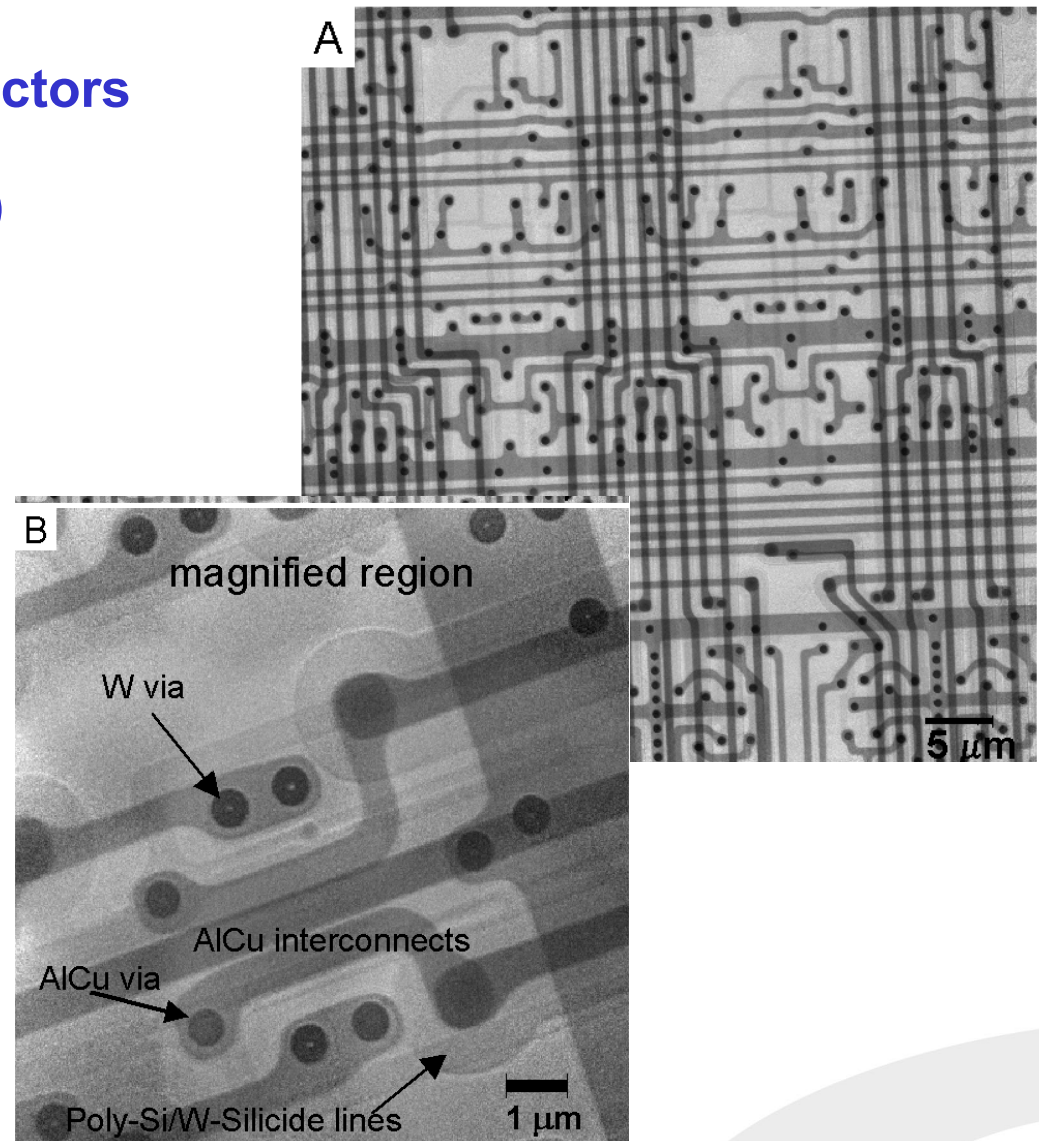
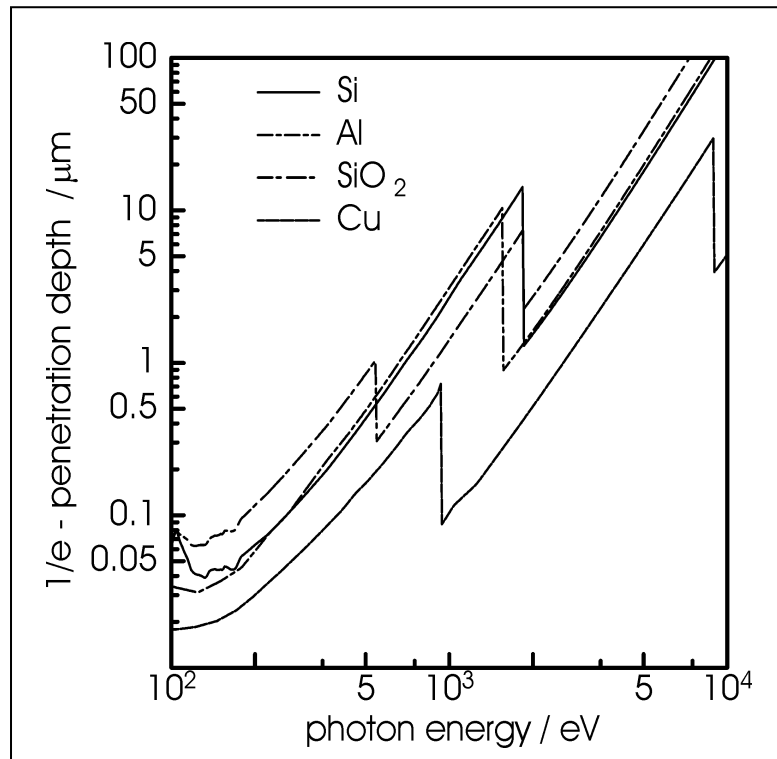


Elettra
Sincrotrone
Trieste

Brightfield imaging at higher photon energies

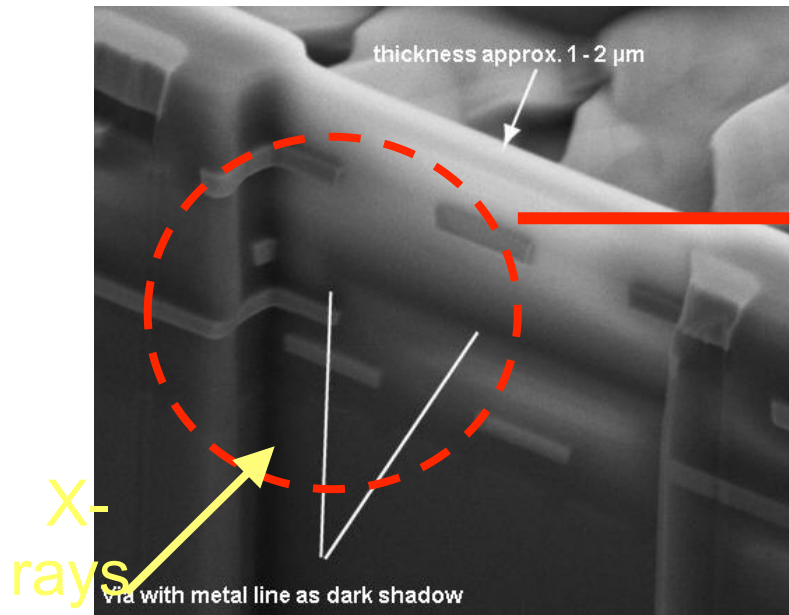
Characterization of morphology
and defects in modern semiconductors
with a full-field imaging
microscope (@ 1.8 keV, XM1/ ALS)

Sample preparation:
Back side thinning of Si wafer

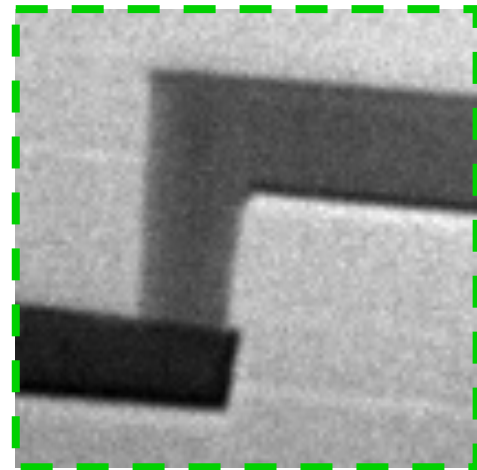
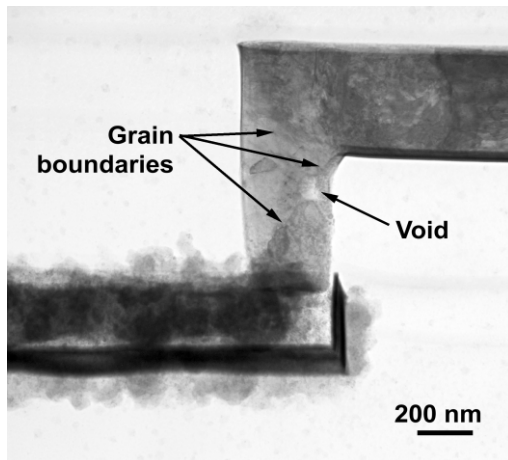
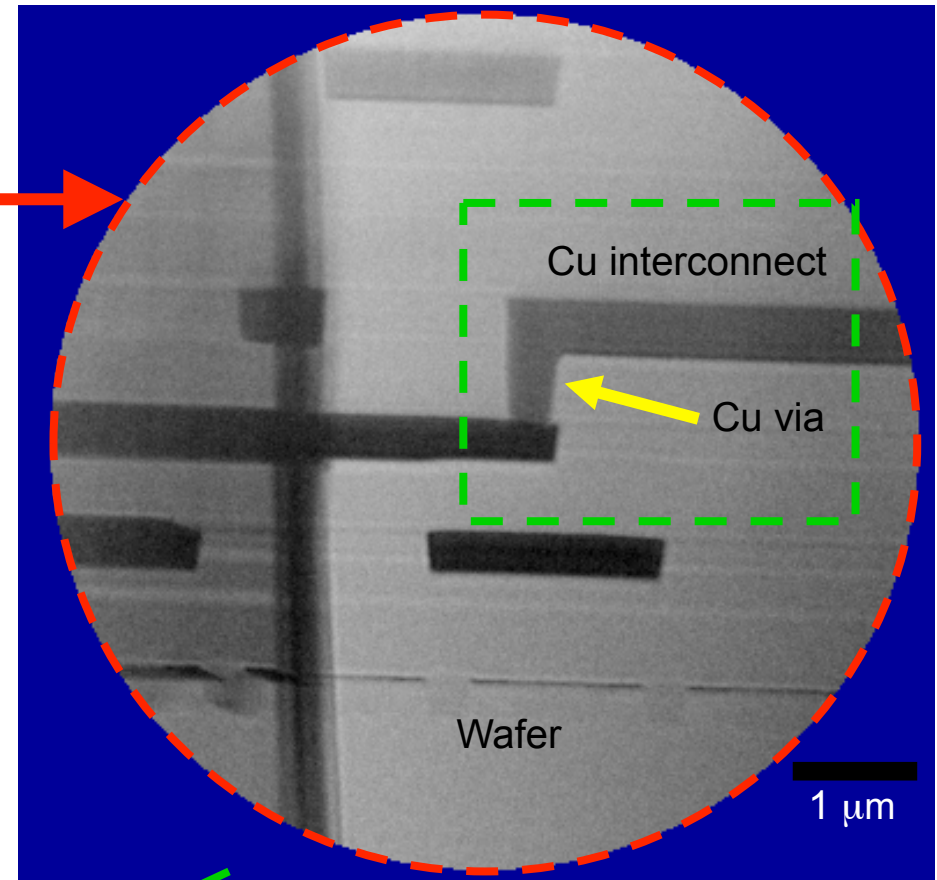


Material sciences: Electromigration in modern Cu interconnects

SEM micrograph



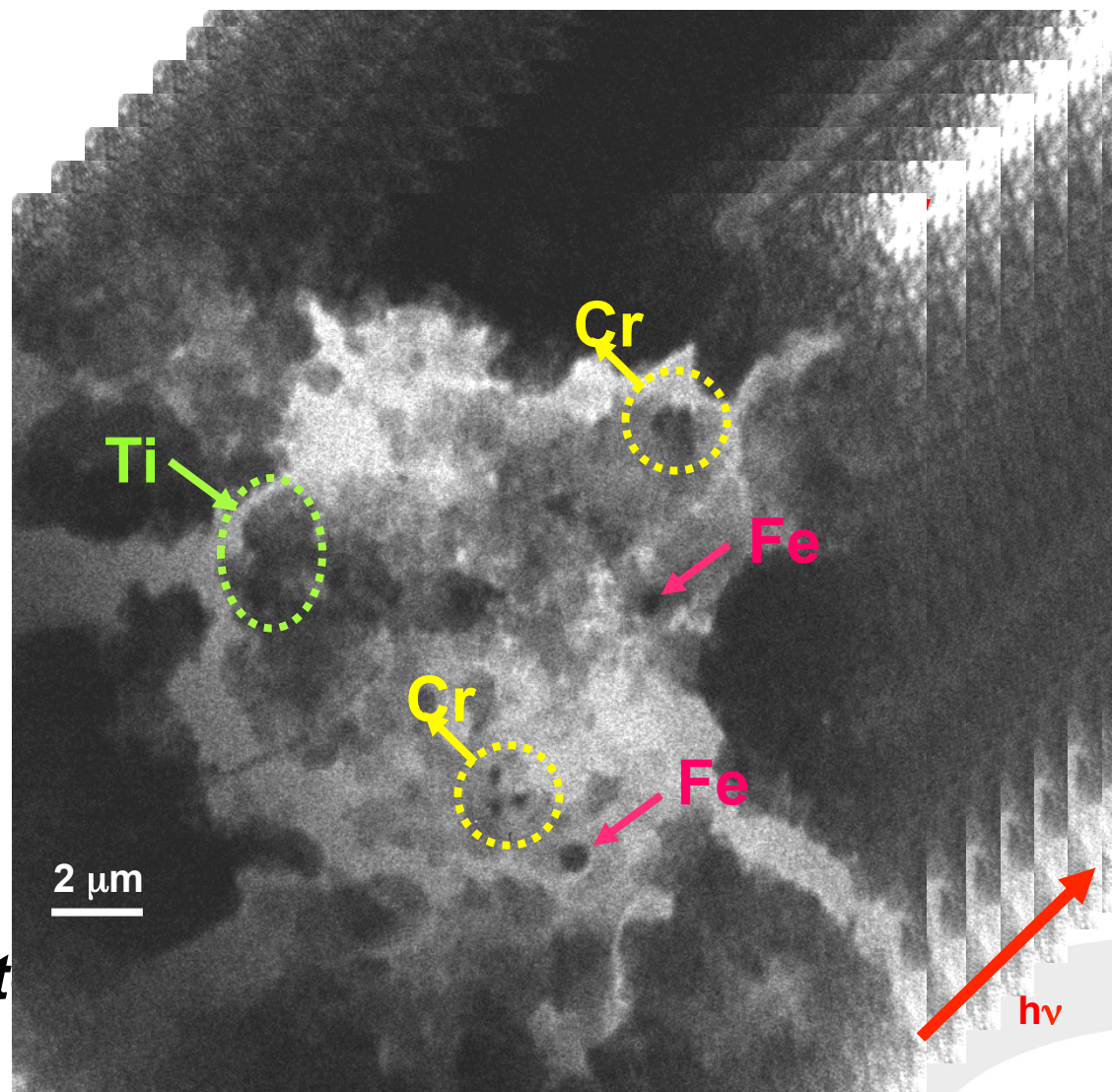
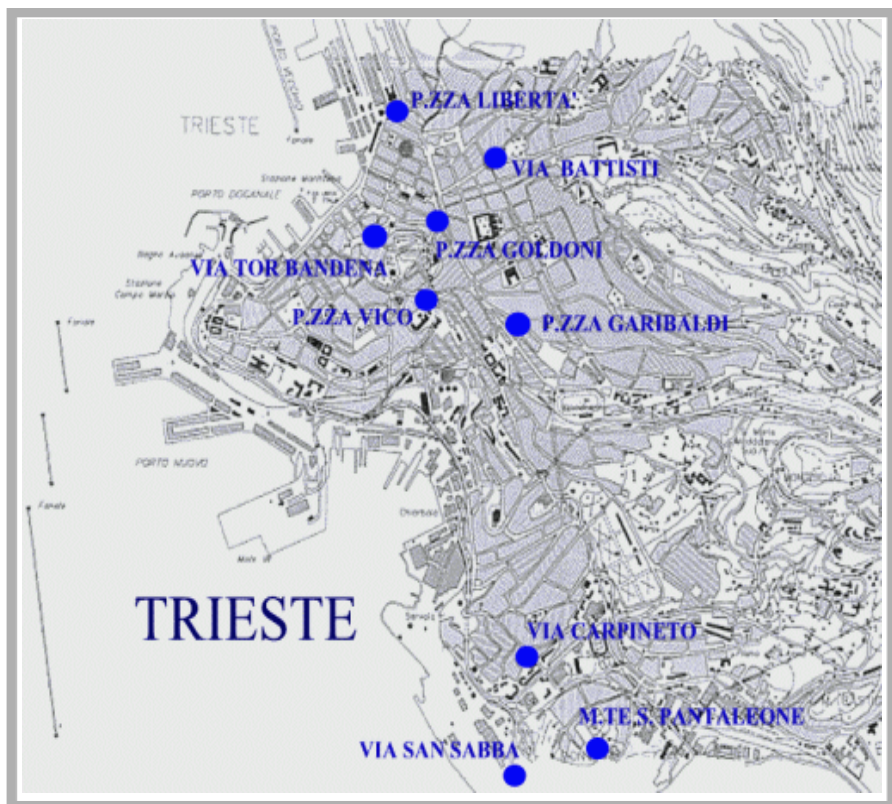
X-ray micrograph imaged at 1.8 keV



high current density

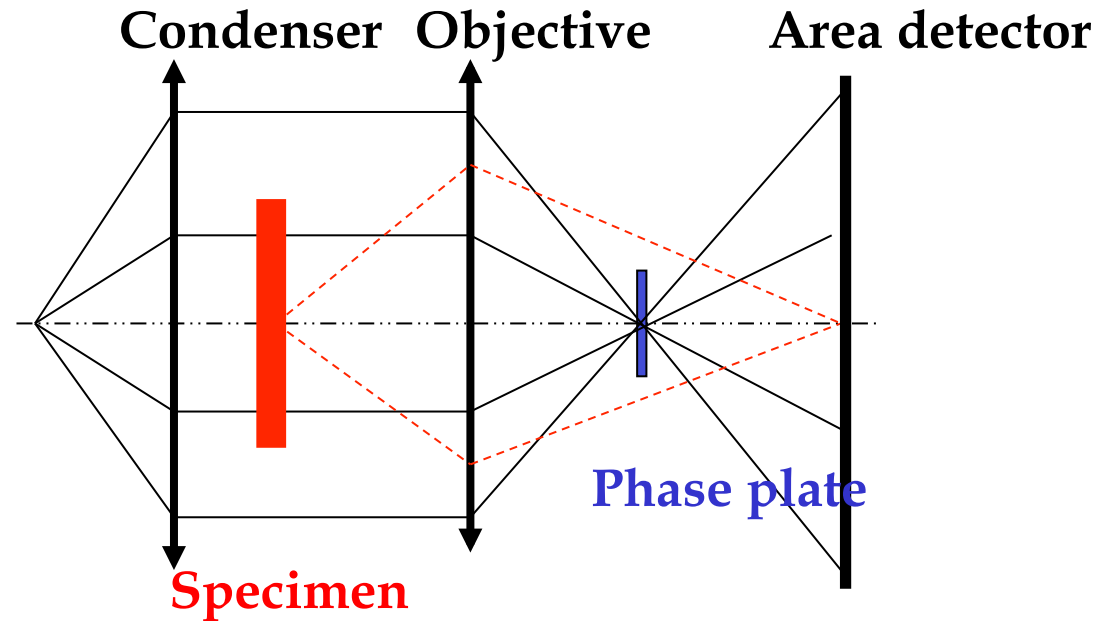
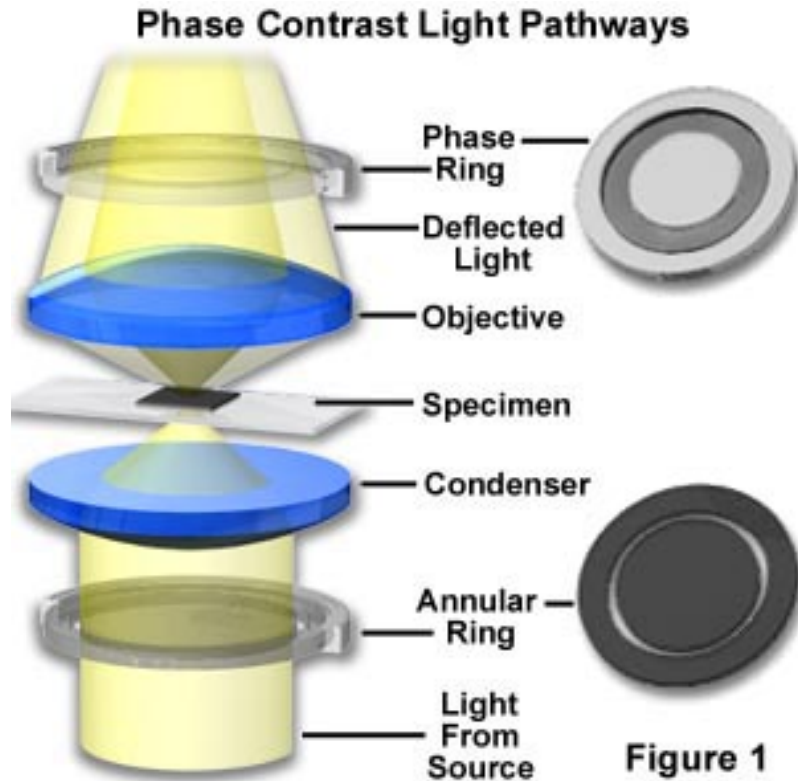


Environmental science: Analysis of air particulate matter



***P. Barbieri et al.,
Dept. of Chem., Univ. Trieste***

Basics of Zernike phase contrast



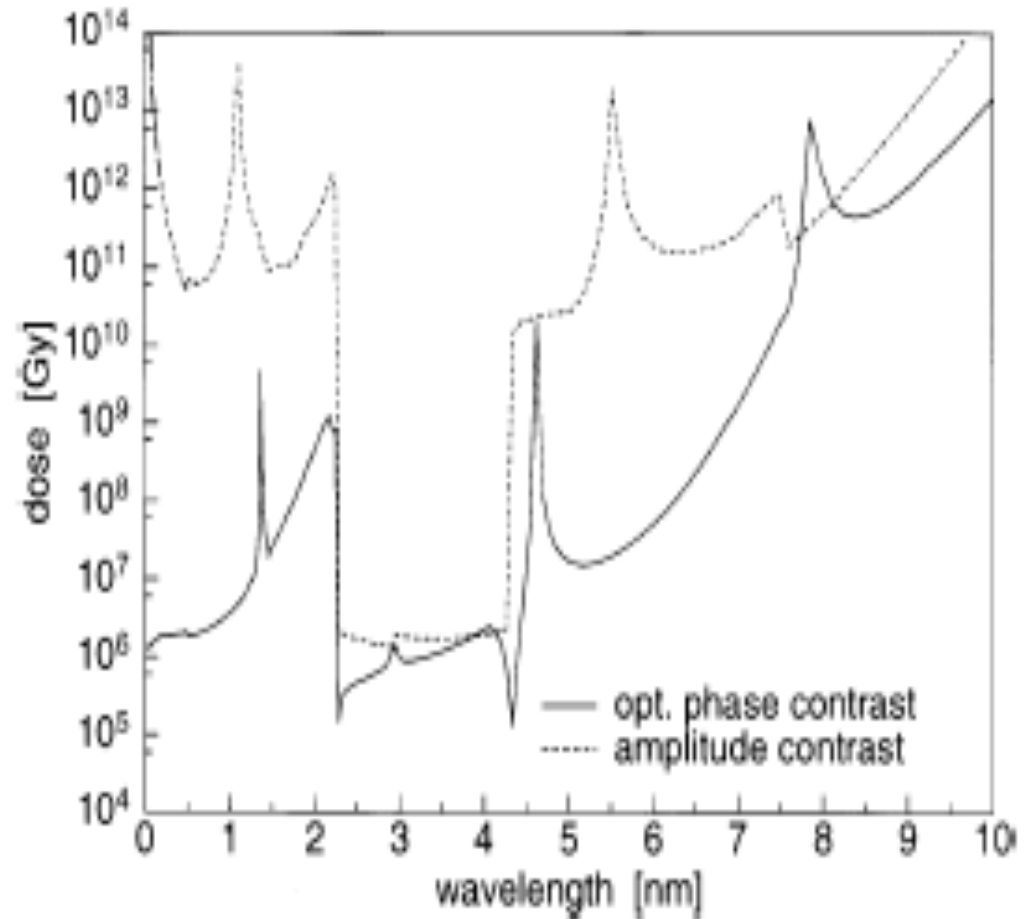
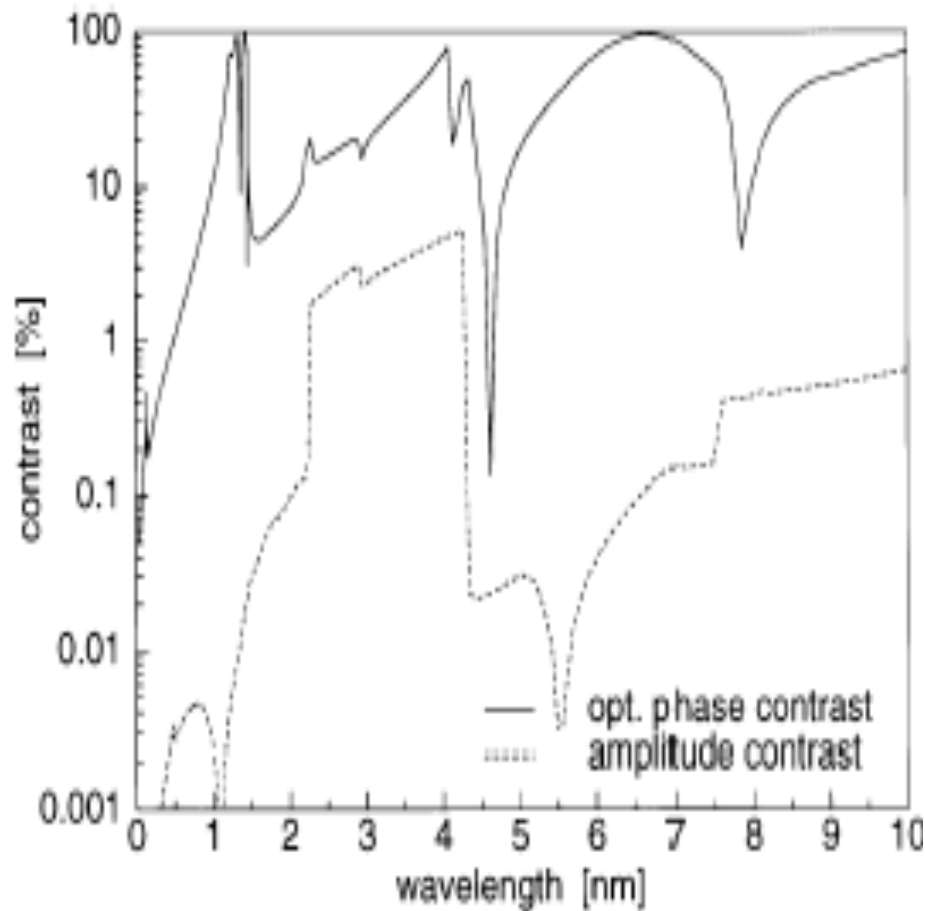
$$A_{specimen} = A_{surr} e^{i\Phi} = A_{surr} e^{i \frac{2\pi}{\lambda} \Delta t} \approx A_{surr} (1 + i\Phi) \quad \Phi \ll 1$$

Phase plate in “back-focal” plane: Phase of A_{surr} can be shifted by $\pm \pi/2$!!!
Phase differences are converted in amplitude differences !!!



Elettra
Sincrotrone
Trieste

Zernike phase contrast in X-ray microscopy

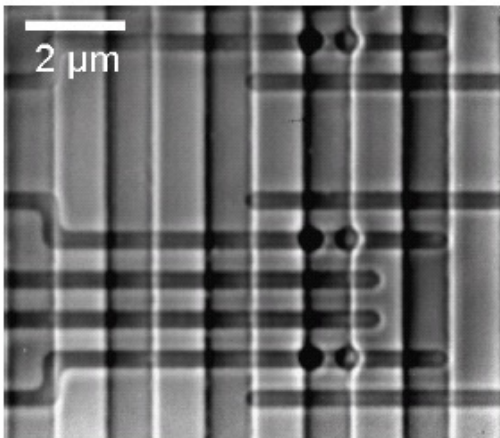
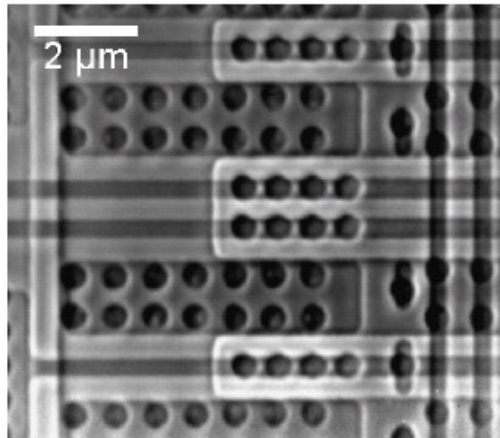


Contrast and dose for a model protein $C_{94}H_{139}N_{24}O_{31}S$

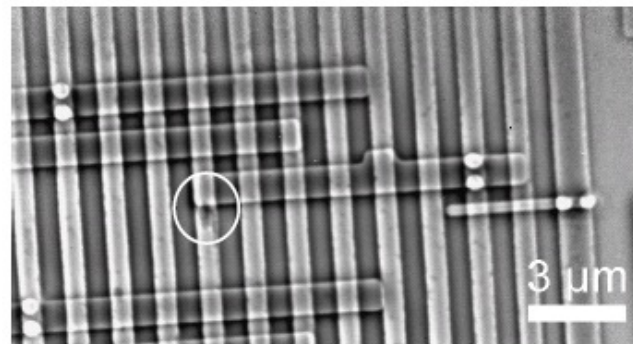
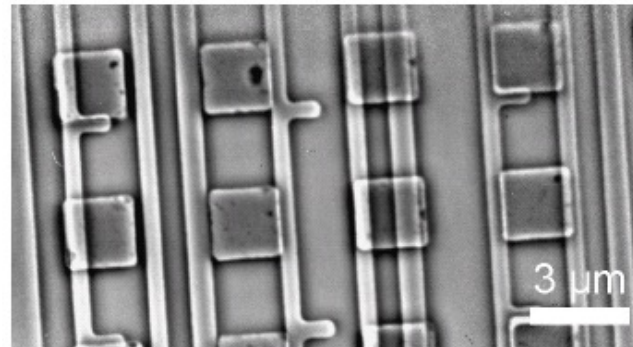
Zernike phase contrast with multi-keV X-rays



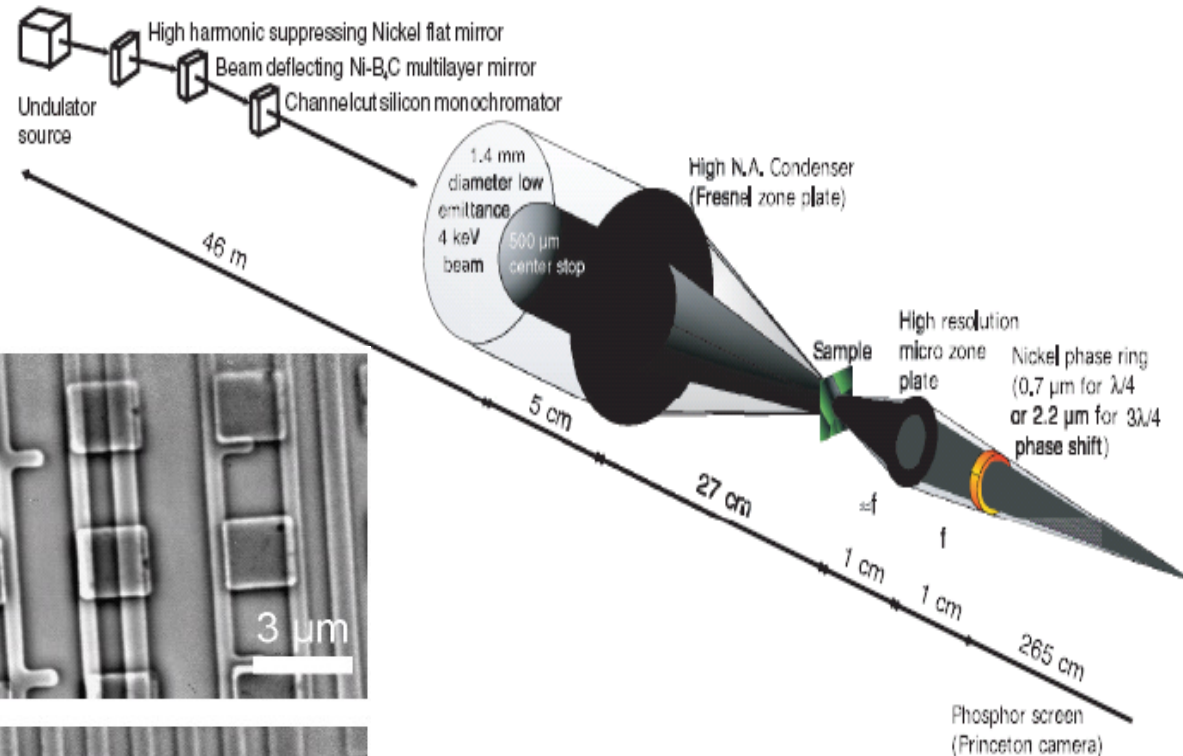
Elettra
Sincrotrone
Trieste



90 deg shift (pos.)



270 deg (neg.)

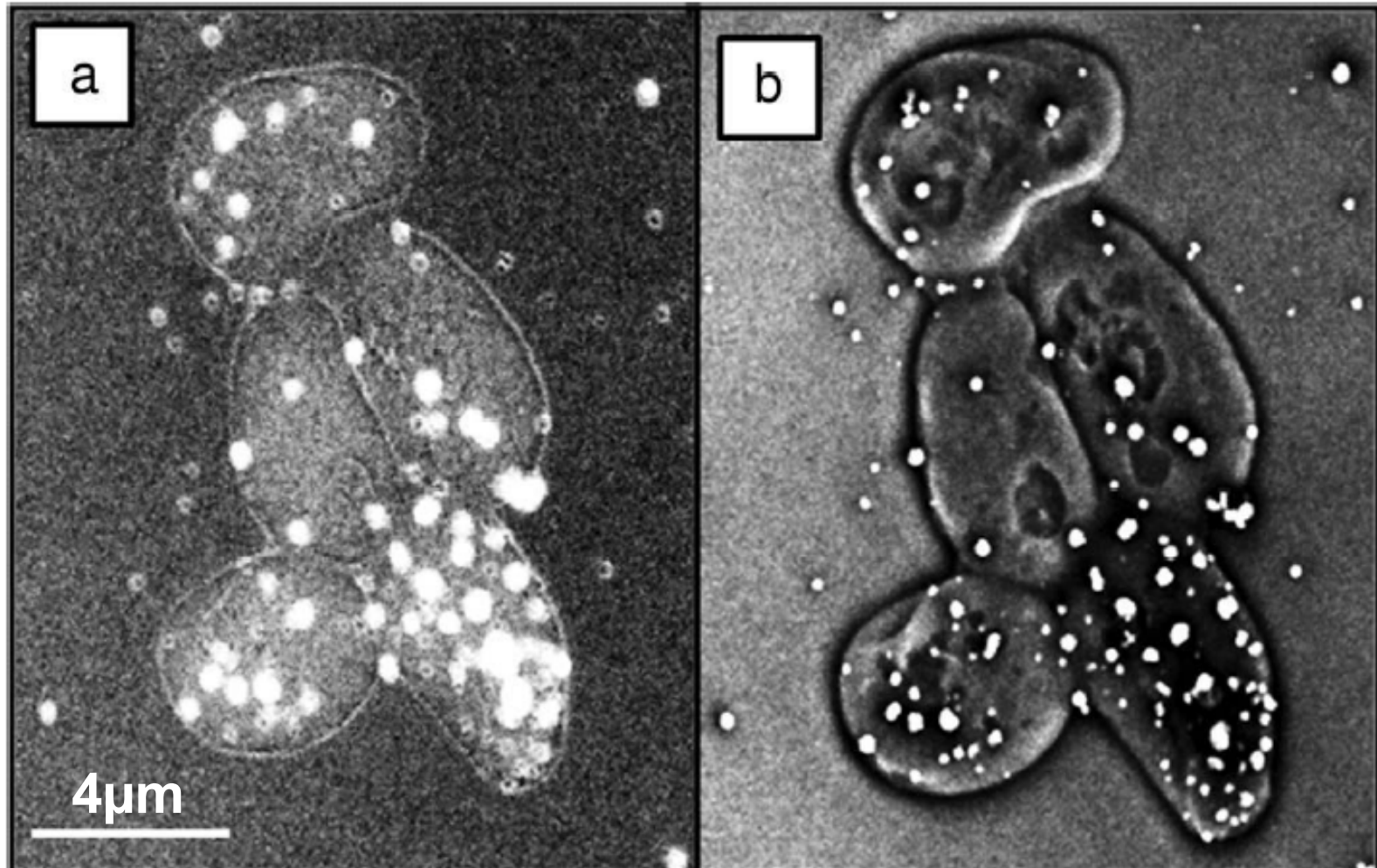


Cu interconnect
structures imaged
at 4 keV photon energy

60nm spatial resolution

Images acquired with the FFIM at ID21, ESRF
U. Neuhaeuser et al. J. Phys. D: Appl. Phys. 36, A79-A82.

TXM images of *S. cerevisiae* at 5.4 keV

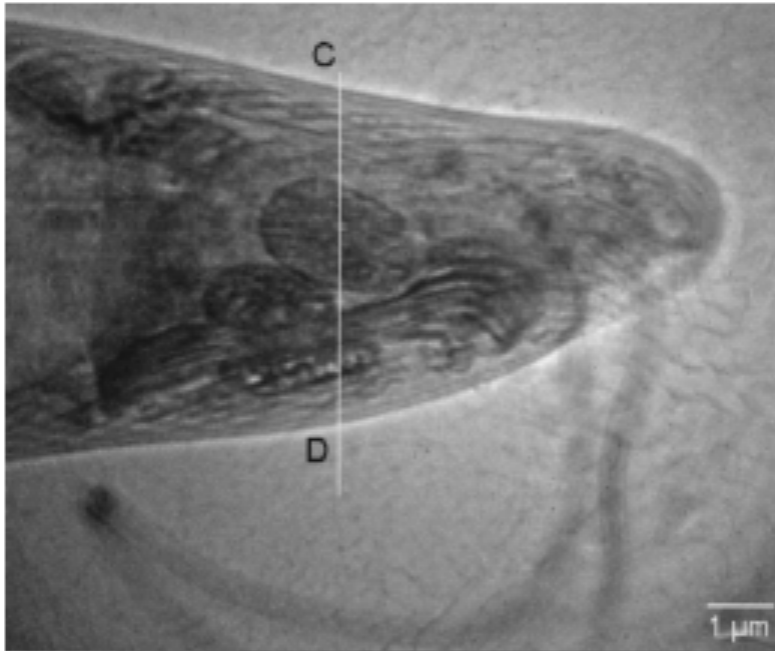


a) in absorption contrast

(b) in Zernike phase



Zernike phase contrast in X-ray microscopy

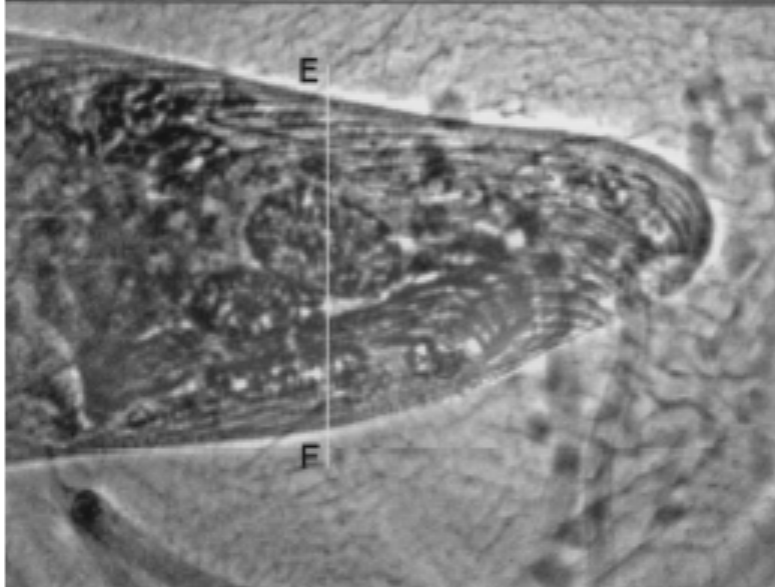


Amplitude and Zernike phase contrast images of an alga *Euglena gracilis*

E = 500 eV, accumulated dose is 3×10^6 Gray

Amplitude: 3 s

Phase contrast: 15 s



Drawbacks of Zernike phase contrast:

- **Halos around structures**
- **Quantitative analysis difficult**
- **Limitation in spatial resolution**
- **Not all spatial frequencies are treated equally**

Darkfield or darkground imaging

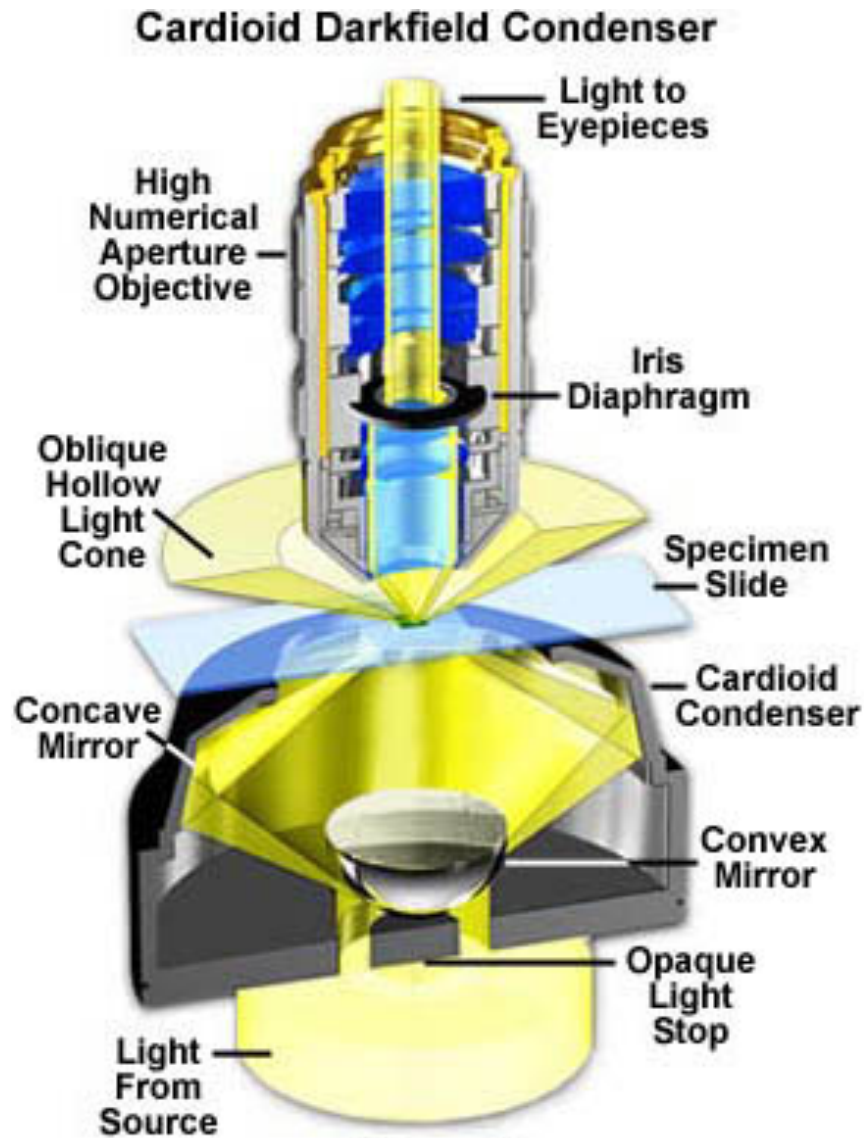
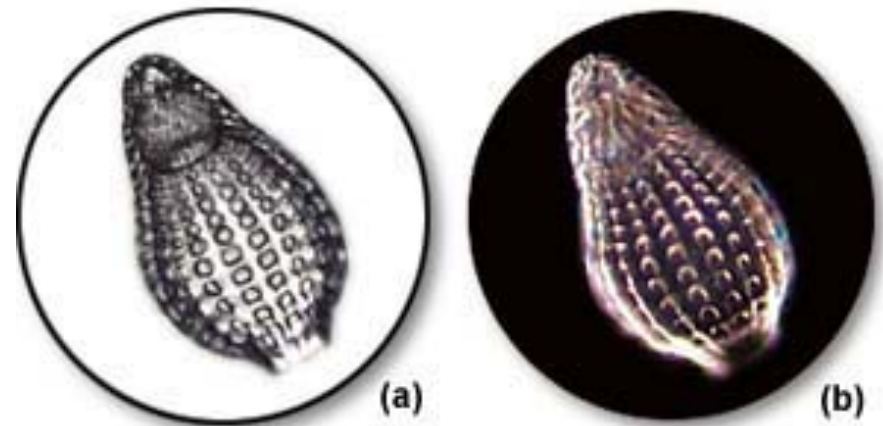


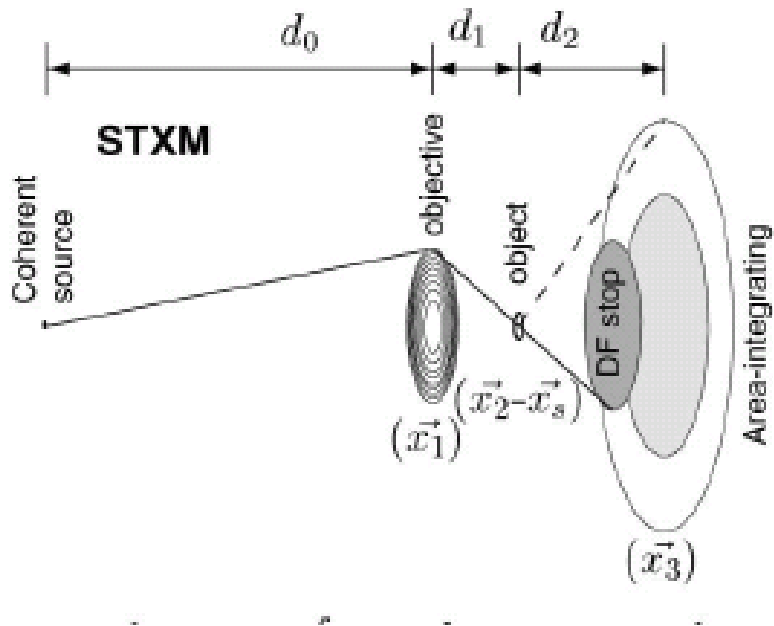
Figure 1

Darkfield illumination requires blocking out of the central light which ordinarily passes through and around (surrounding) the specimen, allowing only oblique rays from every azimuth to "strike" the specimen.



Visible light micrographs of silica skeletons from a small marine protozoan (radiolarian)

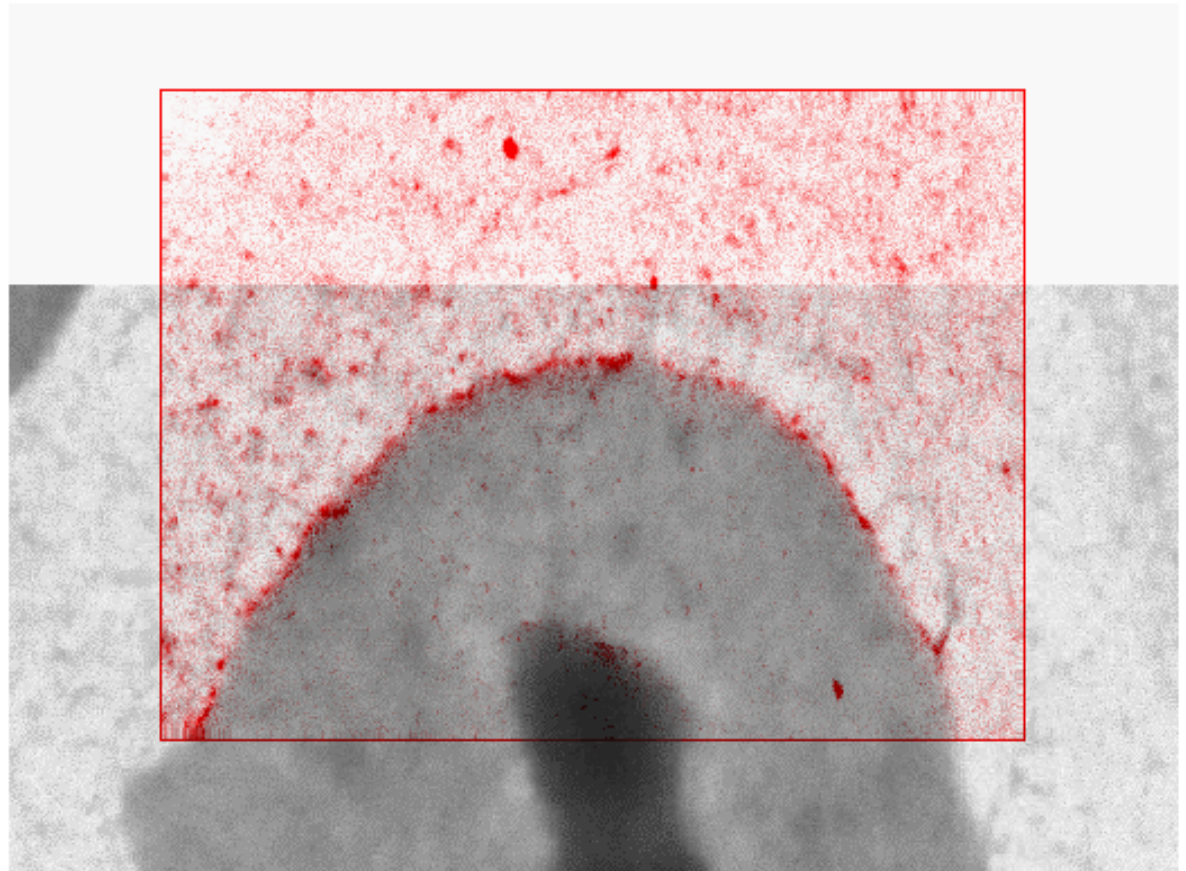
Darkfield imaging in scanning X-ray microscopy



Technique is especially suited for small, strongly scattering particles as for example a few 10nm diameter labelling spheres

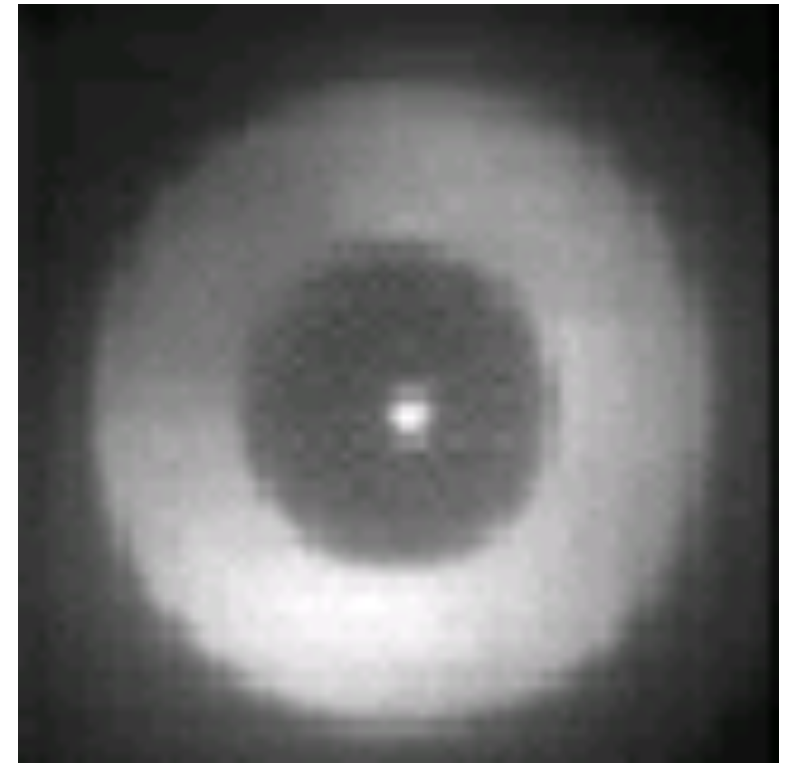
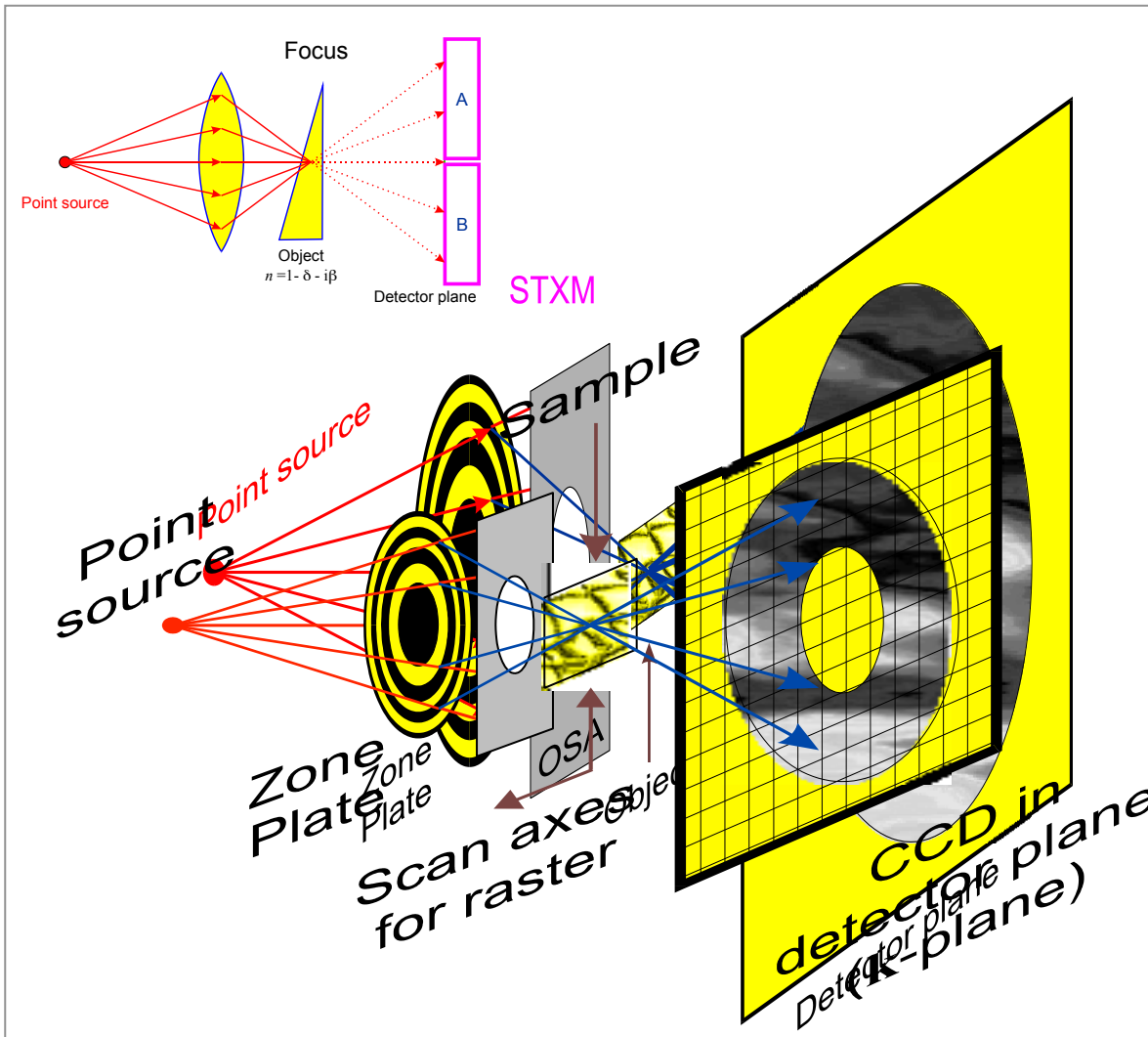
Brightfield image of a cell with Au labelling spheres overlaid with a darkfield image

Images acquired with STXM at the NSLS



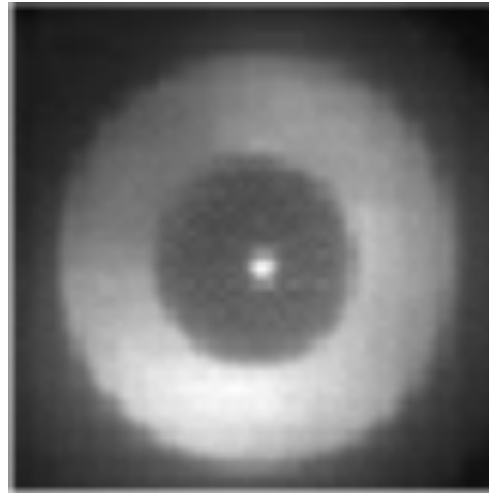
S. Vogt, M.A. thesis, SUNY Stony Brook (1997).

Detector based contrast technologies in scanning X-ray microscopy:



Frame transfer back-illuminated
Electron Multiplying CCD with shutter
and light converting system
(128x128px, 5 Mhz, 110f/s)

*Computational
extraction of
contrasts
by masking:*

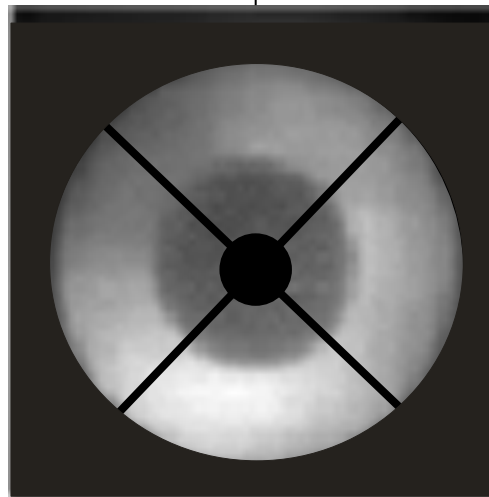


Raw data acquisition of
first diffraction order image
for each pixel of the raster
scan

Applying different masks



Bright field

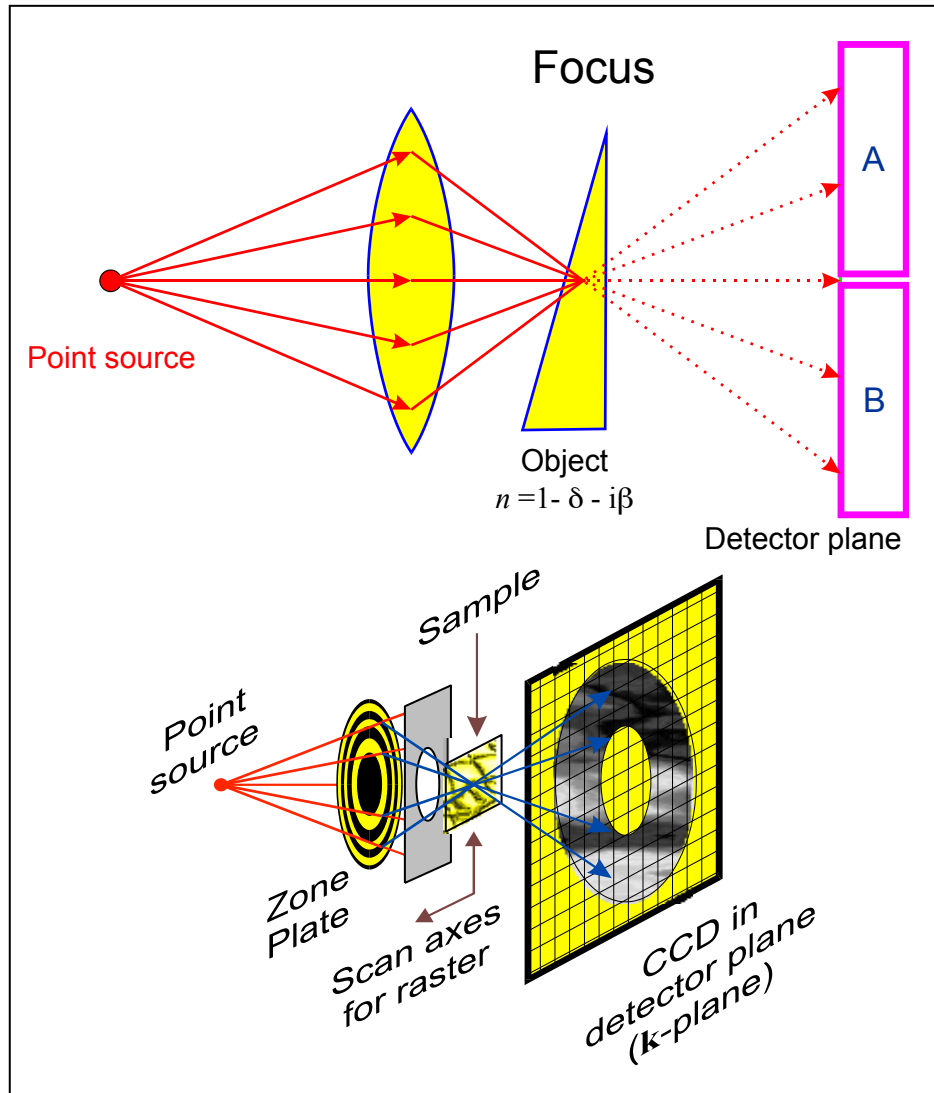


**Differential phase
and absorption**

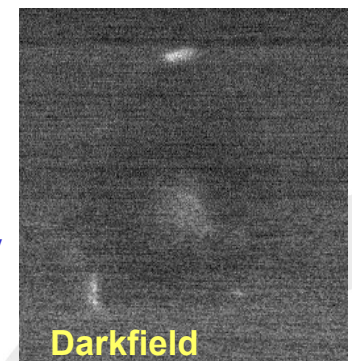
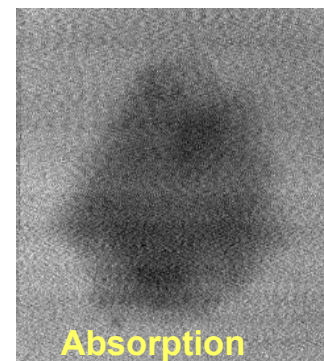
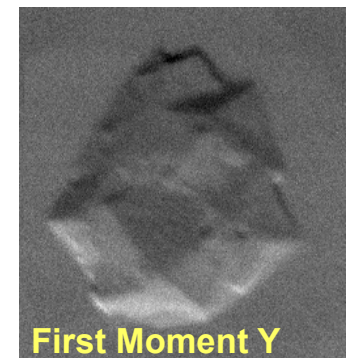
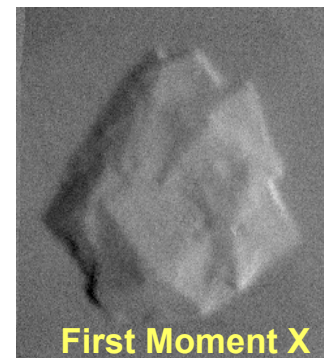


Darkfield

Principle: Differential phase contrast



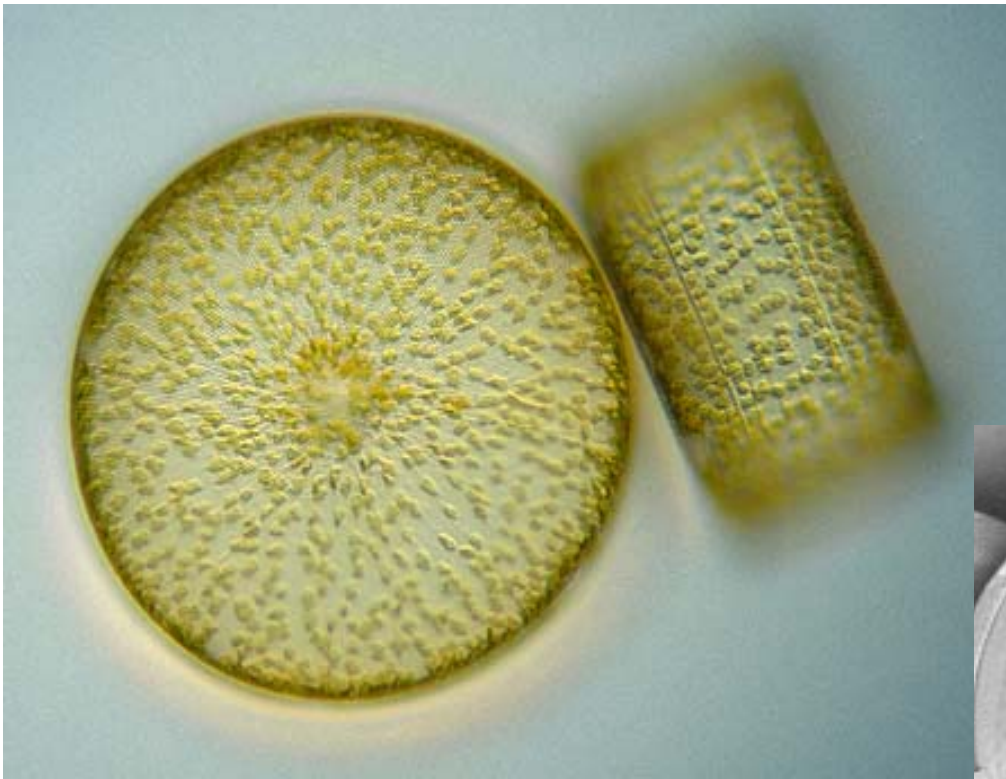
- The detector can be split into several elements
- The sum signal gives the incoherent bright-field signal
- Anti-symmetric signal combinations relate to the *phase gradient* of the object transmittance.



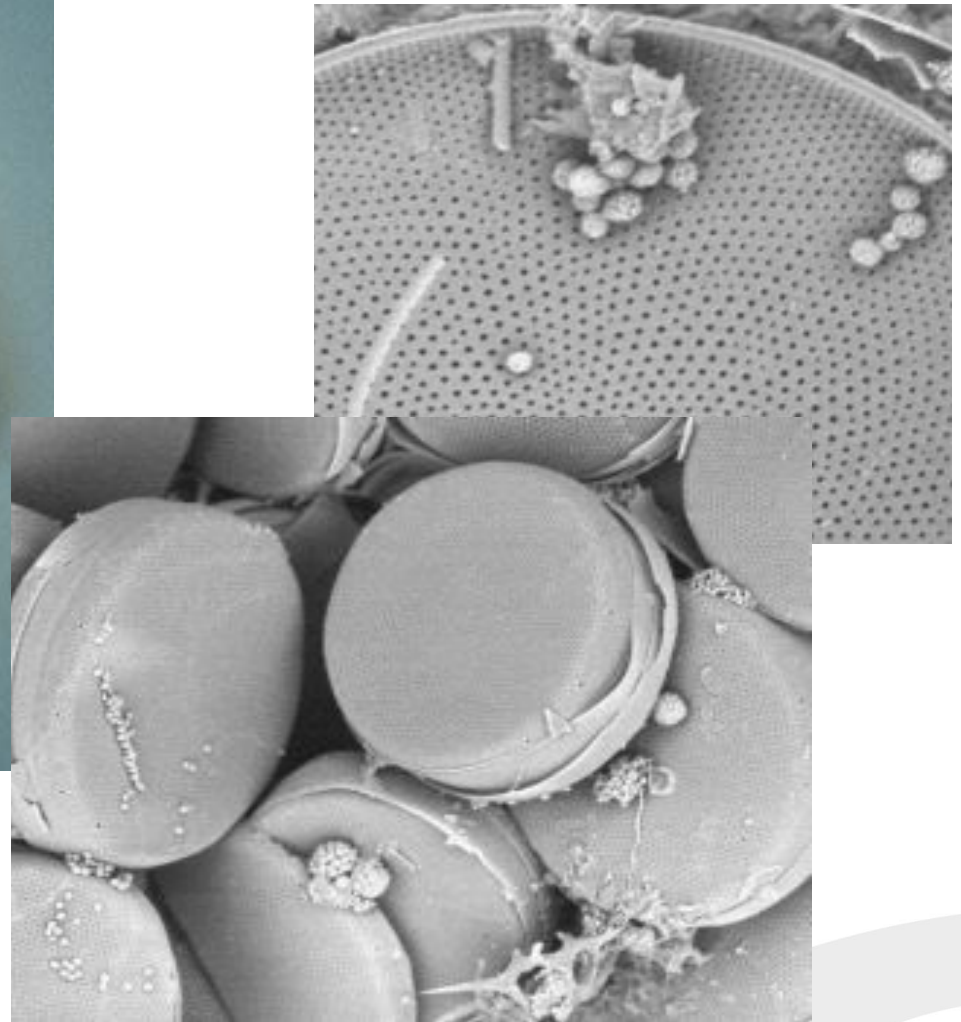
10 μm

3.3 keV

Marine biology: Imaging of giant diatoms

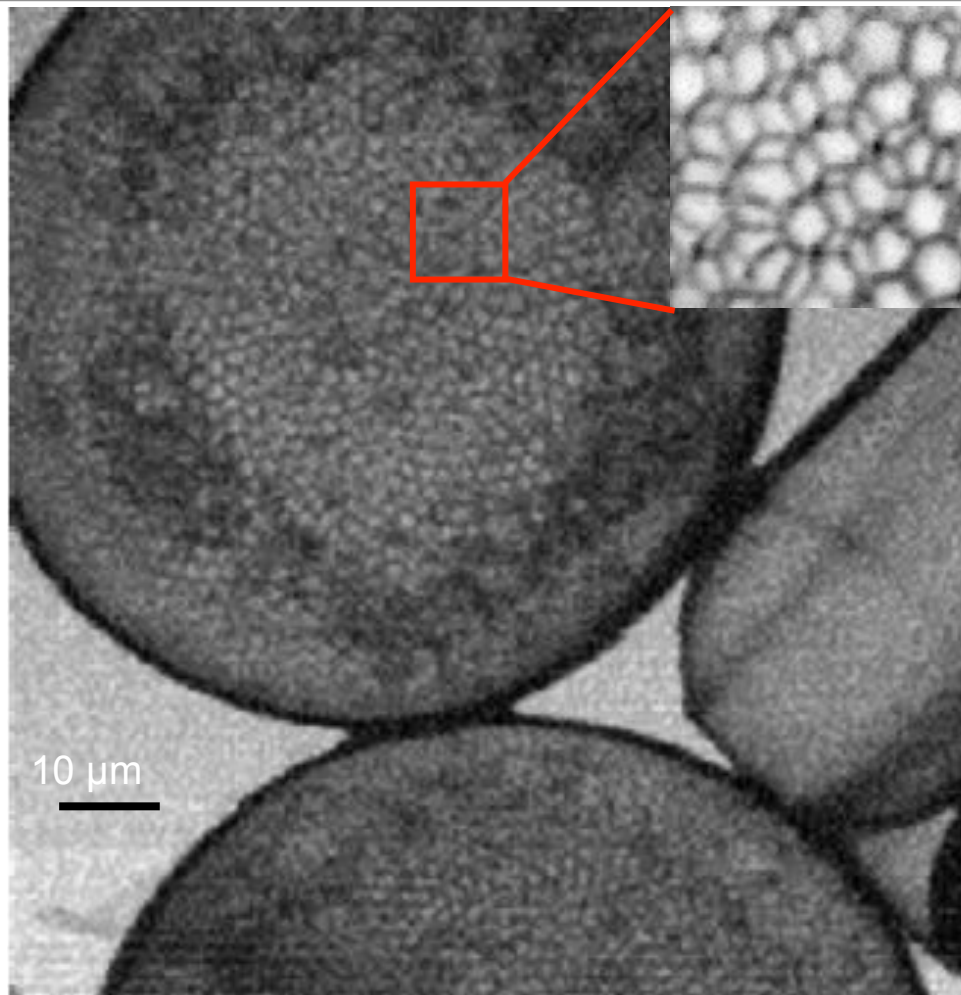


**Planktonic diatom *Coscinodiscus* sp.
(A. Beran, Laboratory for Marine
Biology, Trieste, I)**

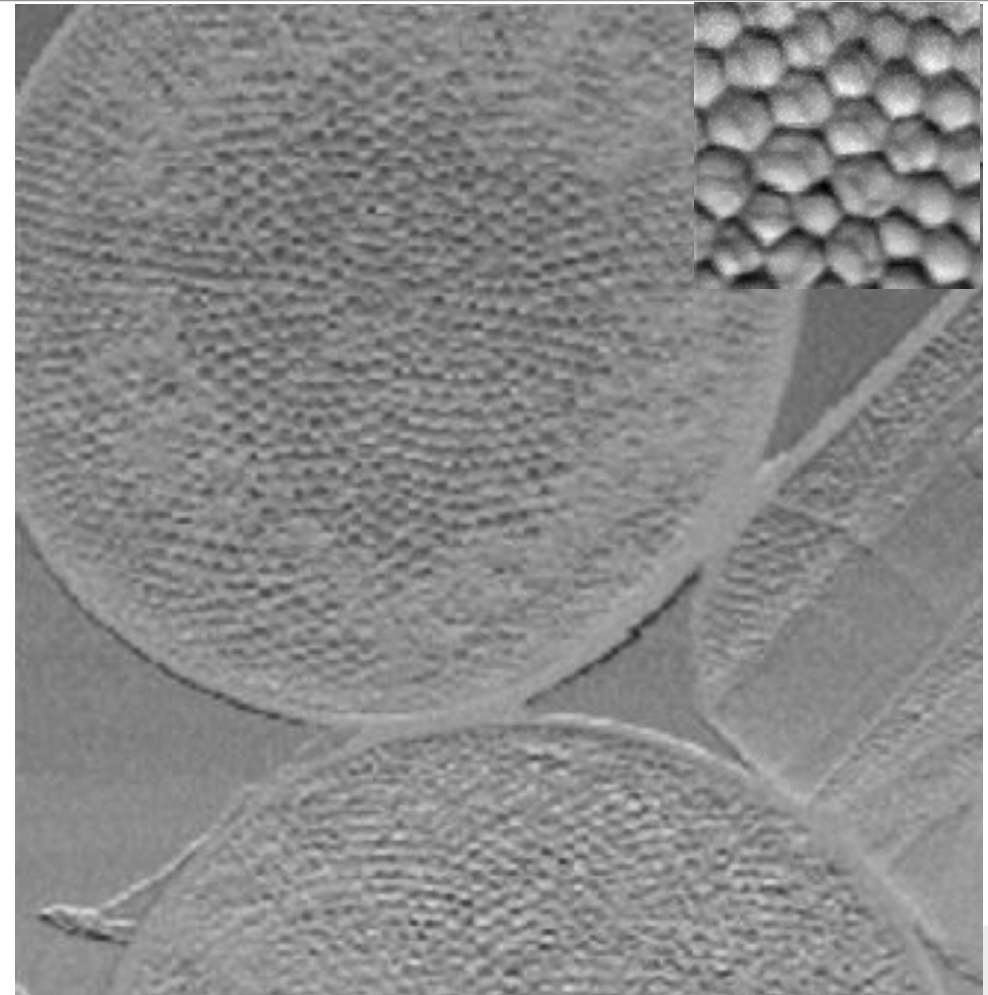


Simultaneous absorption and phase contrast imaging

Planktonic diatom “Casciodiscus sp.” (provided by LBM, Trieste, I)



Bright field image



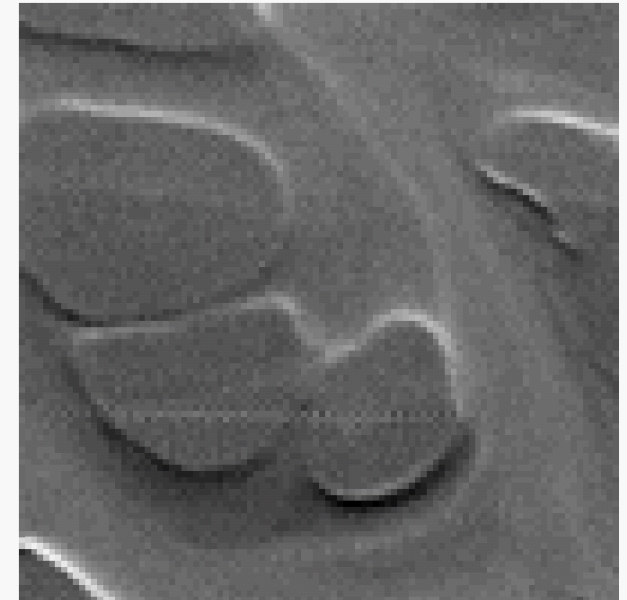
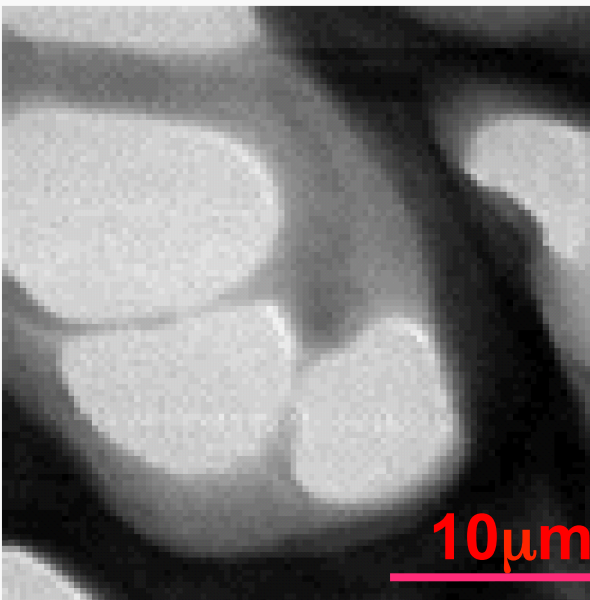
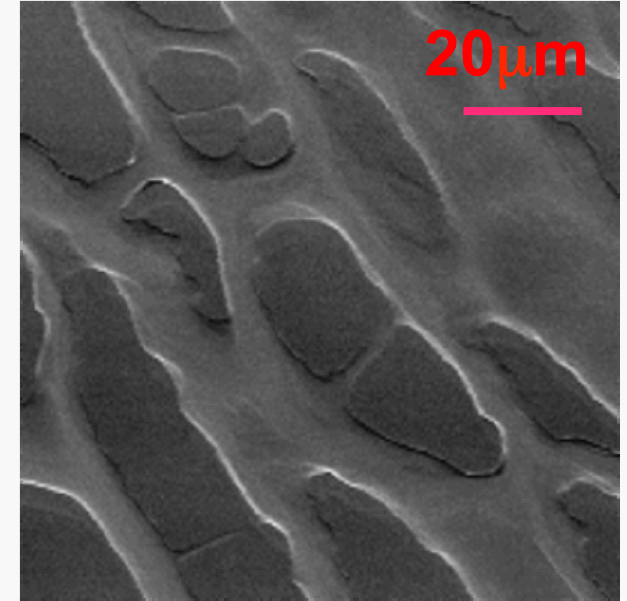
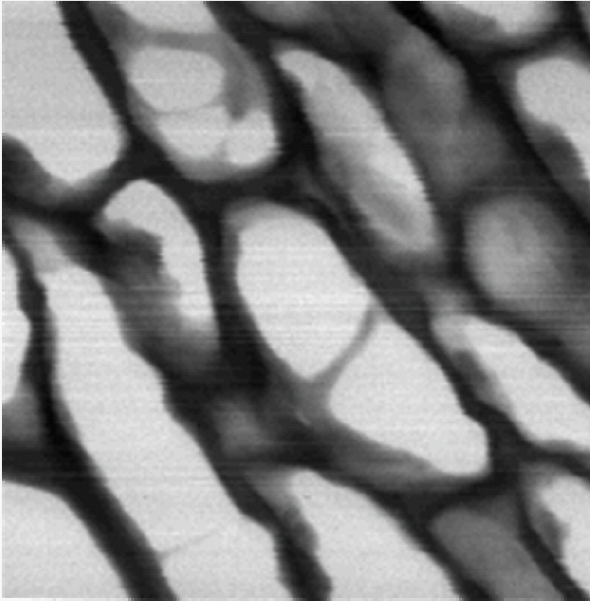
DPC mode – X-moment

Images acquired in STXM mode with FRCCD camera; E=1320 eV, 200x190 px, 50ms dwell/px

Brightfield and differential phase contrast images acquired simultaneously with configured detector



Elettra
Sincrotrone
Trieste



**coffee bean cell
membranes**

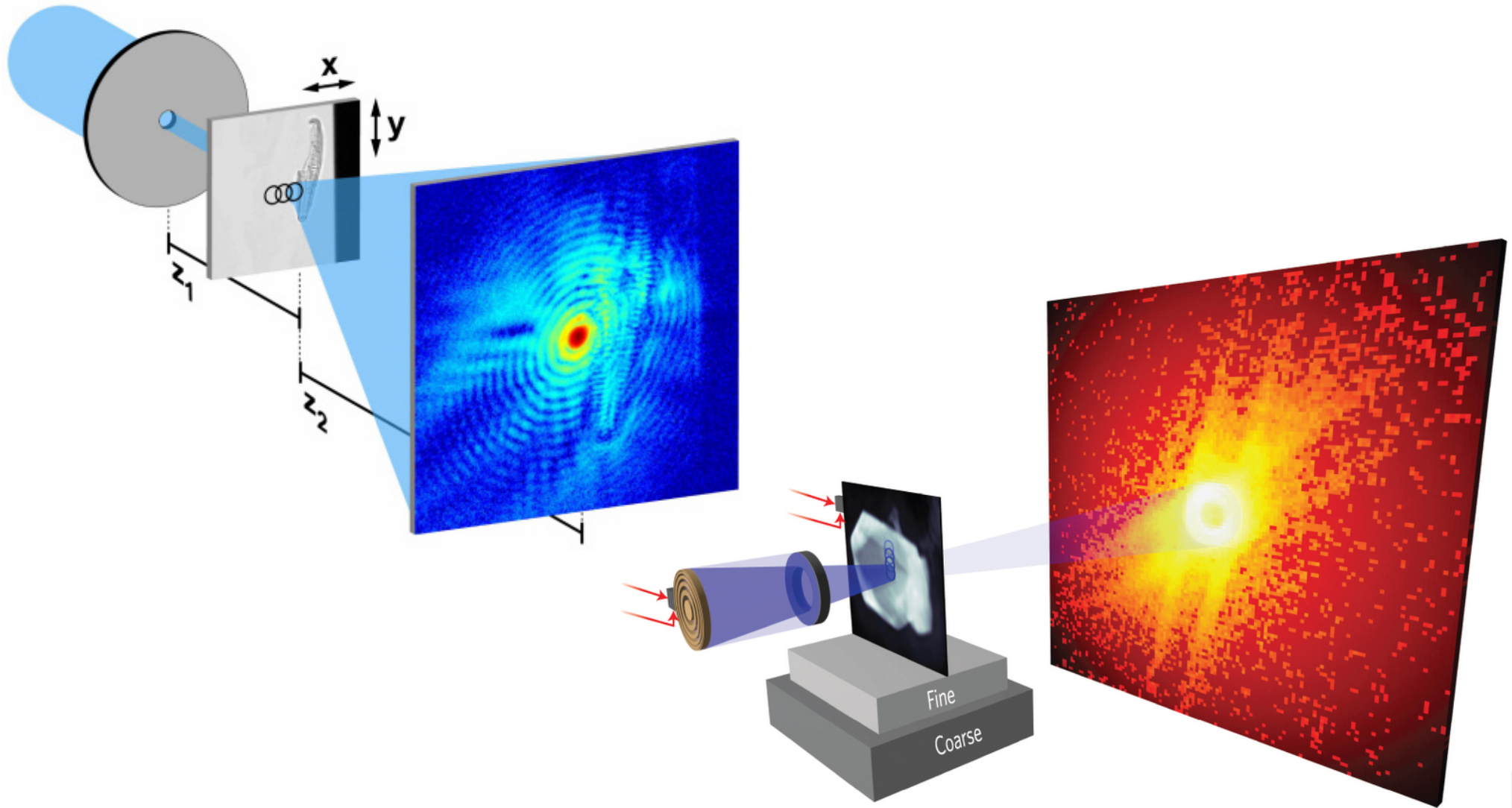


B. Bonnlaender, F. Sicilia, Illy AromaLab, et al.

Ptychography (CDI)

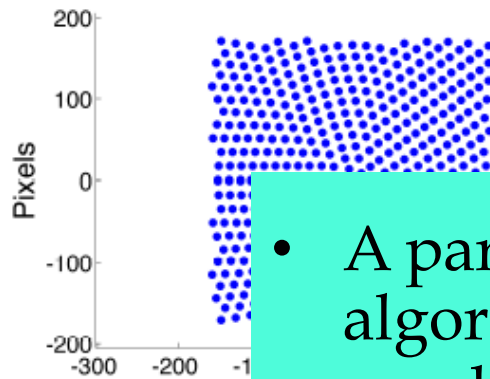
- Ptychography is rapidly developing into an important imaging tool in X-ray microscopy.
- It doesn't require X-ray Optics
- The technique involves successively illuminating overlapping regions of a specimen with a coherent probe and recording the resulting diffraction patterns.
- It is important that the illuminated areas overlap significantly since those common regions provide duplicate information that allows computer algorithms to reconstruct reliably both the sample transmission function and the illuminating probe from the measured diffraction patterns.

Ptychography (CDI)



- K. Giewekemeyer, M. Beckers, T. Gorniak, M. Grunze, T. Salditt, and A. Rosenhahn Optics Express Vol. 19, Issue 2, pp. 1037-1050 (2011)
- D. A. Shapiro, Y.-S. Yu, T. Tyliczszak, J. Cabana, R. Celestre, W. Chao, K. Kaznatcheev, A. L. D. Kilcoyne, F. Maia, S. Marchesini, Shirley Meng, T. Warwick, L. Lisheng Yang, H. A. Padmore Nature Photonics 8, 765-769 (2014)

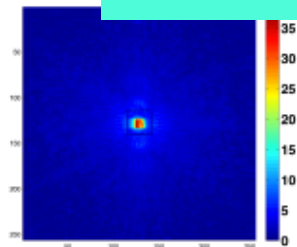
Ptychography Algorithms



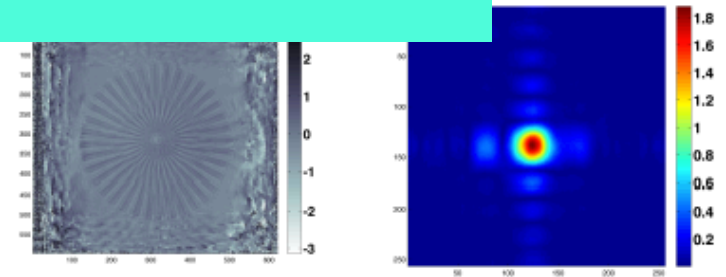
Scan

Start Guess Object

- A particularly useful feature of these algorithms is that they can recover the amplitude and phase of both these signals.
- The lateral resolution of the reconstructed image is not limited by the probe size, overcoming the limitation of X-ray microscopy imposed by the focusing optics



Processed Data



Probe from test object

Open to users in late 2007



The team of the TwinMic project (EC FP5; 2001 – 2004):

ESRF: J. Susini, M. Salome and O. Dhez (F)

SLS: C. David, T. Weitkamp, F. van der Veen (CH)

TASC/ INFM: E. Di Fabrizio, S. Cabrini and D. Cojoc (I)

KCL: G. R. Morrison, P. Charalambous, A. Gianoncelli (UK)

RAC: T. Wilhein and U. Vogt (D)

UNI Goettingen: J. Thieme (D)

IJS: J. Kovac (SLO)



The team that build the TwinMic BL at ELETTRA:

D. Cocco, D. Bacescu, A. Bianco, G. Sostero and D. Lonza

The team that implemented low-energy X-ray emission:

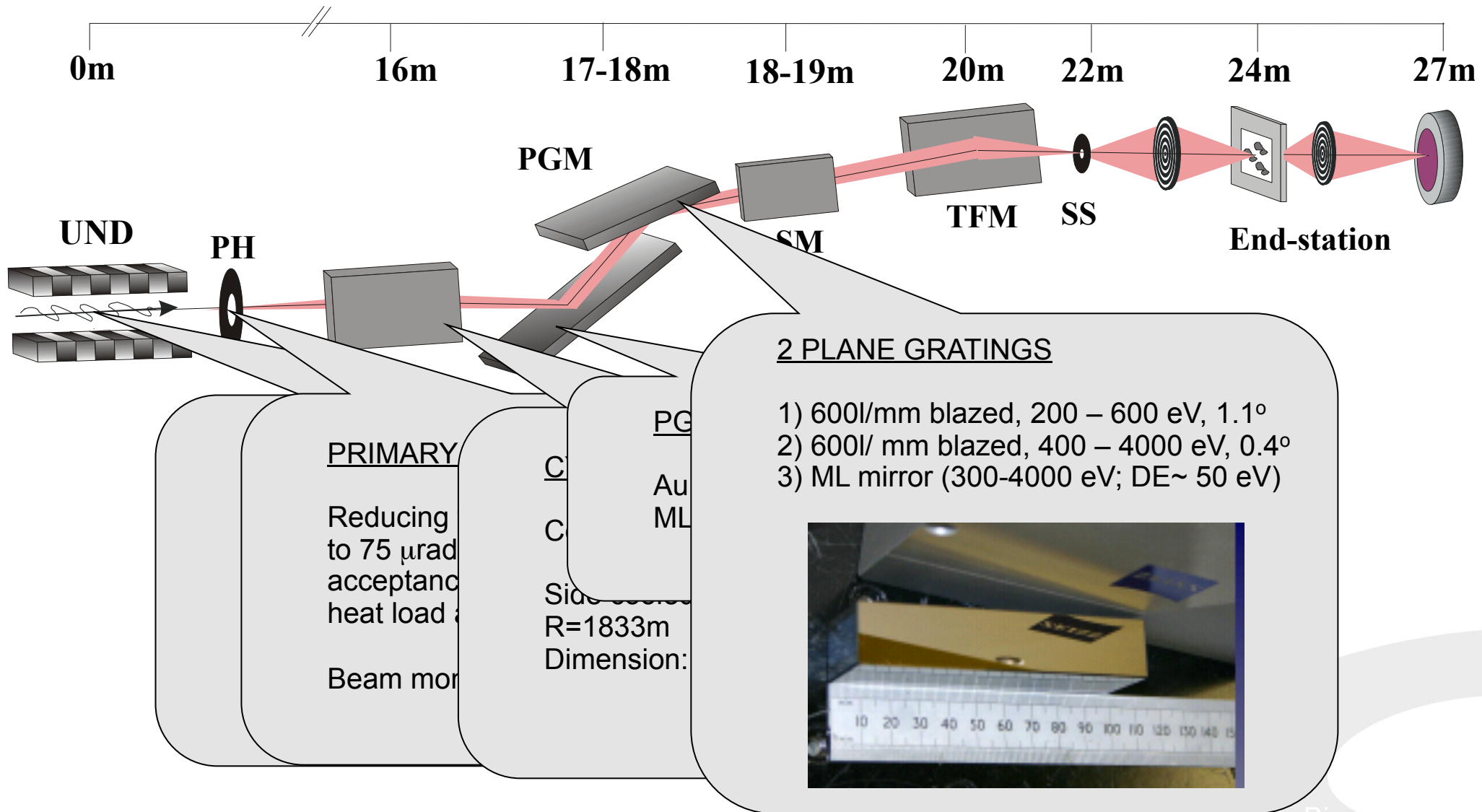
A. Gianoncelli, B. Kaulich (Elettra)

A. Longoni, R. Alberti, T. Klatka et al. (Politecnico Milano)

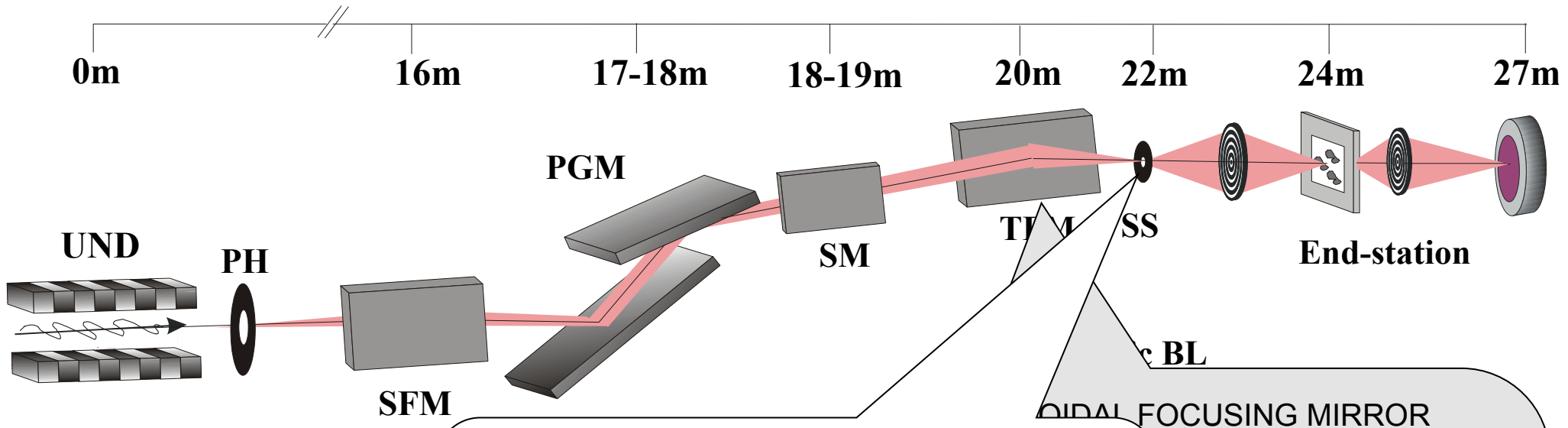
G. Margaritondo, V. Gajdosik, C. Poitry-Yamate et al.
(EPFL Lausanne)

And many many others ...

Dedicated TwinMic short undulator beamline (Section 1.1)



Dedicated TwinMic short undulator beamline (Section 1.1)

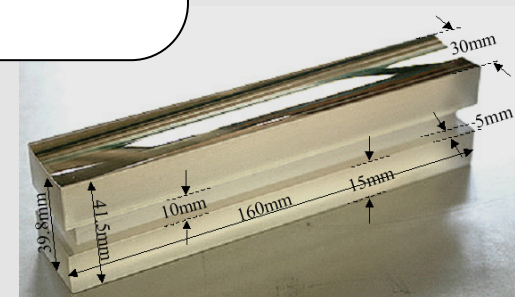


Secondary source for microscope station

Different apertures (pinholes) with diameters from 5 – 50 μm

beam into secondary

6.35cm
6x3 cm



TwinMic: Integration of both imaging modes into a single instrument

Spectromicroscopy:
XANES, LEXRF, AEI

Kinetics, dynamics,
3D

STXM

TXM


400 – 2200 eV

Brightfield
Darkfield
Differential PC
(simult.)
Nomarski DIC

Brightfield
Darkfield
Differential PC
Nomarski DIC



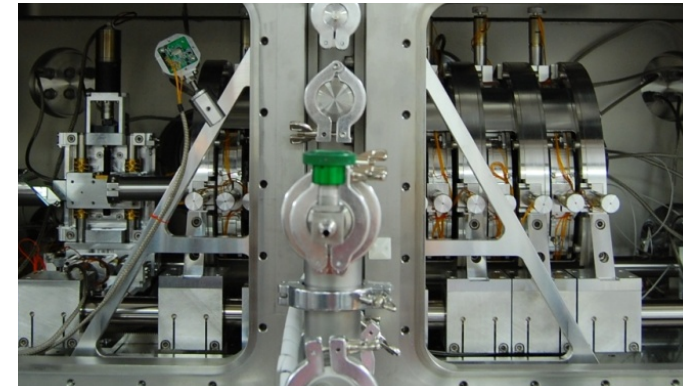
The European team that initiated the project

- Morphological analysis, XANES and AAEI
- Different contrasts incl. brightfield, differential phase and interference contrast, darkfield, etc
- Versatile specimen environment

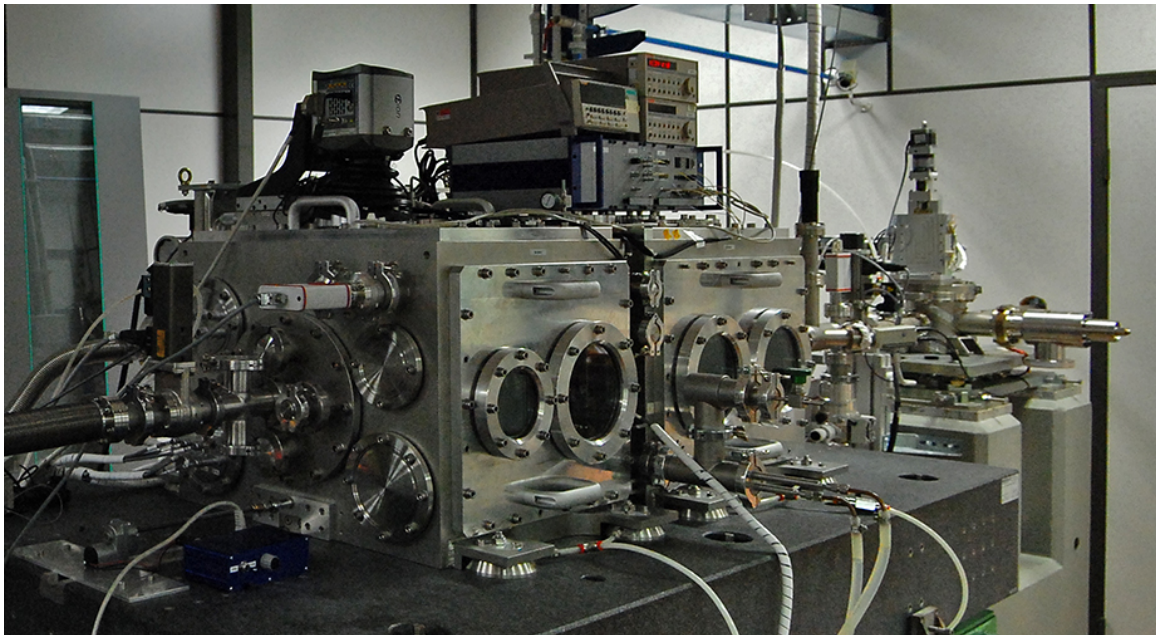
TwinMic microscope

400 – 2200 eV

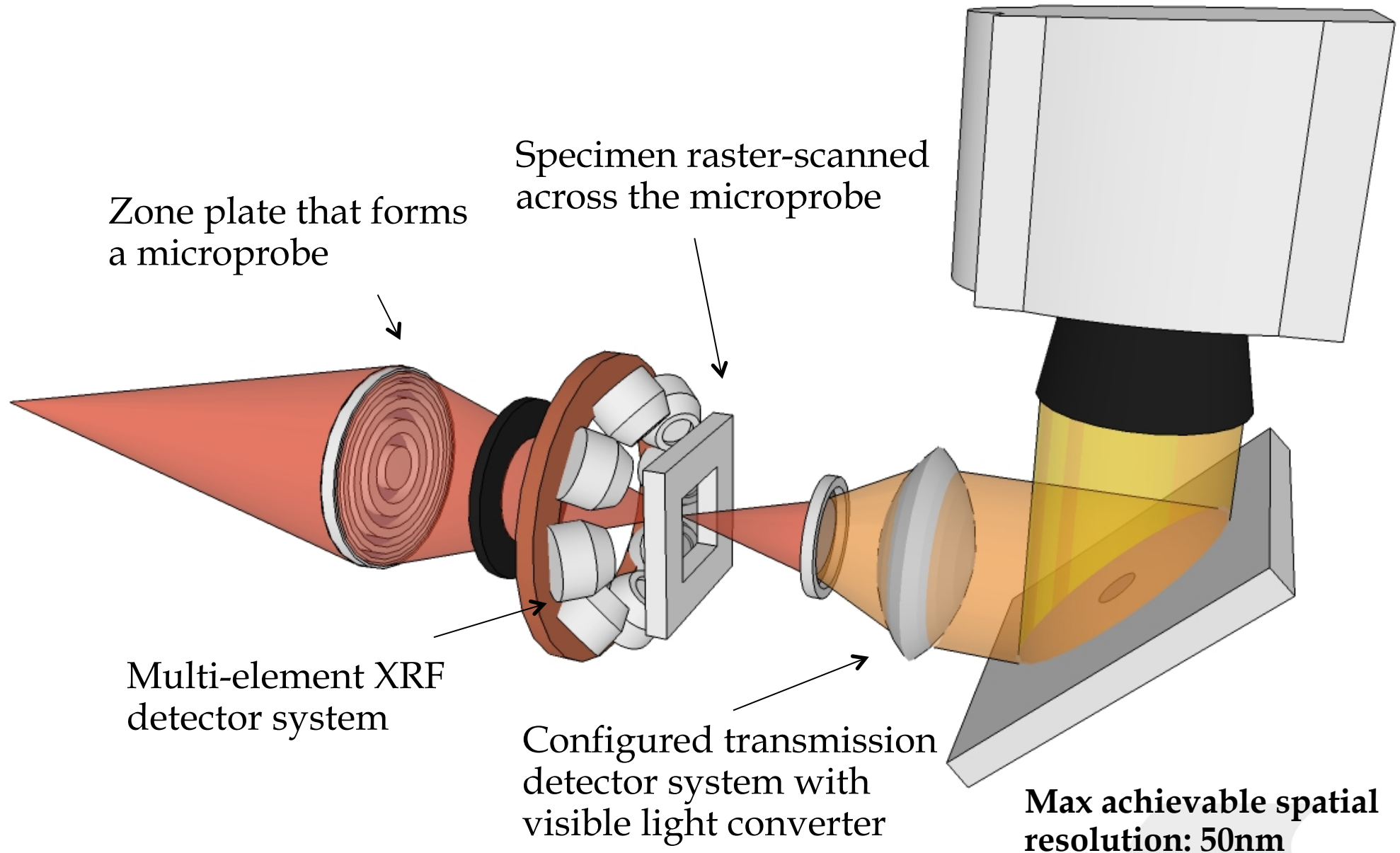
TwinMic – Combination of scanning and full-field imaging in a single instrument



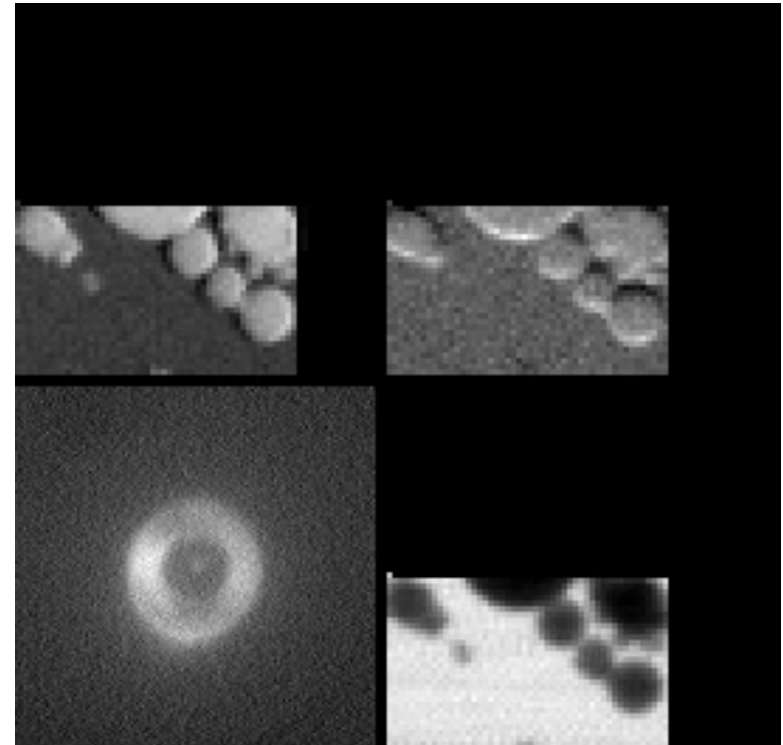
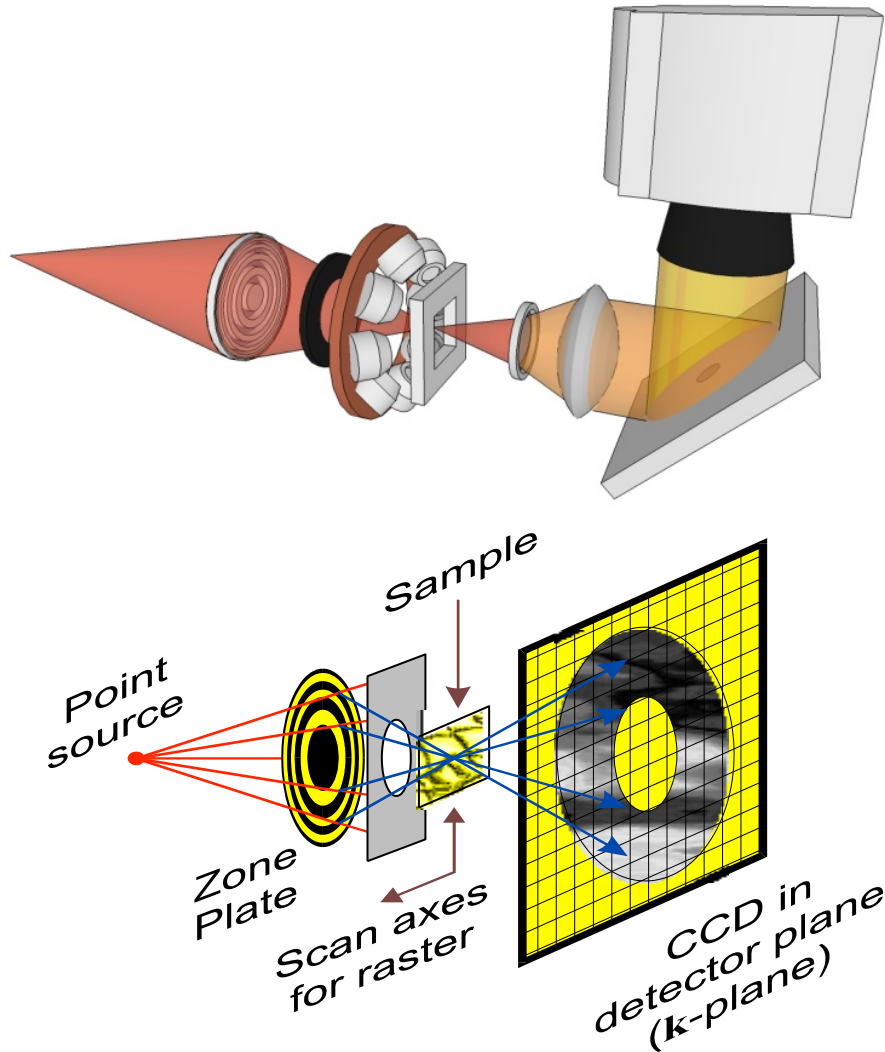
- Biotechnology
- Nanotechnology
- Environment
- Geochemistry
- Food Science
- Medicine
- Pharmacology
- Cultural Heritage
- New Materials



Scanning X-ray microscope (STXM)



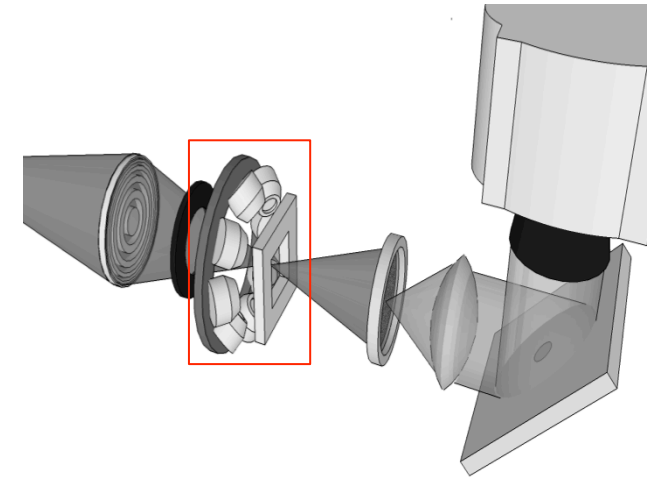
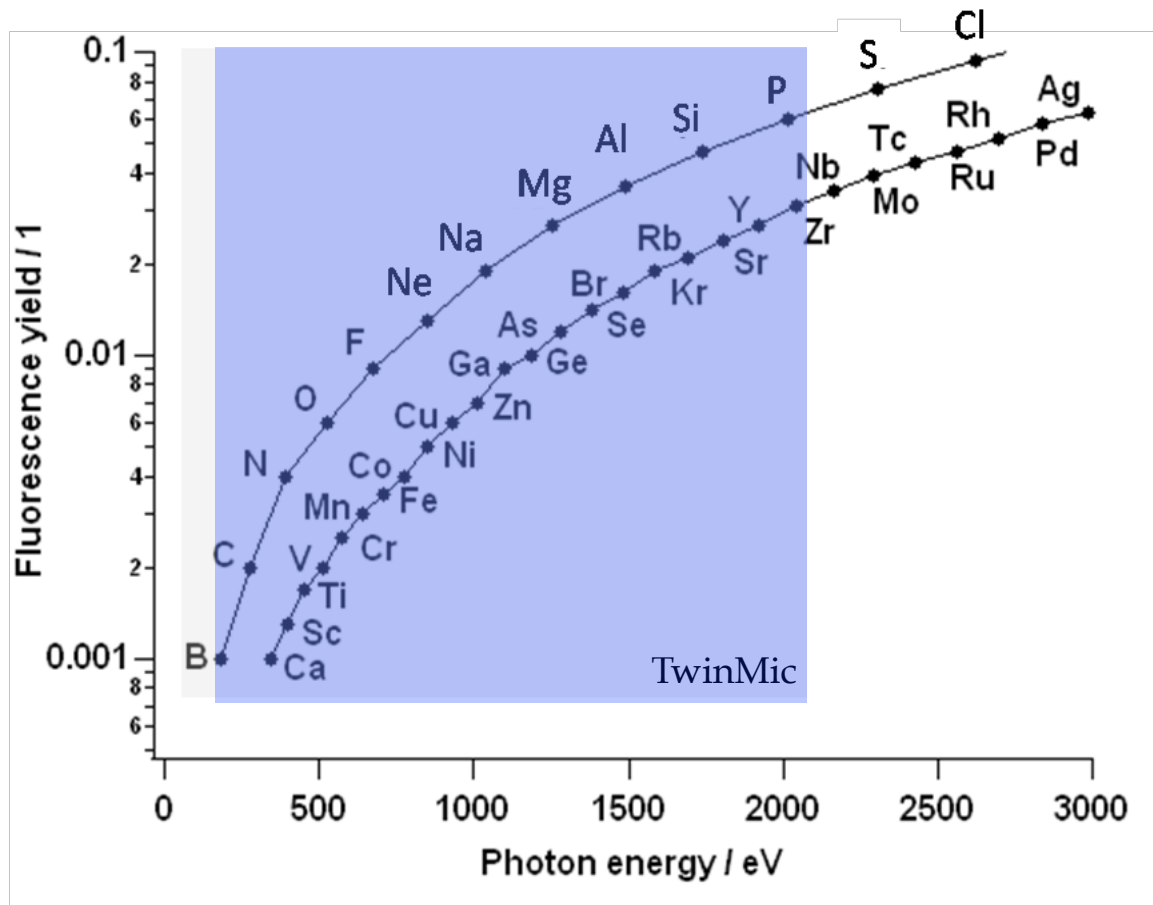
Differential phase contrast with a fast read-out CCD camera



Simultaneous acquisition of:

- Absorption or transmission
- Differential phase contrast
- Darkfield images

Low-energy X-ray fluorescence for elemental analysis:

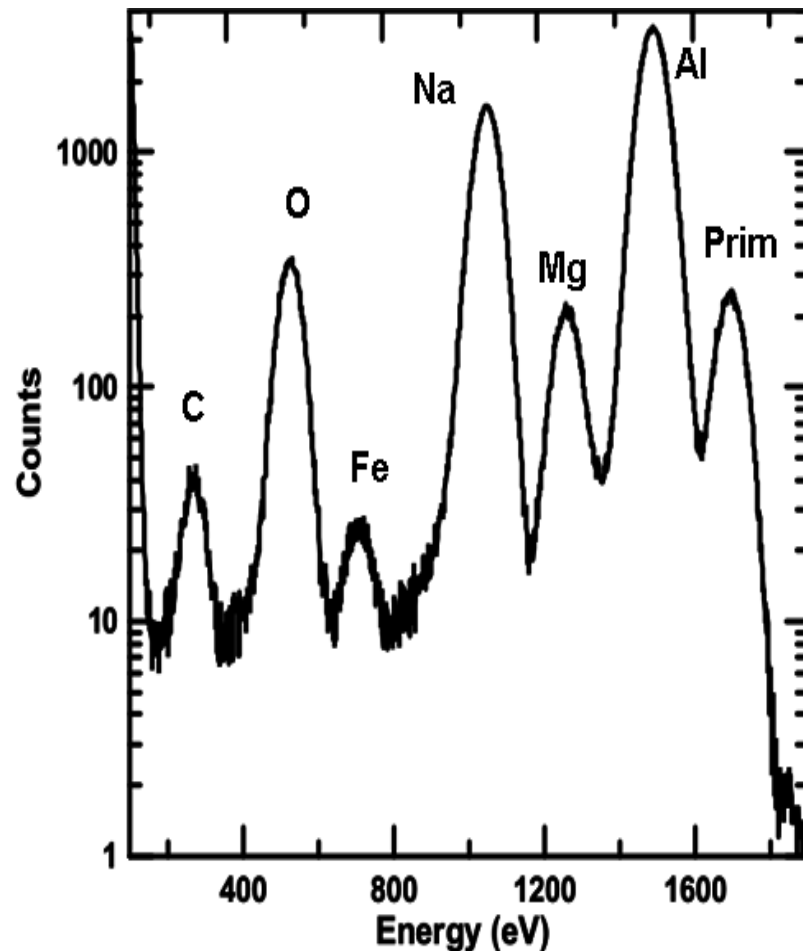


Detecting trace elements:

X-ray fluorescence: ~1000x better sensitivity than electrons for trace elemental mapping (ion concentrations etc.).

Low fluorescence yields for soft X-rays!!

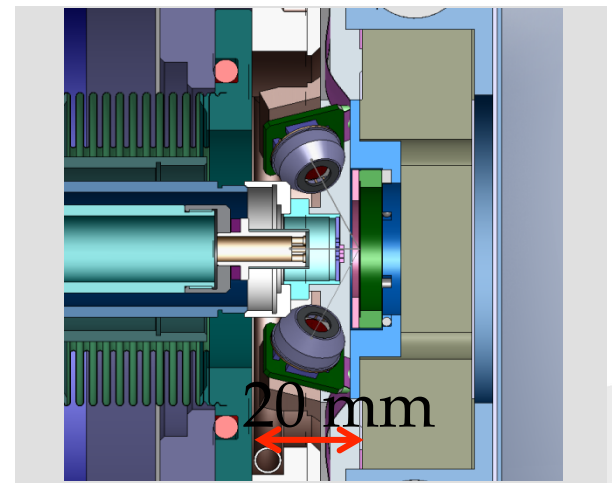
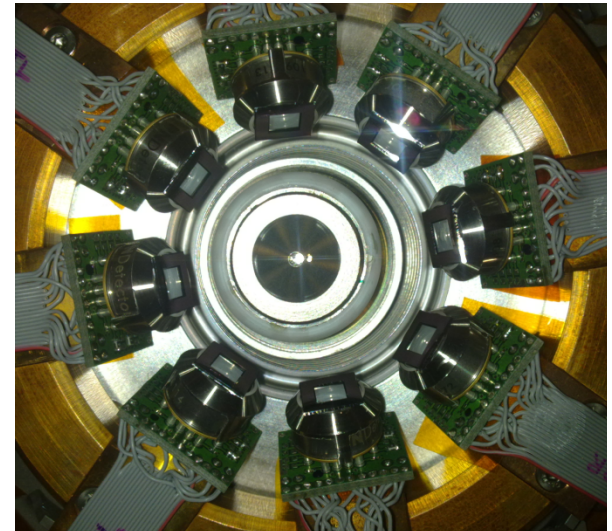
Low-energy X-ray fluorescence:

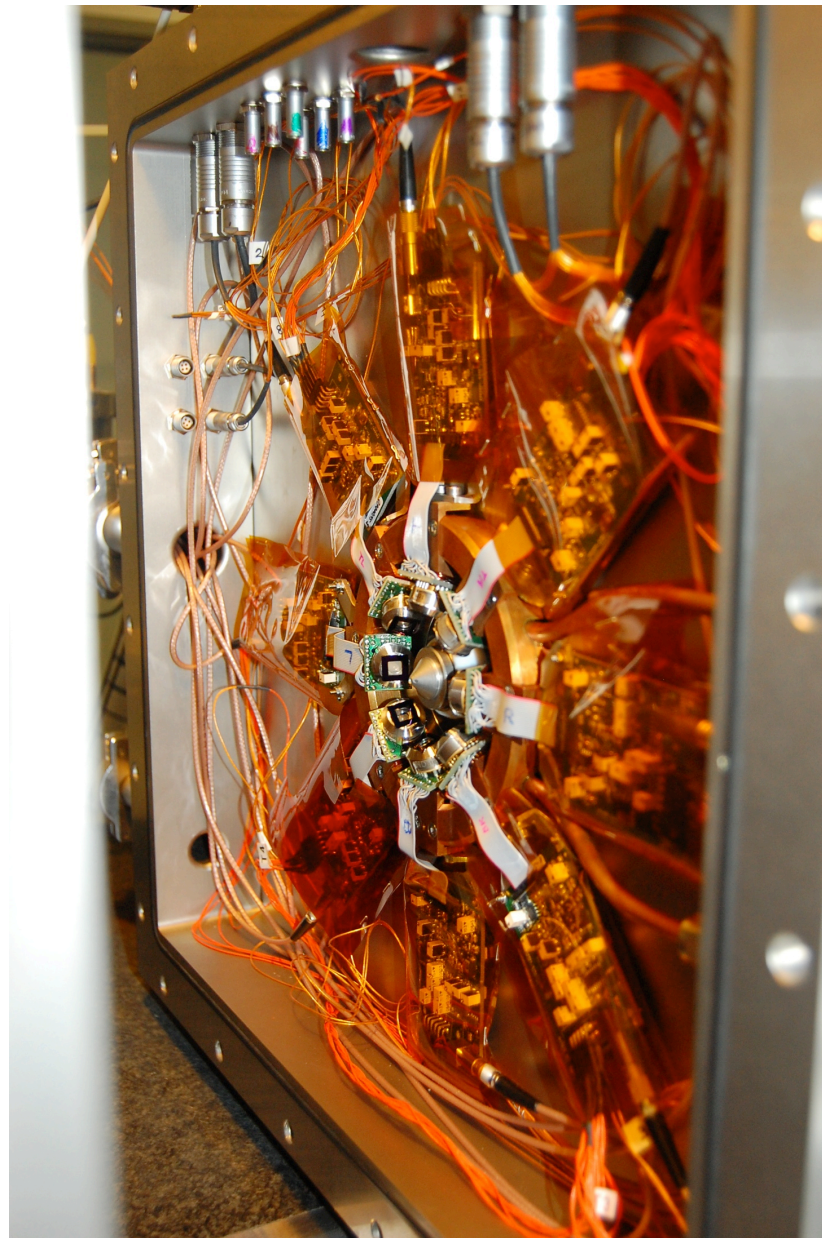


TwinMic LEXRF spectrum with unfocused beam of a test organic matrix on a metal shim

Dynamic range: up to 30 kcounts/s

Average FWHM energy resolution @ C- K edge: 69 eV



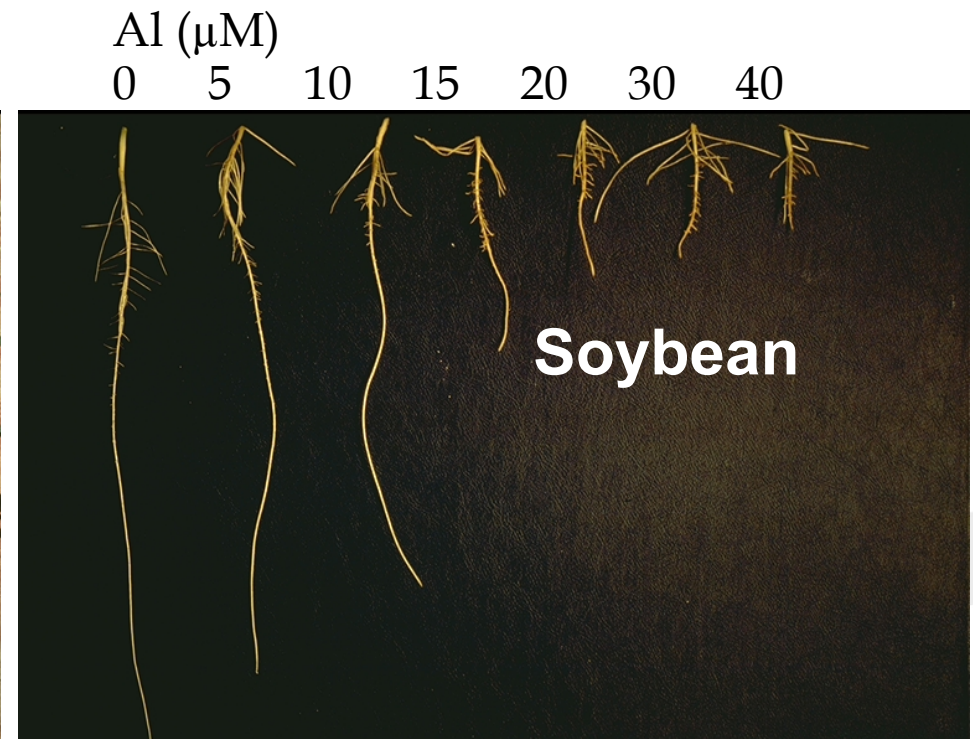


Aluminium toxicity

Soluble Al – “the most important growth-limiting factor for plants in most strongly acid soils and mine spoils” **Foy (1984)**

Acid soils occupy ~ 40 billion hectares (~ 30 %) of the world's ice free land area
von Uexküll and Mutert (1995)

In Australia alone, acid soils cost \$1.5 billion p.a. in lost productivity

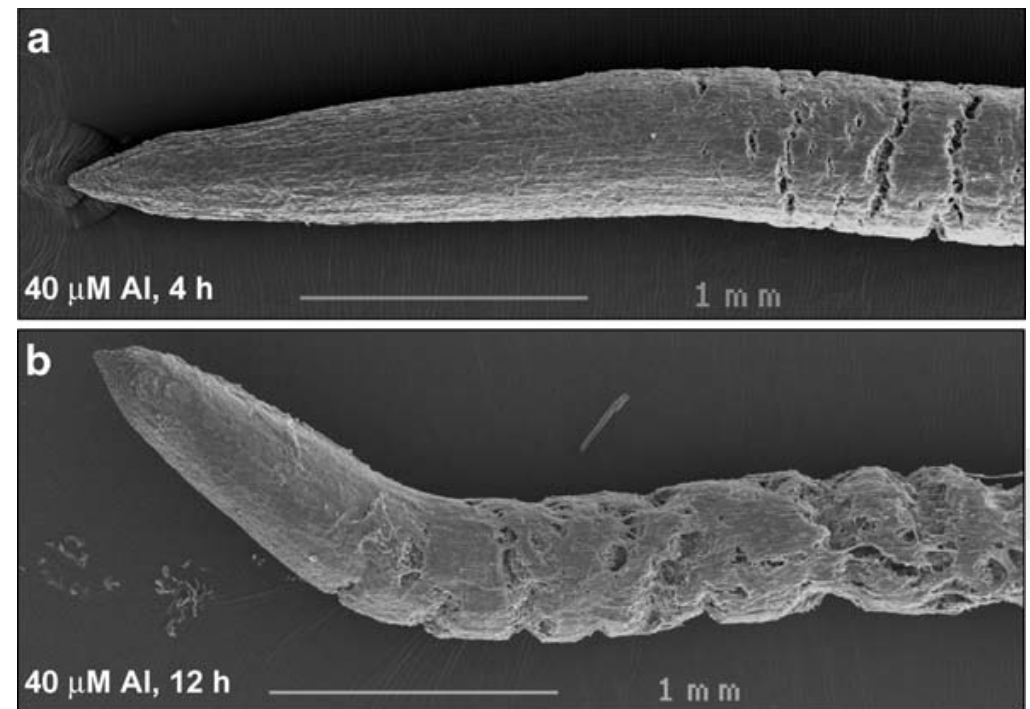
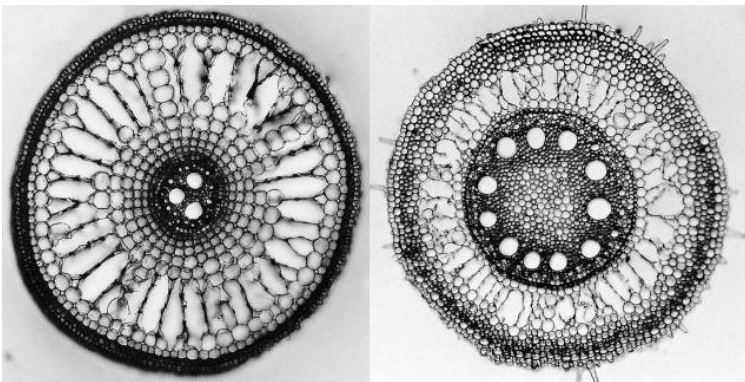


Aluminium toxicity

Soluble Al – “the most important growth-limiting factor for plants in most strongly acid soils and mine spoils” **Foy (1984)**

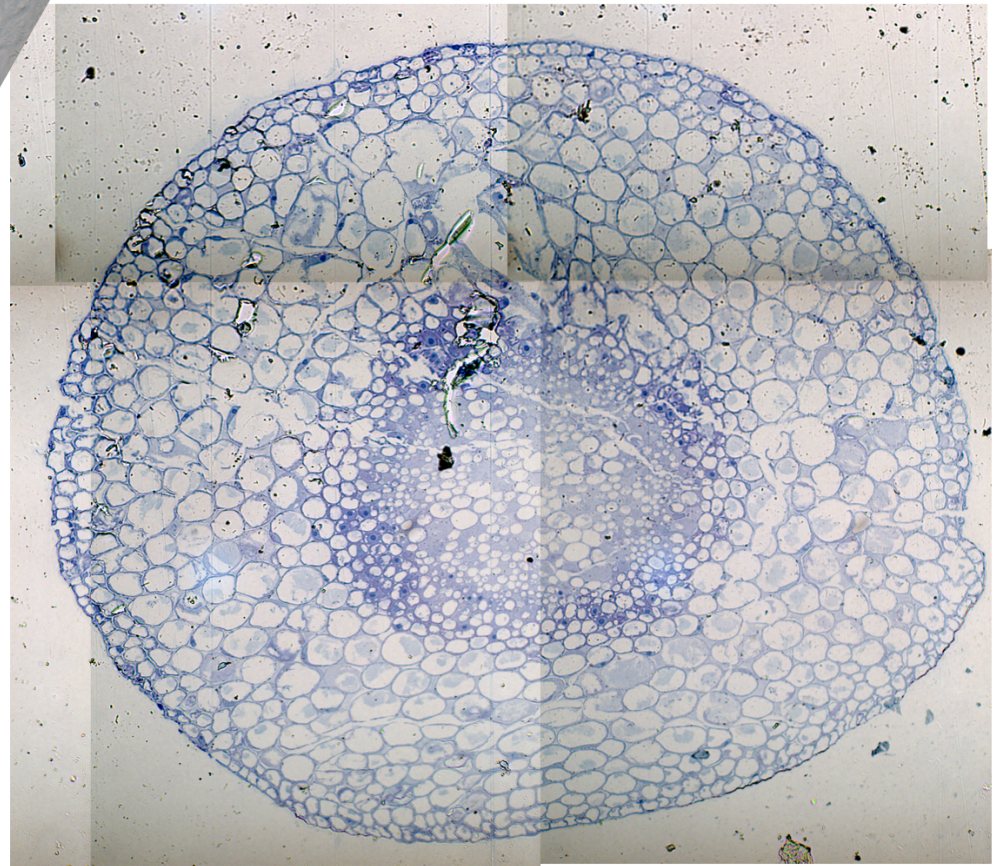
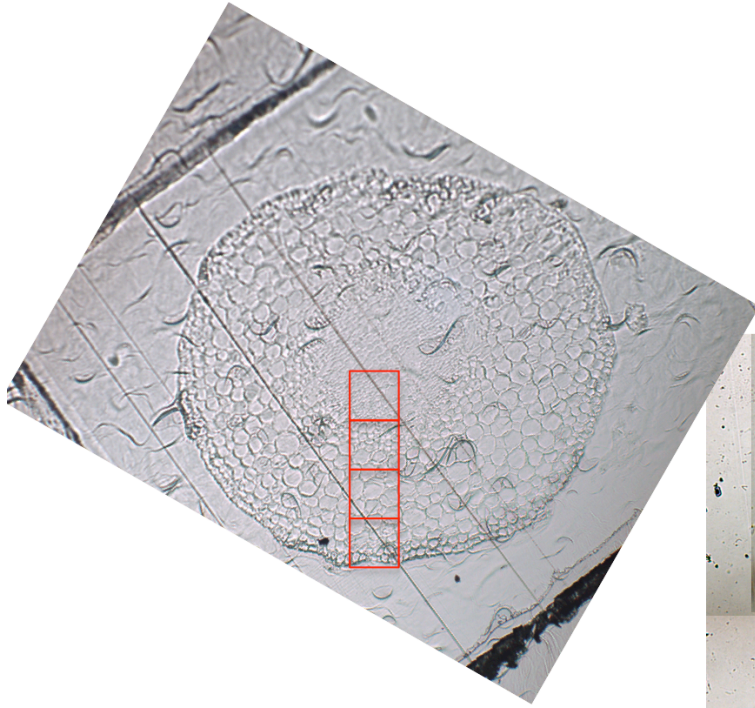
Although known since 1904 that Al is the primary factor causing a reduction in plant root growth in acid soils, the mechanism by which Al is toxic remains unclear

Recent research (2014) has shown that Al exerts its toxic effects very quickly, reducing root growth in ≤ 30 min. Therefore, a crucial step in elucidating how Al exerts its toxic effects is to examine where the Al is accumulating within the roots



Aluminum toxicity

30 minutes, 6 mm, Sample 1



7 μm -thick transverse cross section of soybean roots

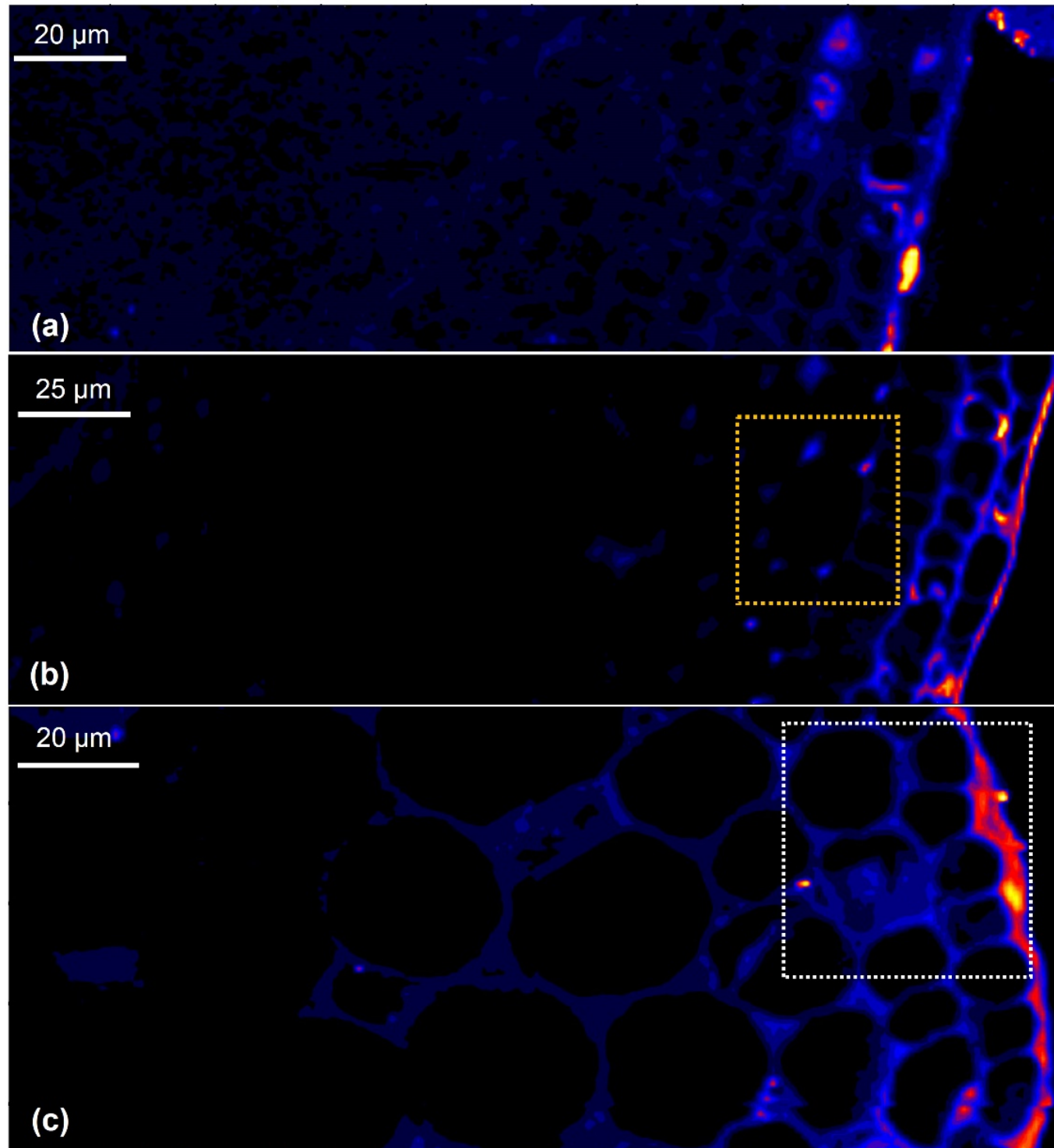
Exposed to 30 μM Al for 0.5 h.

30 μM Al
0.5 h

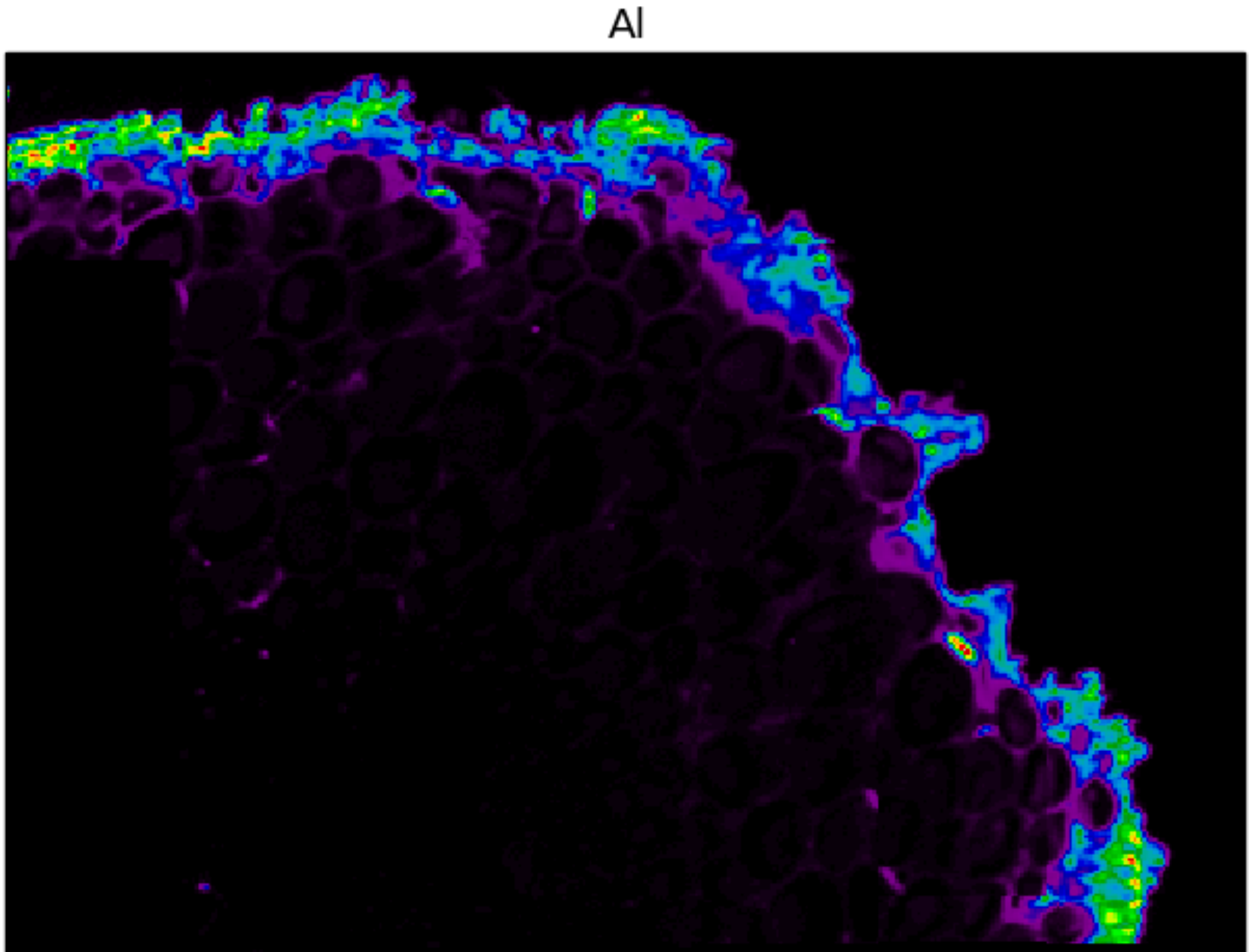
c) 6mm from apex

b) 2mm from Apex

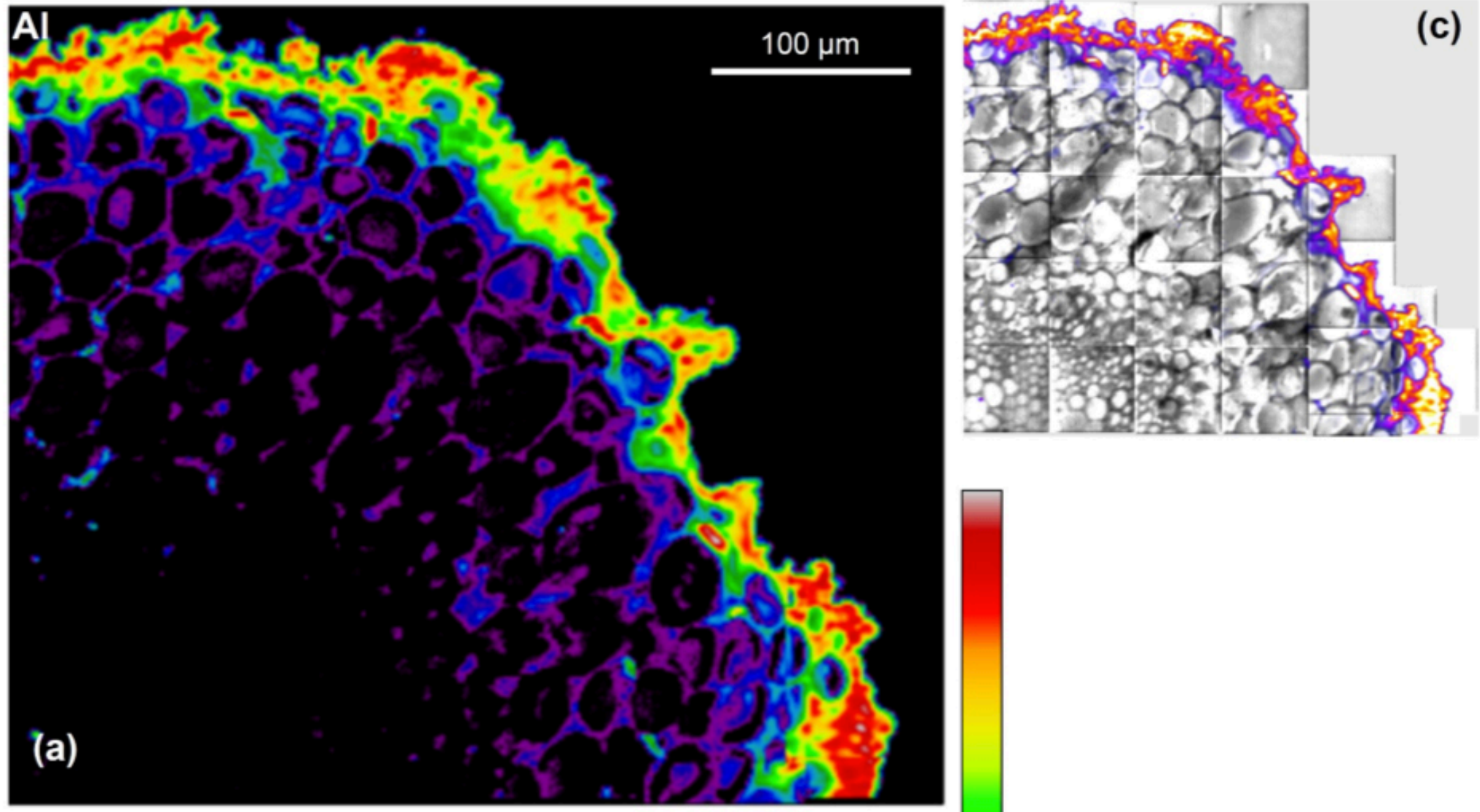
a) 0.5 mm from Apex



Soybean roots exposed to 30 μM Al for 24 h

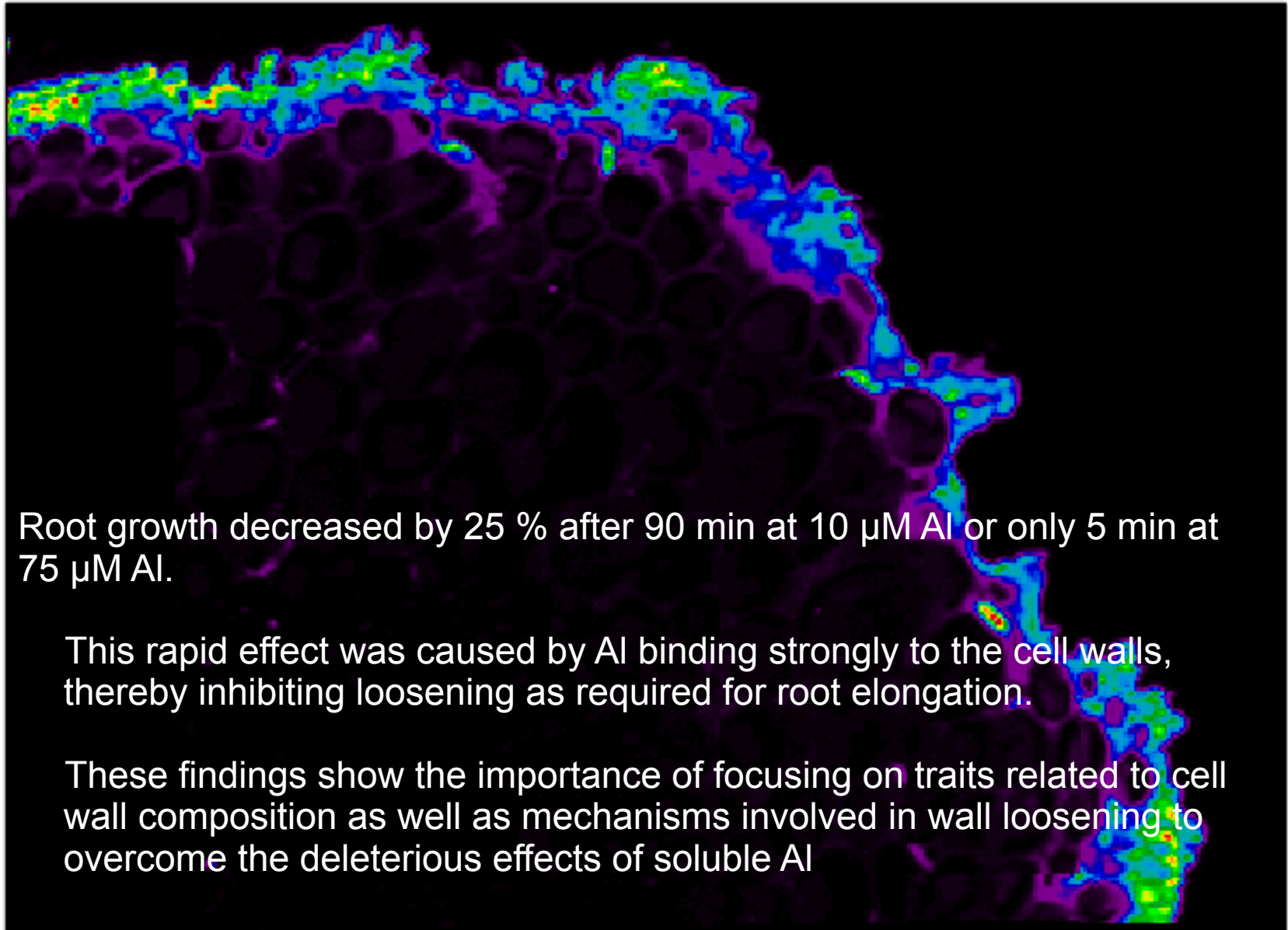


Soybean roots exposed to 30 μM Al for 0.5 h



Soybean roots exposed to 30 μM Al for 0.5 h

Al



Root growth decreased by 25 % after 90 min at 10 μM Al or only 5 min at 75 μM Al.

This rapid effect was caused by Al binding strongly to the cell walls, thereby inhibiting loosening as required for root elongation.

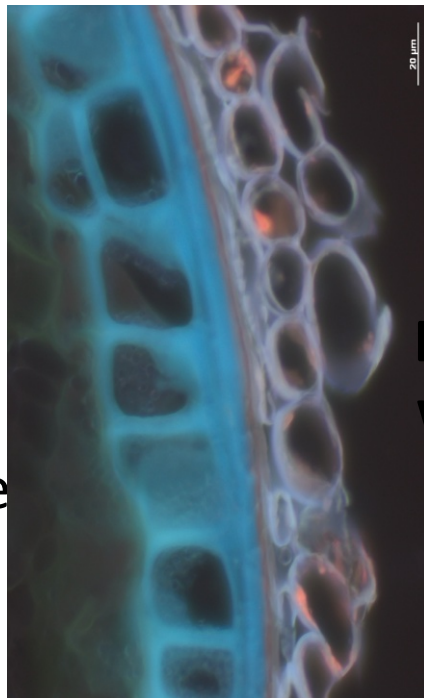
These findings show the importance of focusing on traits related to cell wall composition as well as mechanisms involved in wall loosening to overcome the deleterious effects of soluble Al

Food Science: Inside the wheat

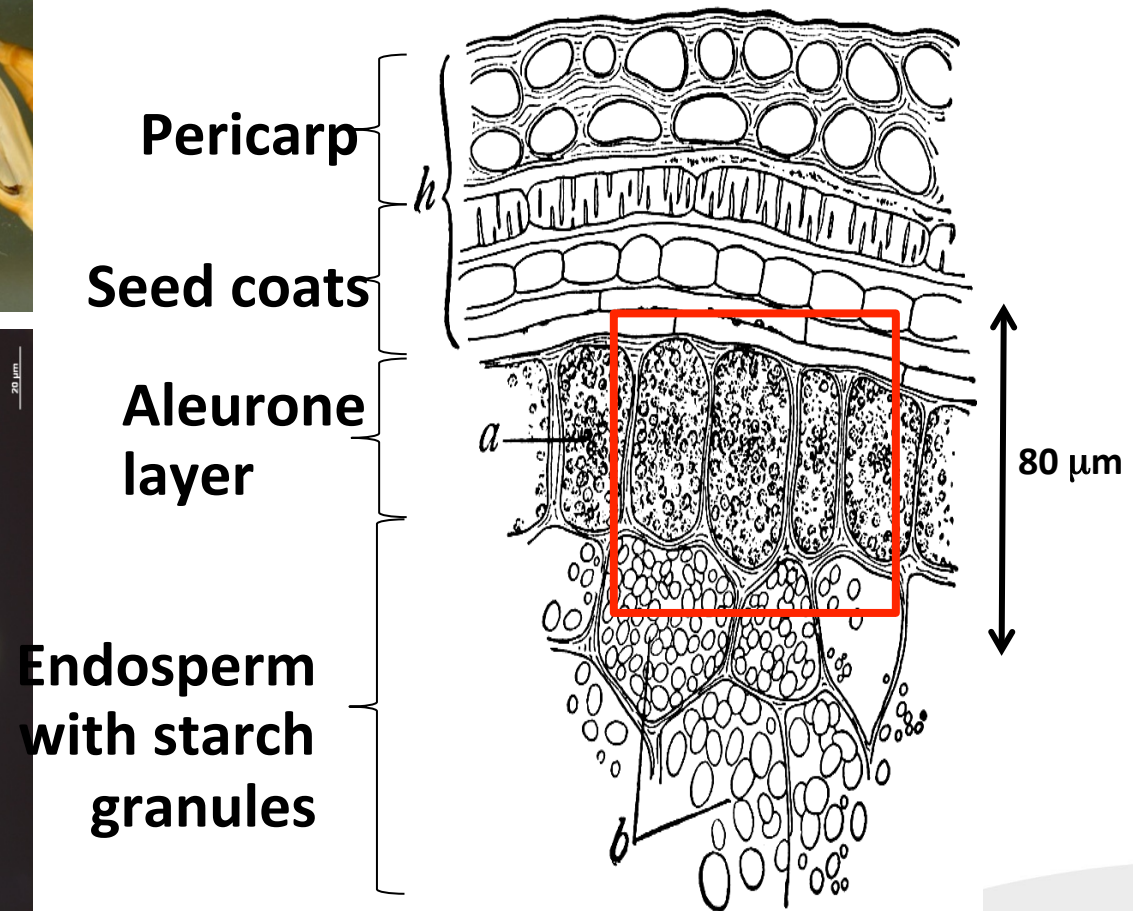


Ivan Kreft,
University Ljubljana

Functionality and toxicity of Zn in wheat and buckwheat analyzed on sub-cellular level



Structure of a wheat grain



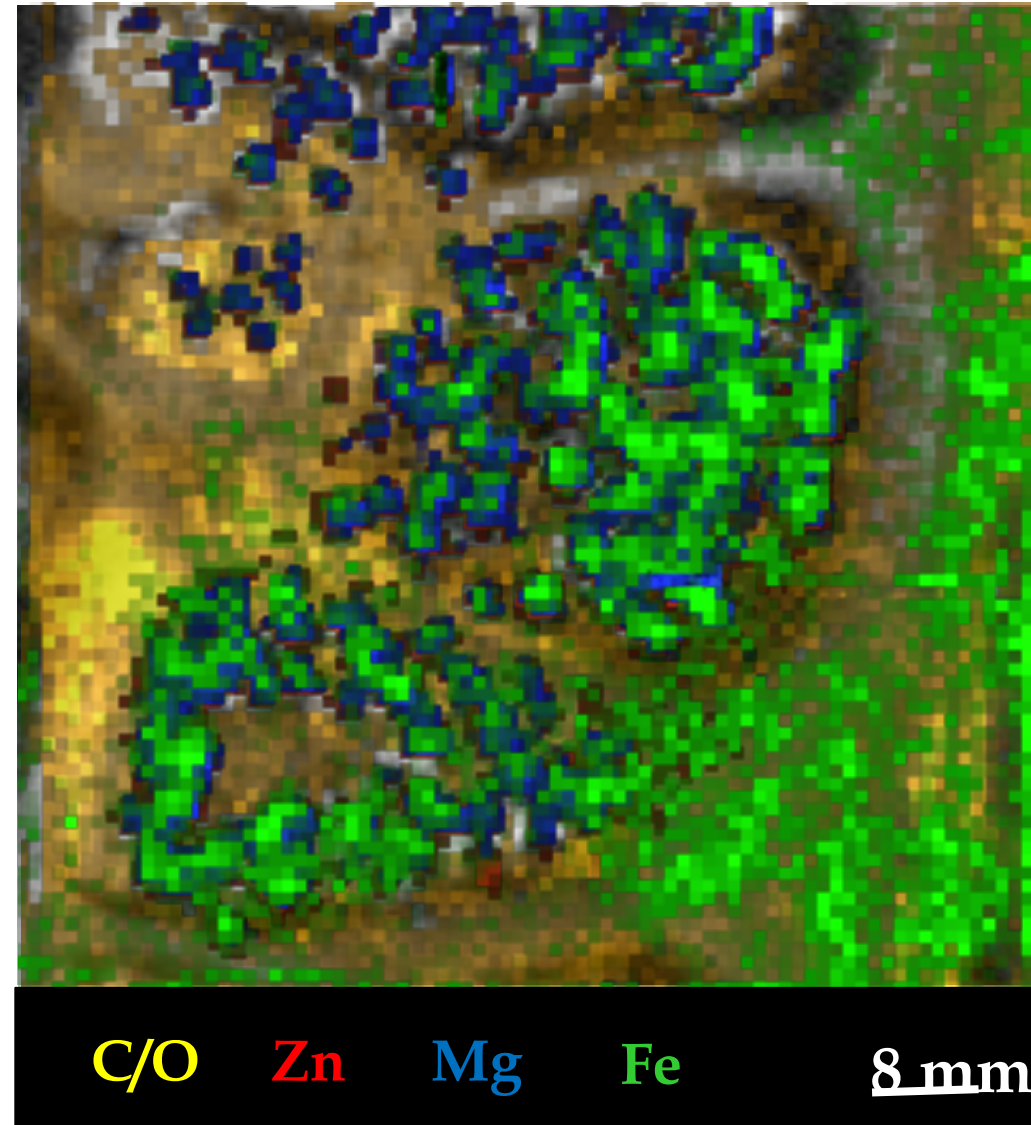


*Ivan Kreft,
Fac. of Biotechnology,
University Ljubljana*

**Functionality and
toxicity of Zn in
wheat and buckwheat
analyzed on sub-
cellular level**

**Healthy
control
wheat**

**E=1686 eV
80 x 80 mm²
80 x 80 px
8 s dwell/ px
1 mm
resolution
4 detectors**

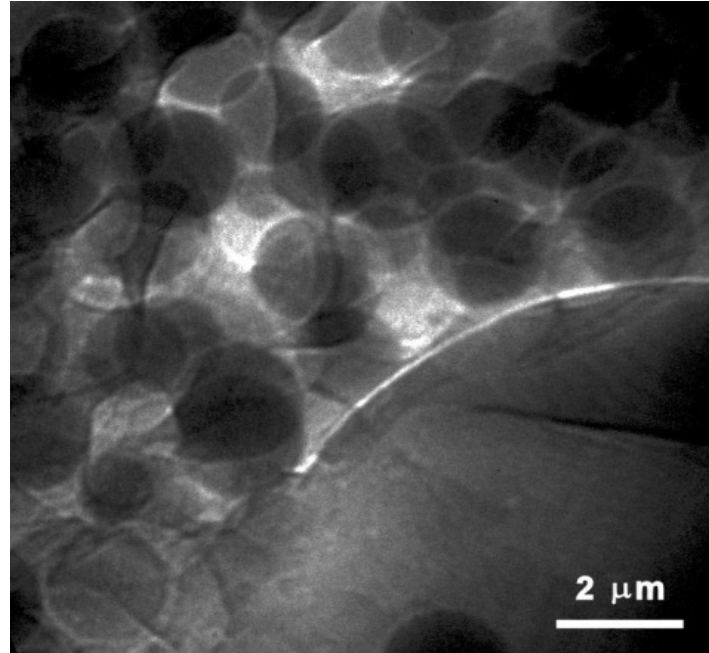


Biogenetics and Food Science: Inside the wheat

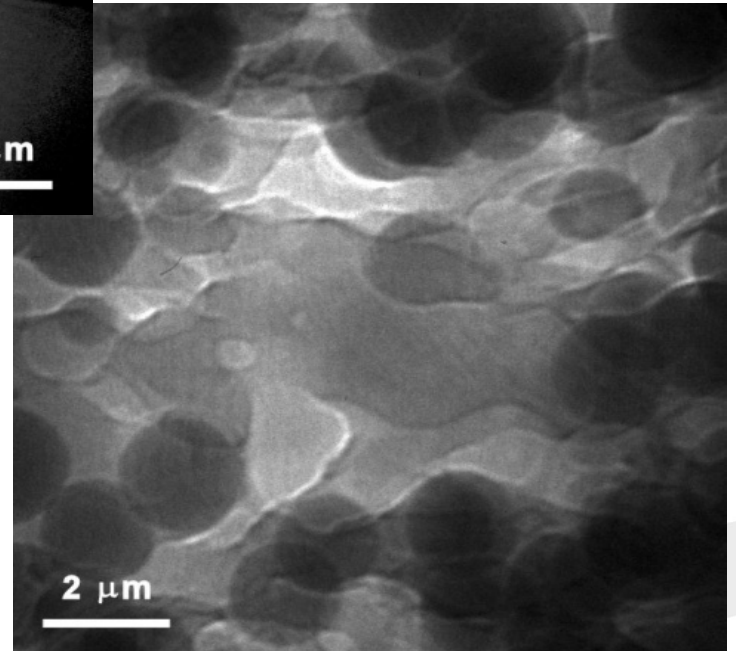


*Ivan Kreft,
Fac. of Biotechnology
University Ljubljana*

Functionality and
toxicity of Zn in
wheat and buckwheat
analyzed on sub-
cellular level



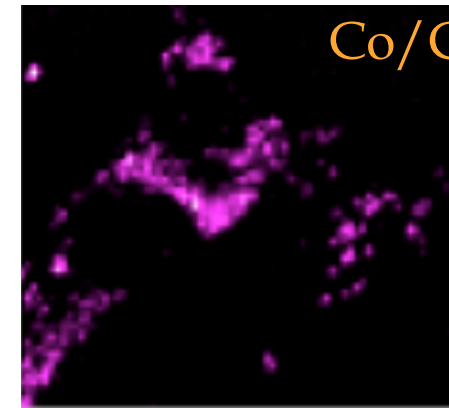
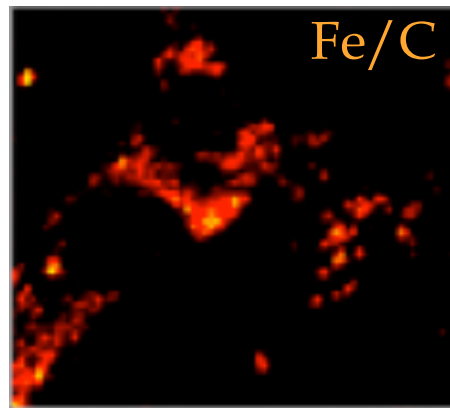
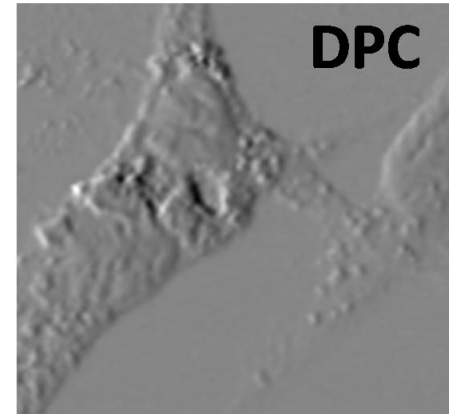
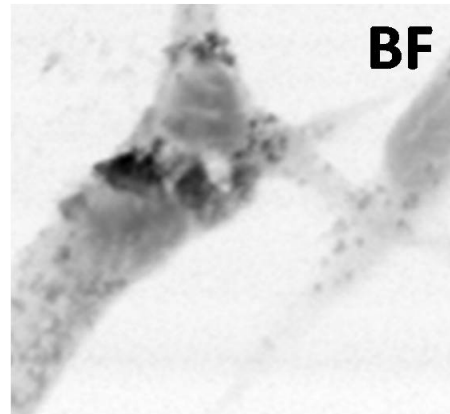
1s dwell, 740 eV photon
energy



TXM images acquired
with a double-
frequency ZP (15nm
outermost zone width
from J. Vila-
Comamala (PSI)

Cellular distribution and degradation of CoFe_2O_4 NPs in Balb/3T3 Fibroblast cells

Localization of engineered nanoparticles (ENPs) inside a cell and on the possible effects on the cell metabolic behaviour

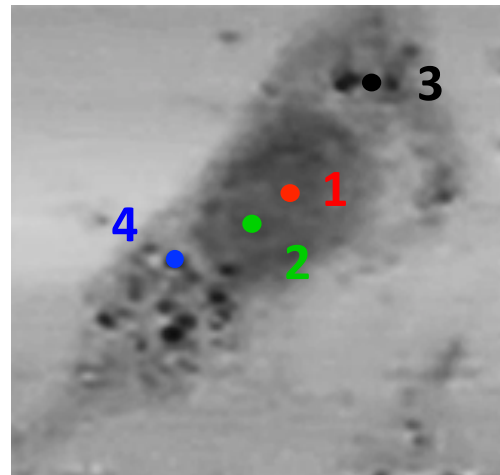


G. Ceccone,
P. Marmorato et al.,
EC Joint Research
Center, Ispra, I

CoFe_2O_4 in mouse 3T3 fibroblast cells, $E=2019$ eV, $60\mu\text{m} \times 60\mu\text{m}$

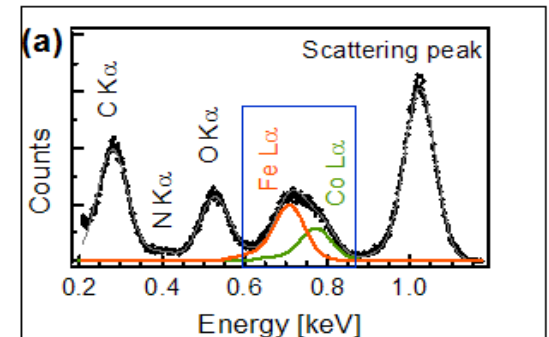
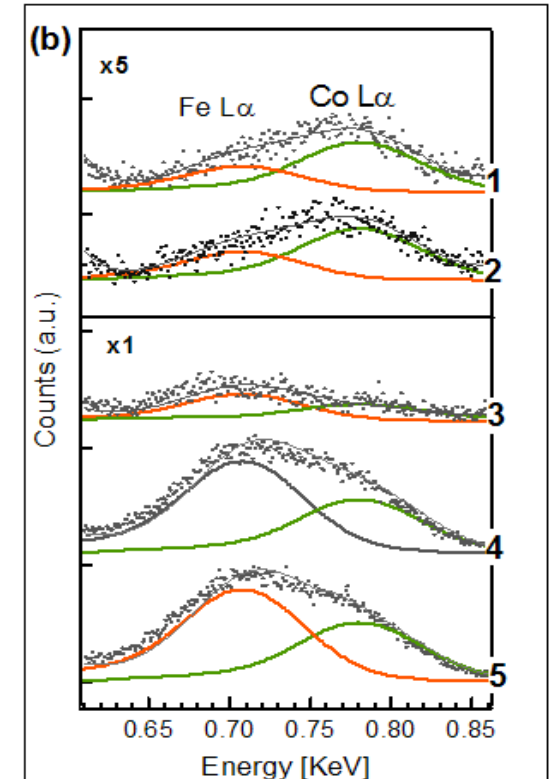
Balb/3T3 exposed to 1000mM

Fe/Co~0.8



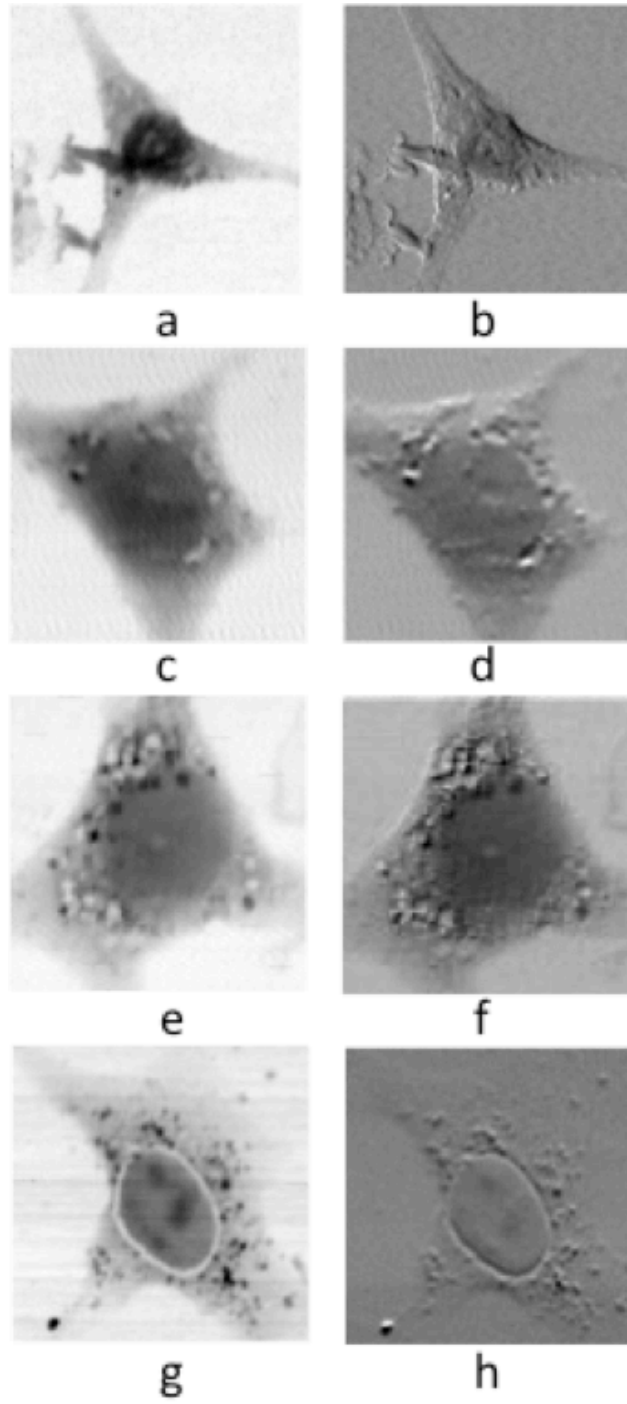
Fe/Co~1.5

Similar behaviour (but less evident) in the nuclear region for 500μM concentration





Elettra
Sincrotrone
Trieste



Control

40 μM

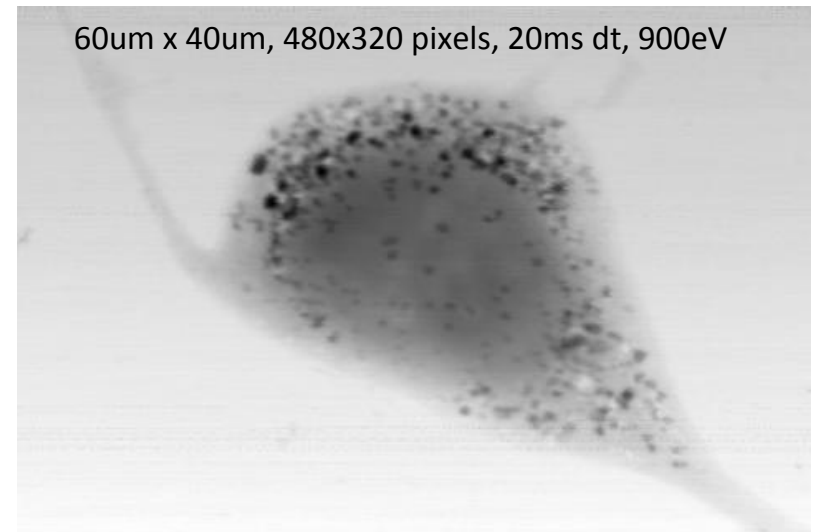
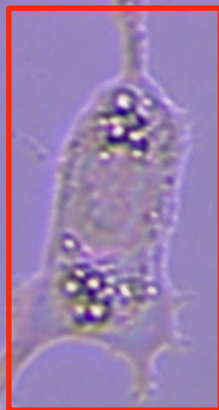
250 μM

500 μM



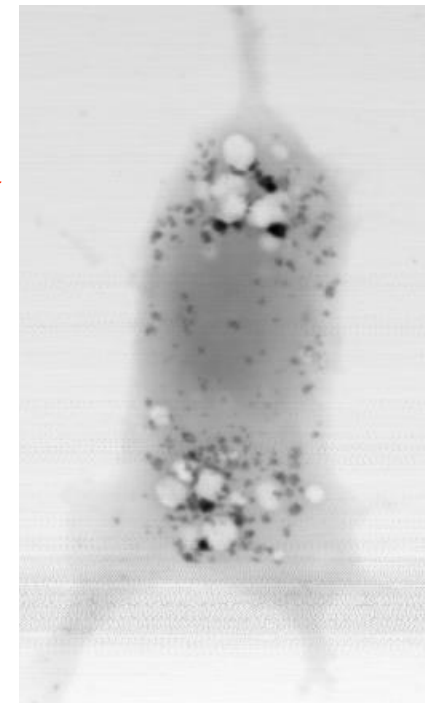
Elettra
Sincrotrone
Trieste

Fibroblast cells
exposed to
 CoFe_2O_4 NPs



60um x 40um, 480x320 pixels, 20ms dt, 900eV

32um x 60um, 256x480 pixels, 20ms dt, 900eV

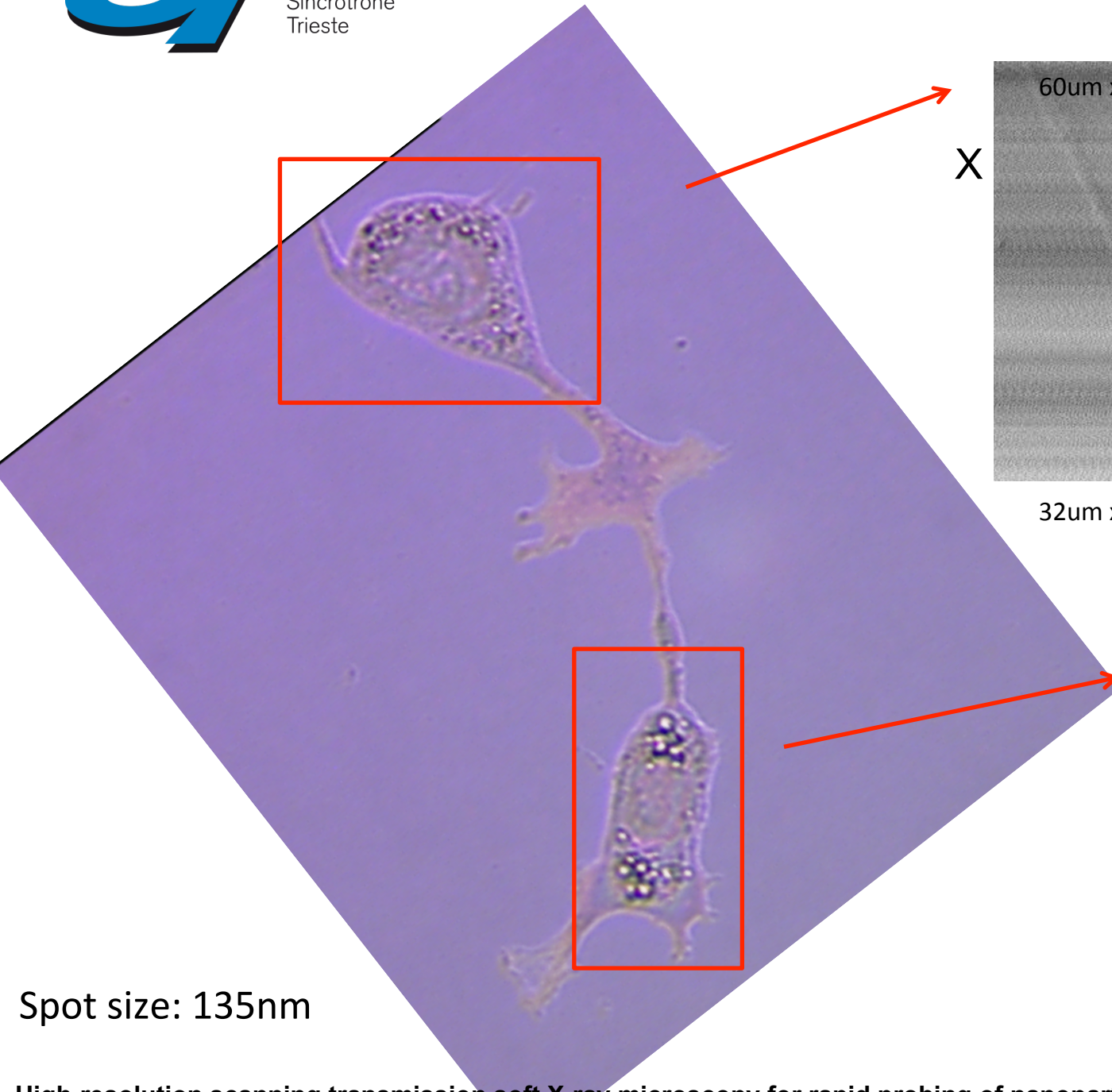


Spot size: 135nm

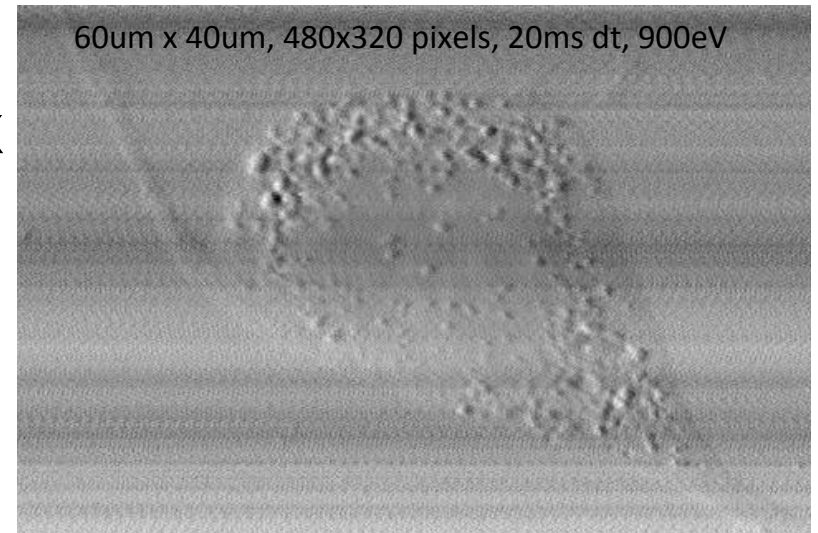
High-resolution scanning transmission soft X-ray microscopy for rapid probing of nanoparticle distribution and sufferance features in exposed cells Kourousias G, Pascolo L, Marmorato P, Ponti J, Ceccone G, Kiskinova M, Gianoncelli A *X-Ray Spectrometry* (2015)



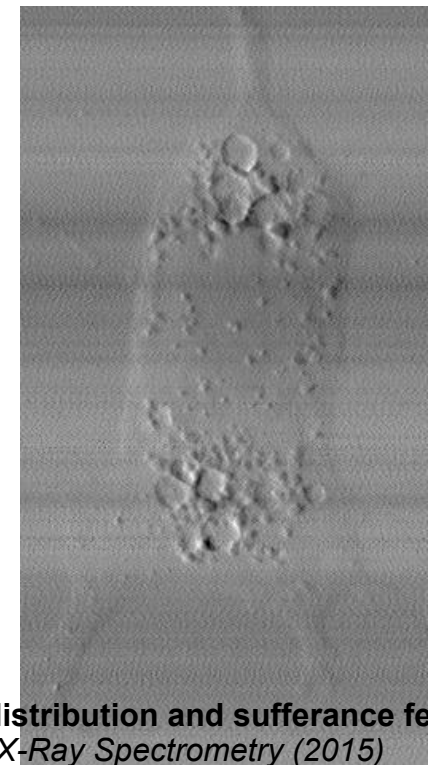
Elettra
Sincrotrone
Trieste



X



32um x 60um, 256x480 pixels, 20ms dt, 900eV



X

Spot size: 135nm

High-resolution scanning transmission soft X-ray microscopy for rapid probing of nanoparticle distribution and sufferance features in exposed cells Kourousias G, Pascolo L, Marmorato P, Ponti J, Ceccone G, Kiskinova M, Gianoncelli A *X-Ray Spectrometry* (2015)

Red oil specifically stains lipids

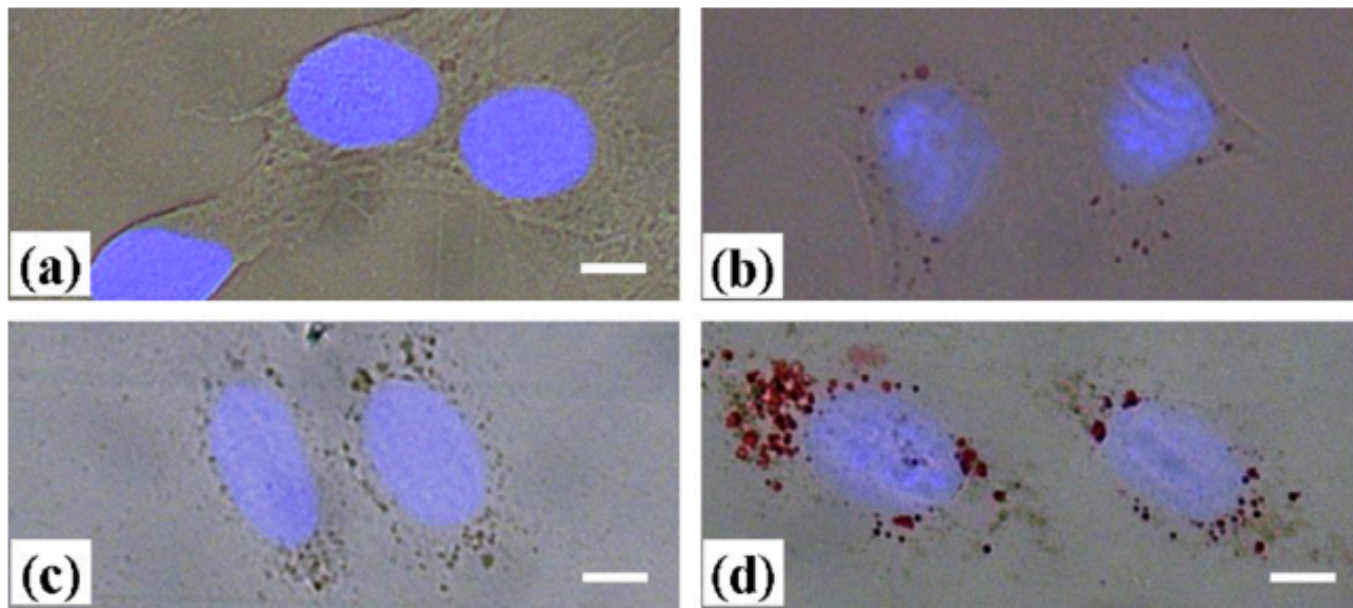
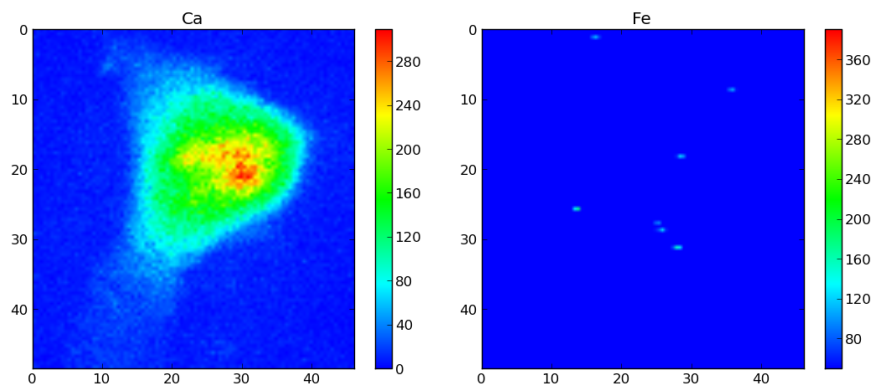


Fig. 6. Optical images of Balb/3T3 control cells (a and b) and incubated for 24 h with 500 μM CoFe_2O_4 NPs suspension (c and d). Red spots represent lipids stained by Red Oil O solution (b and d) whilst nuclei are stained in blue by Hoechst. Bar = 10 μm . (For interpretation of the references to color in this figure legend, the reader is referred to the web version of the article.)

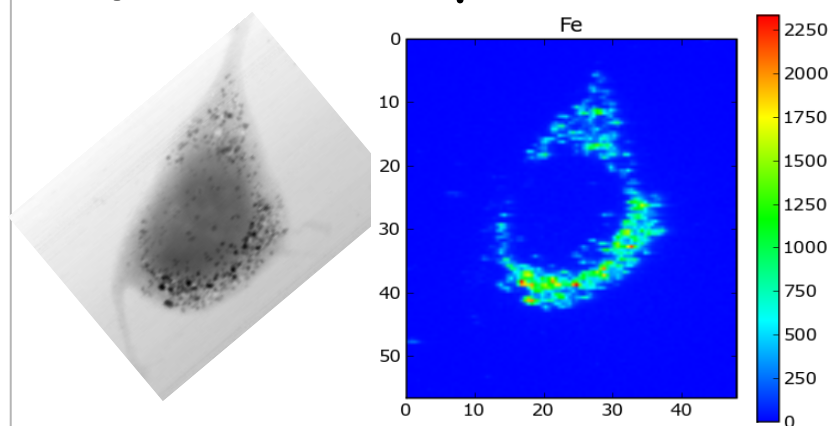


Nanotoxicology: CoFe_2O_4 ENPs

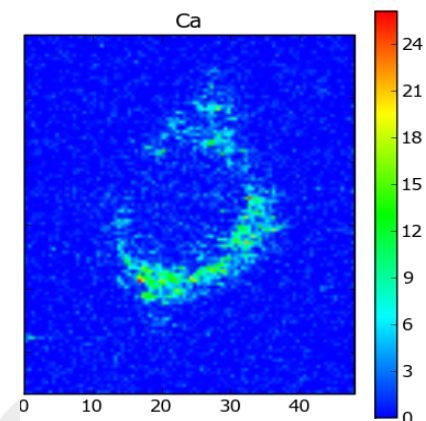
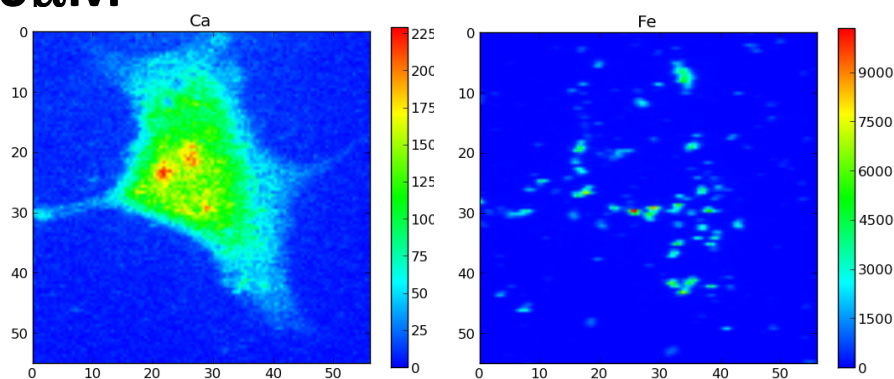
Control



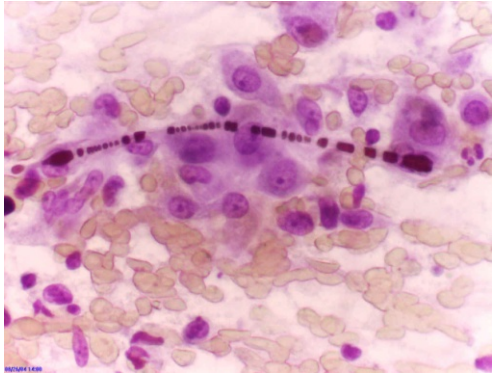
Exposed to 500 μM



Exposed to 40 μM

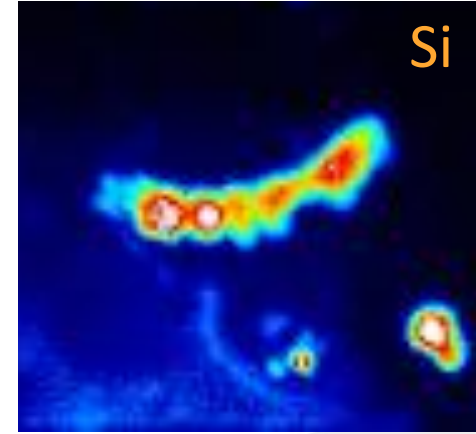
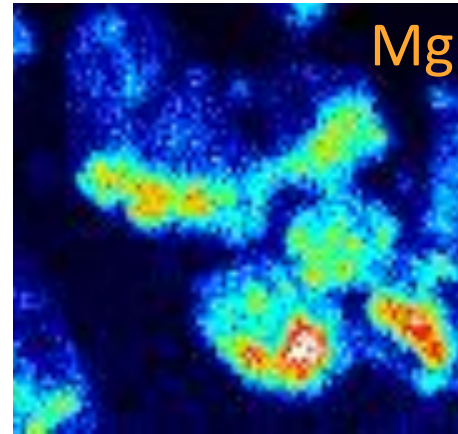
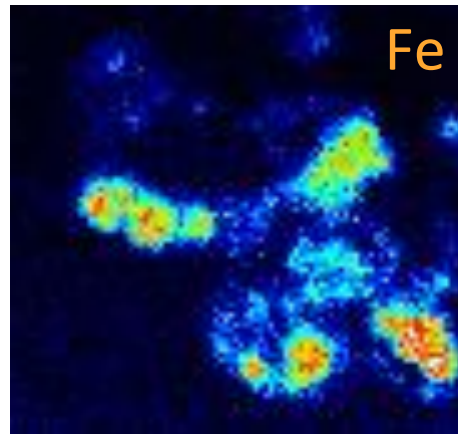
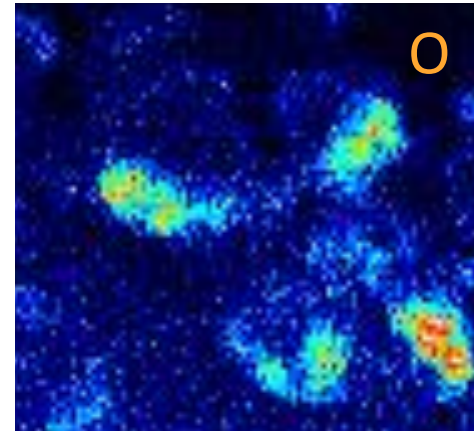
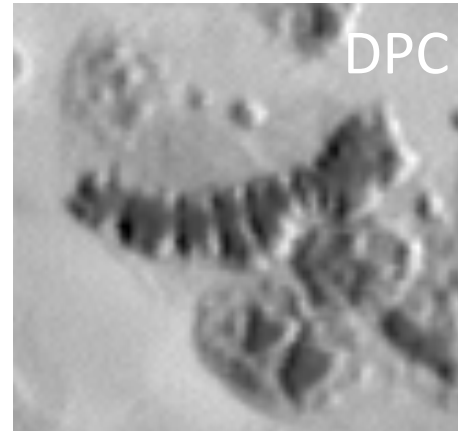
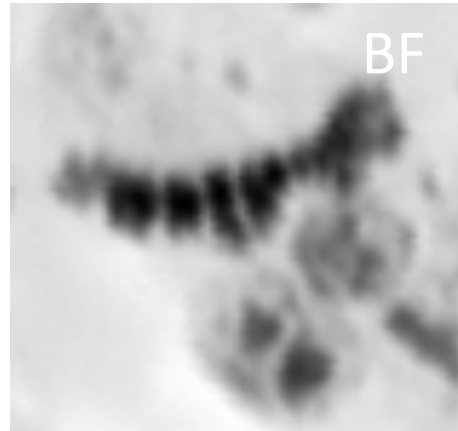


Exposure to Asbestos



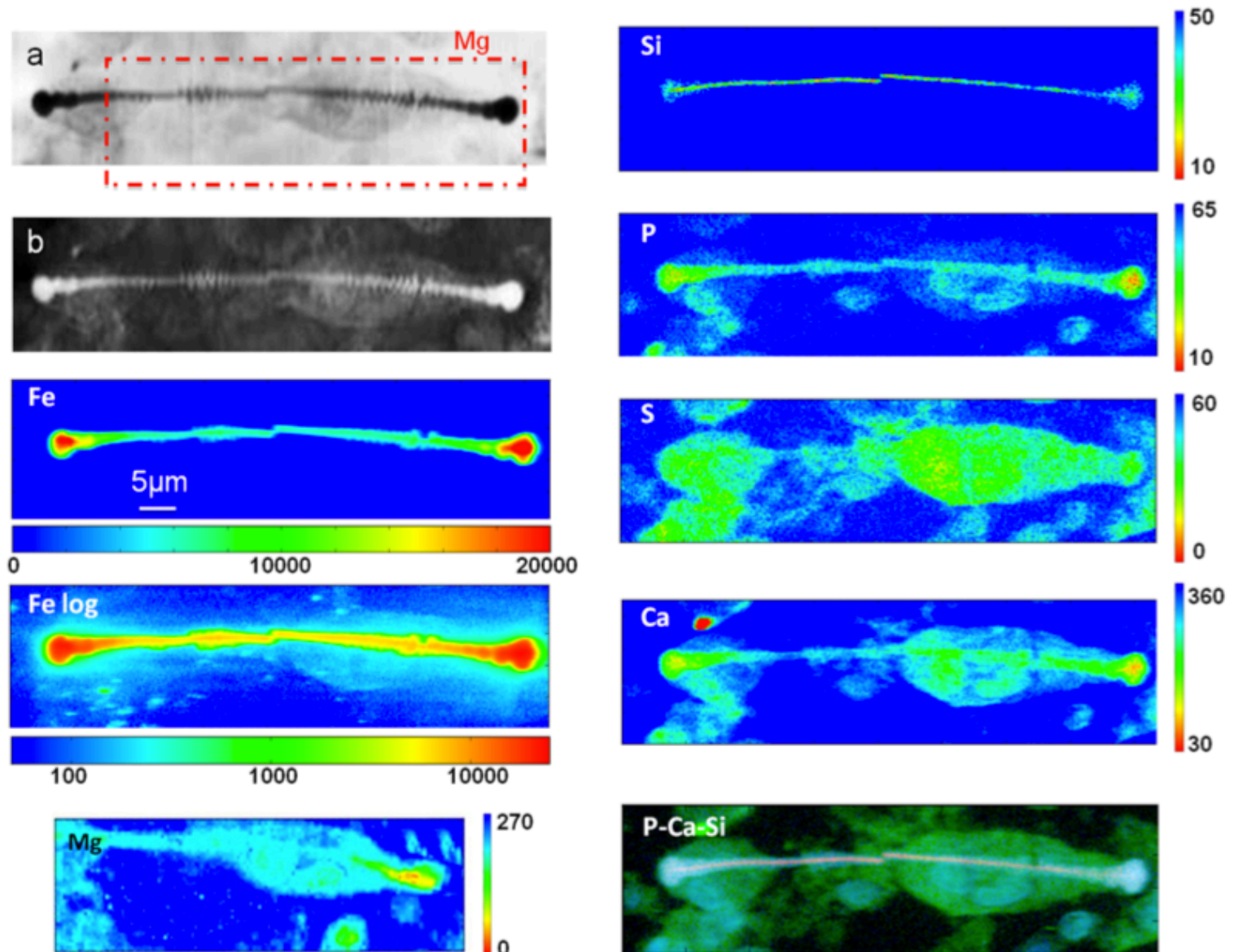
*L. Pascolo, M. Melato,
Burlo Hospital, Trieste,
Italy*

Mesothelioma and
differentiation of lung
tissue due to
asbestos;
the role of Mg



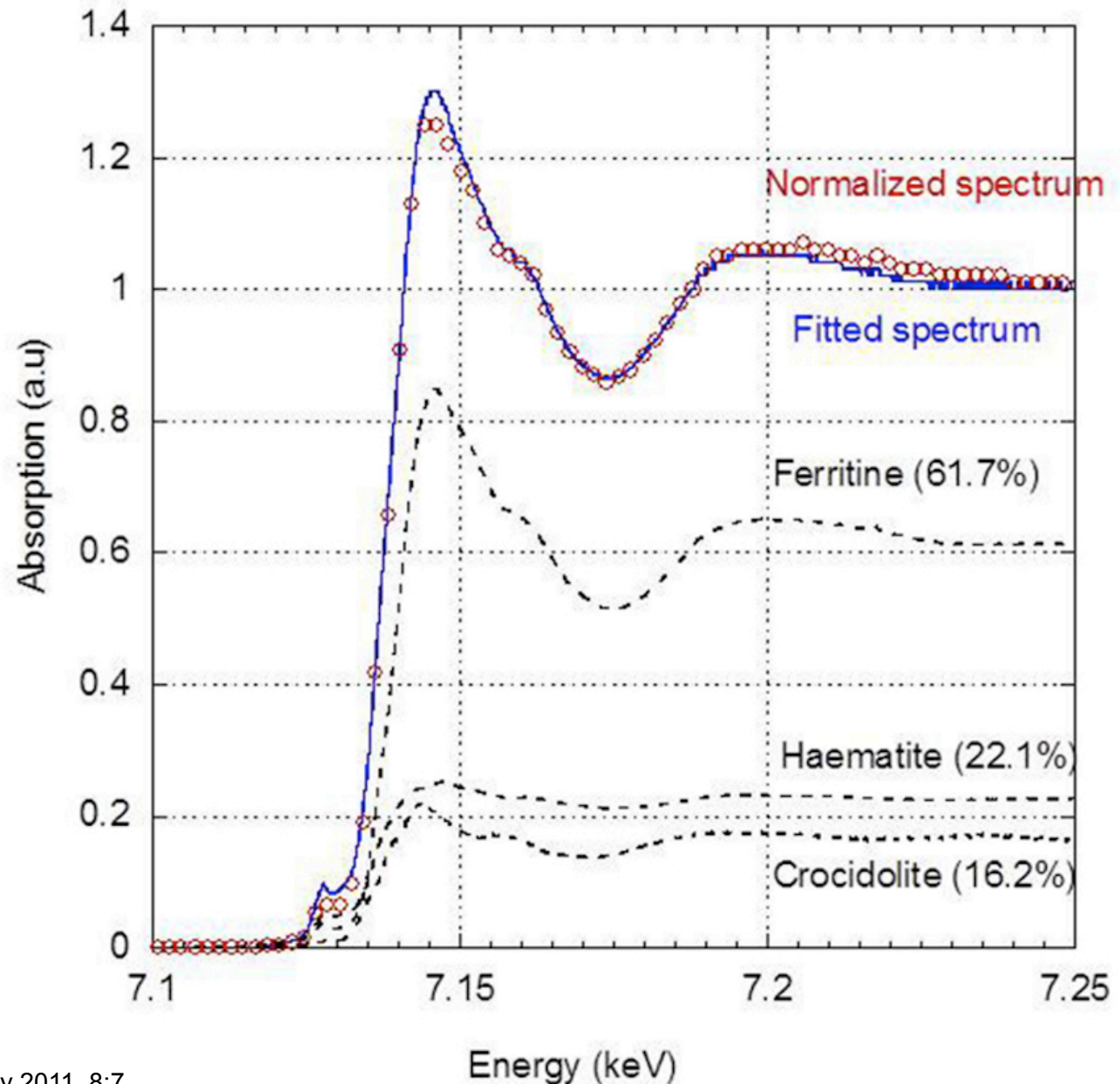
E=2019 eV, 50mm x 50 mm, 100 x 100 pixels, 15s/pixel LEXRF,
4 SDDs

Tissue with a phagocytated asbestos fibre.



Fe K-edge XANES measured in selected ~ 1 mm² spots of an asbestos body

Figure 6



- Most of the Fe detected around asbestos fibres (coating and ferruginous bodies) is compatible with the presence of ferritin and the Fe³⁺ oxidation state of iron.
- The most novel and intriguing result was the detection of significant percentages of haematite in the asbestos bodies that we suppose is the results of ferritin transformation occurring during the long residence time in the asbestos bodies in the lung tissues.



First real Clinical case at TwinMic

OPEN

SUBJECT AREAS:

PATHOGENESIS

BIOPHYSICS

CHEMICAL MODIFICATION

Received
19 May 2014

Accepted
9 September 2014

Published
7 October 2014

Calcium micro-depositions in jugular truncular venous malformations revealed by Synchrotron-based XRF imaging

Lorella Pascolo¹, Alessandra Gianoncelli², Clara Rizzardi³, Veronica Tisato⁴, Murielle Salomé⁵, Carla Calligaro⁶, Fabrizio Salvi⁷, David Paterson⁸ & Paolo Zamboni⁹

¹Institute for Maternal and Child Health, IRCCS Burlo Garofolo, Trieste, Italy, ²Elettra-Sincrotrone Trieste, Area Science Park, Basovizza, Trieste, Italy, ³Department of Pathology and Forensic Medicine, University of Trieste, Trieste, Italy, ⁴Department of Morphology, Surgery and Experimental Medicine and LTTA Centre, University of Ferrara, Ferrara, Italy, ⁵European Synchrotron Radiation Facility, Grenoble Cedex 9, France, ⁶Servizio Diagnostica Veterinaria, University of Udine, Udine, Italy, ⁷IRCCS Neurological Sciences, Centro il Be.Ne, Ospedale Bellaria, Bologna, Italy, ⁸Australian Synchrotron, Clayton, Victoria, Australia, ⁹Vascular Diseases Center, University of Ferrara, Cona (Ferrara), Italy.

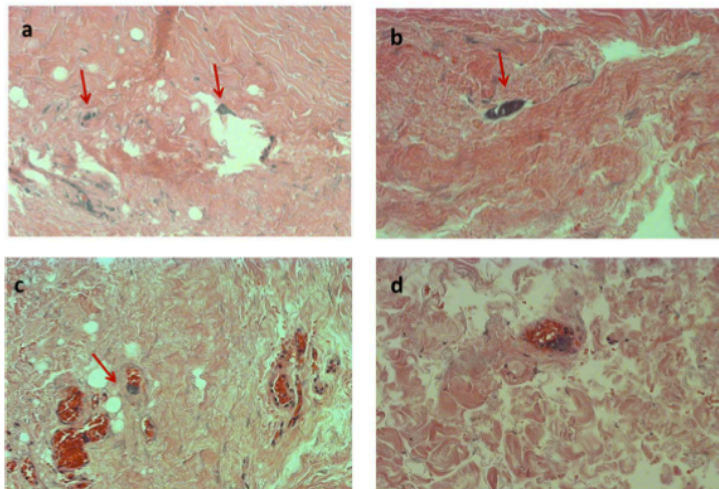


Figure 1 | Optical microscopy images of anomalies in MS jugular vein tissues. Images a and b show suggested micro-calcifications (arrows). A scratch in the tissue is evident in a, while b, c and d show the singular appearance of same microvessel. The arrow in c indicates the presence of basophilic-calcified material inside a capillary. The same is revealed in panel d. All images are at 40 × magnification.

Started at TwinMic
Then extended to 2 other synchrotron facilities
to get complementary information:

- ESRF (ID21)
- Australian Synchrotron (XFM)

Rapid XRF imaging at XFM beamline (Australian Synchrotron)

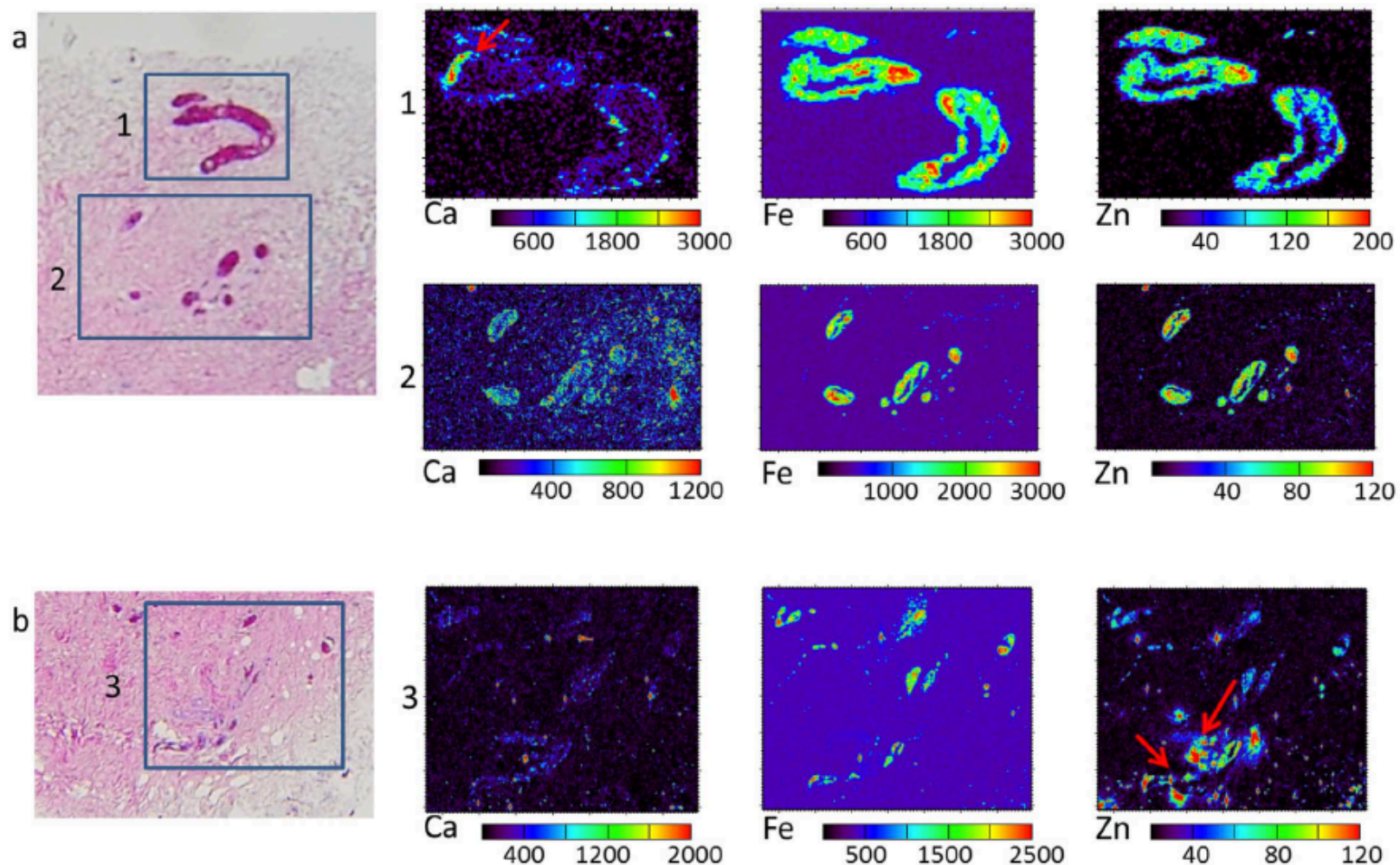


Figure 2 | XRF elemental maps at 12.74 keV in MS2 tissue jugular sections. Three consecutive tissue sections of MS2 sample are used: two unstained for XRF analyses and one HH stained for tissue structure recognition. a) and b): light microscopy images, the boxes indicate the selected regions for XRF analyses in the unstained sections. The corresponding elemental maps of Ca, Fe and Zn of regions 1, 2 and 3 acquired at the XFM beamline at 12.74 keV with 2 μm spatial resolution on the corresponding unstained tissue slices are shown in rows 1, 2 and 3 respectively. Red arrow in Ca map (1) indicates a calcification further analyzed at 4.12 keV. Arrows in Zn map indicate potential contaminants and tissue debris. The concentrations reported on the scale bars are in ppm. Region 1: 250 μm \times 170 μm ; Region 2: 600 μm \times 400 μm ; Region 3: 700 μm \times 600 μm .

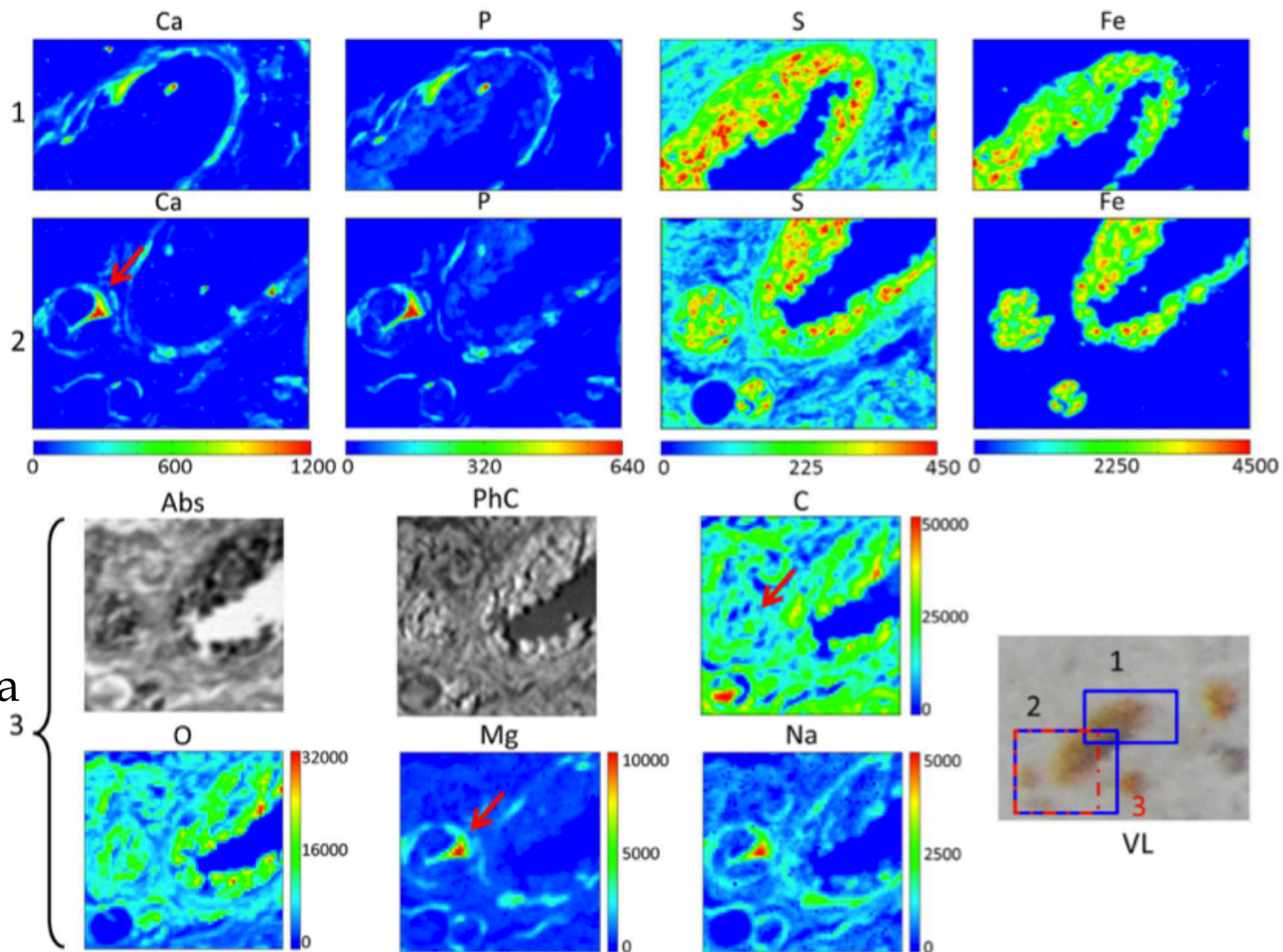
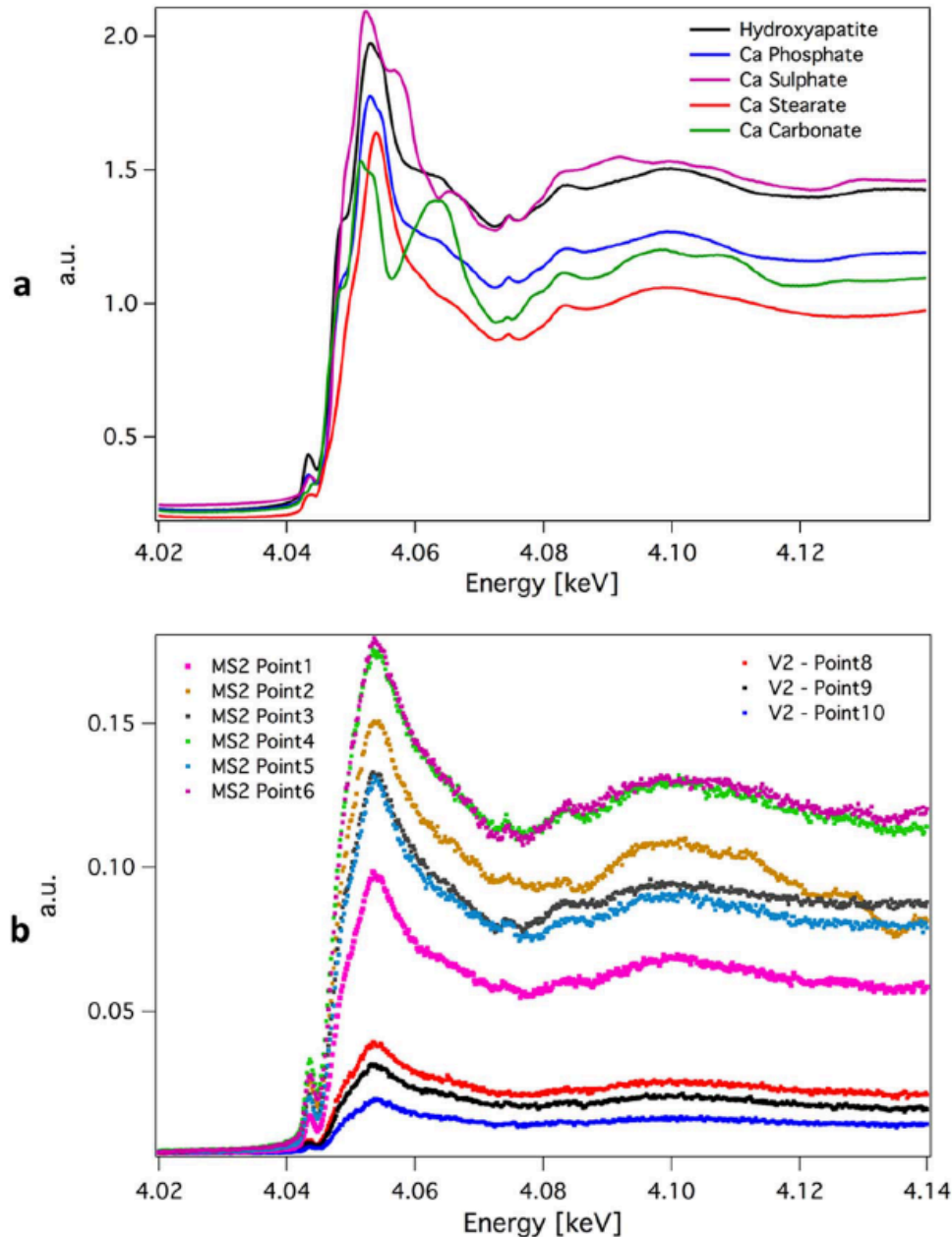


Figure 3 | XRF analyses of microvessels in a MS2 jugular tissue section. Row 1: elemental maps of Ca, P, S and Fe acquired on regions 1 (100 $\mu\text{m} \times 54.5 \mu\text{m}$) at 7.2 keV (ID21 beamline) with 0.5 μm spatial resolution and 300 ms/pixel acquisition time; Row 2: elemental maps of Ca, P, S and Fe acquired on region 2 (100 $\mu\text{m} \times 76 \mu\text{m}$) at 7.2 keV (ID21 beamline) with 0.5 μm spatial resolution and 300 ms/pixel acquisition time; Row 3: Absorption (Abs) and phase contrast images (PhC) with the corresponding elemental maps of C, O, Mg and Na collected on region 3 (80 $\mu\text{m} \times 80 \mu\text{m}$) at 1.5 keV (Twinmic beamline) with 0.5 μm spatial resolution and 10 s/pixel acquisition time. The analysed regions are indicated in the corresponding visible light image (VL) of the MS2 tissue section. The red arrow indicates a region analysed at 4.12 keV too.



In control tissues, the major contributions in the XANES spectra seem to come from organic Ca salts.

On the contrary, in the diseased subject tissues the XANES results are in line with a substantial presence of hydroxyapatite (and other inorganic calcium salts) in clear connection with the vasa venorum.



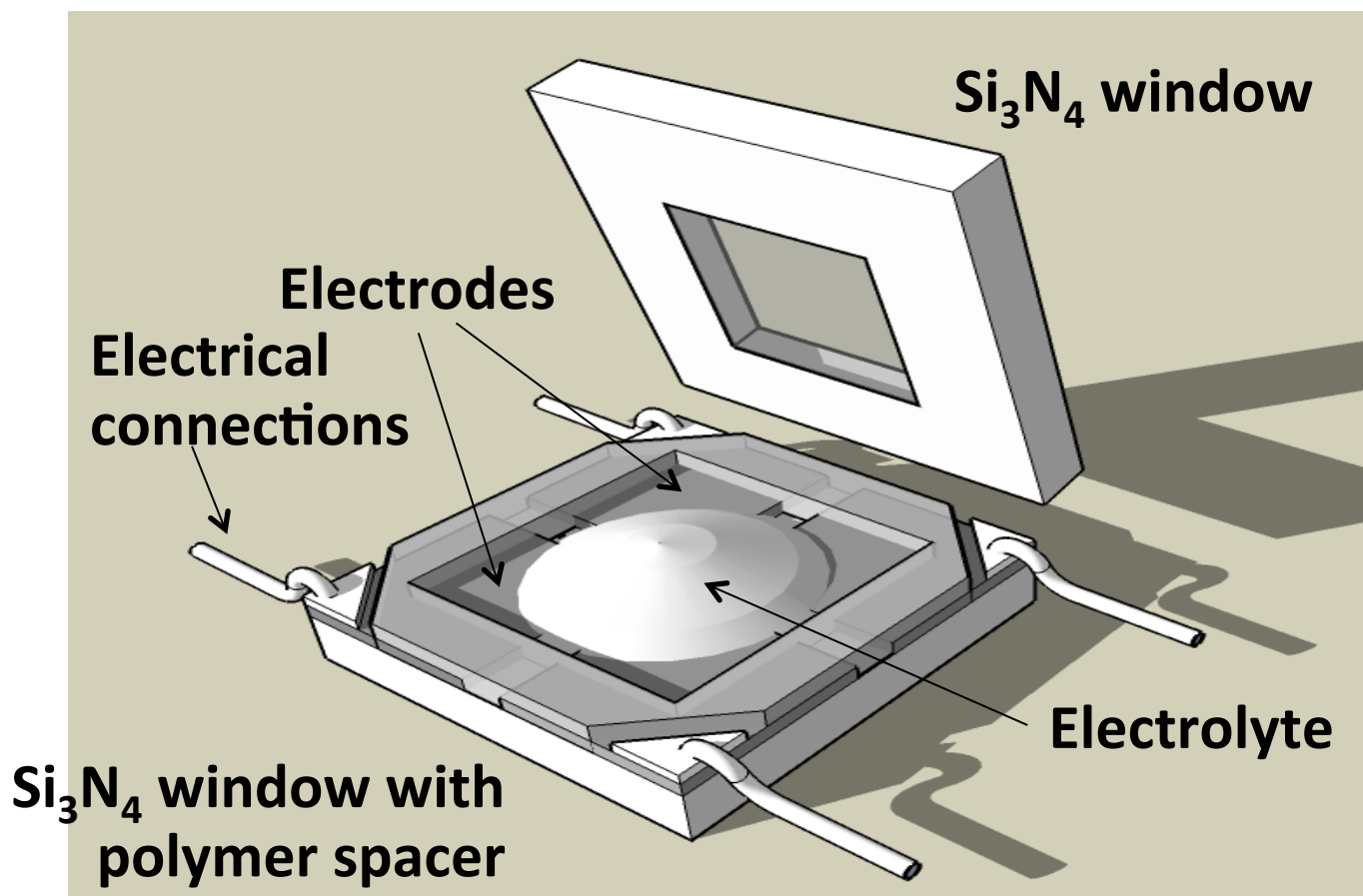
Electrochemistry: Development of fuel cells



*Benedetto Bozzini,
Uni Lecce/ Salento, I*

Towards the
development
of a micro fuel-cell for
in-situ
spectromicroscopy

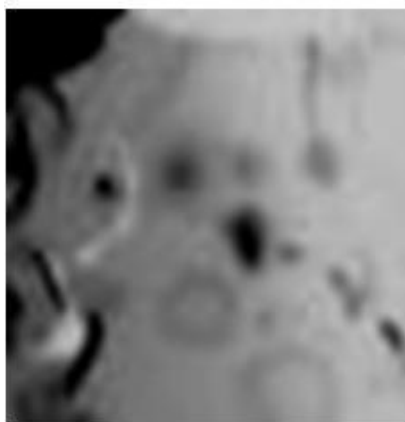
**Vacuum-compatible functional electrolytic specimen
cell for in-situ studies**



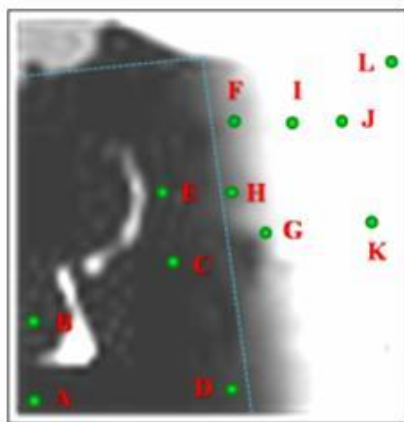


Electrochemistry: Development of fuel cells

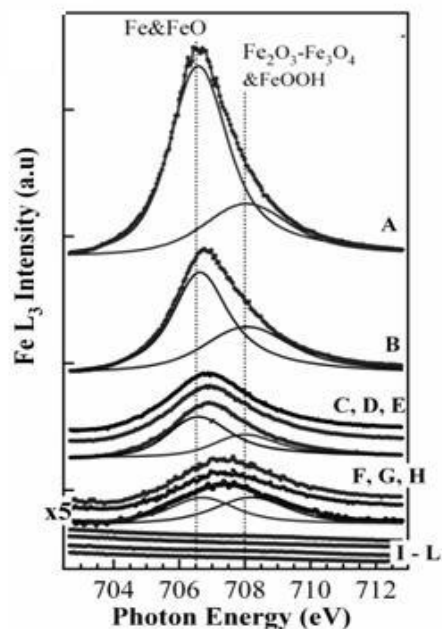
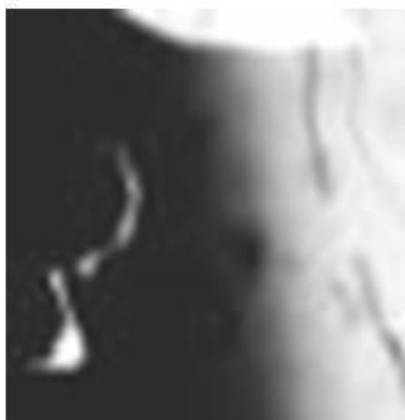
701eV



706.3eV / 701eV



706.3eV



Spatial variations in the Fe concentration confirmed by the μ -XAS Fe L_3 spectra, measured in selected spots
Highly sensitive to the Fe chemical state

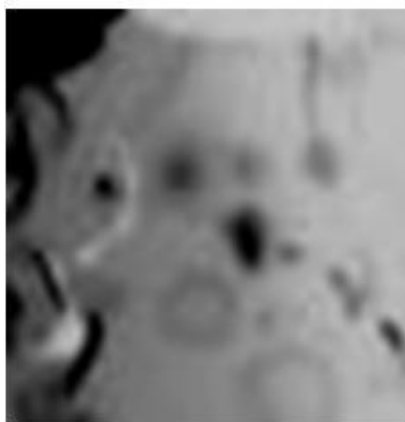
Fe signal attenuation approaching the edge of the Fe electrode, that reflects the increasing loss of Fe due to the corrosion process

The relative amount of the Fe species in the higher oxidation states and FeOOH is increasing in the heavily corroded areas and for areas closer to the edge

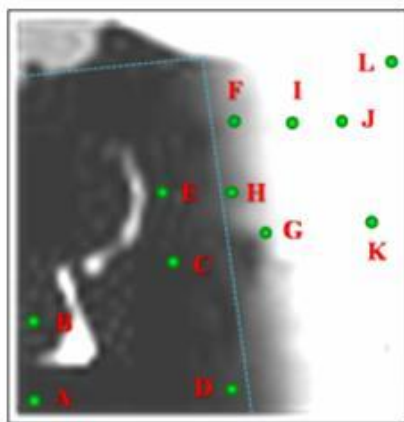


Electrochemistry: Development of fuel cells

701eV



706.3eV / 701eV



The contrast in the 701.0 eV map taken below the Fe L₃ edge is dominated by the morphology (thickness variations)

Above the absorption edge (706.3 eV) dramatic intensity drop occurs in the Fe electrode region and in locations containing Fe species

706.3eV



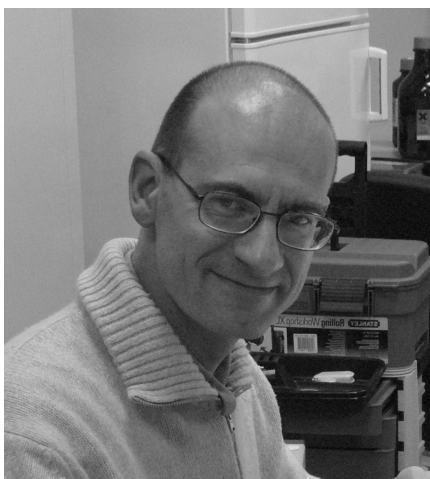
Sulfonated based fluoropolymer-copolymer. Synthetic polymers with ionic properties. Considerable attention as a proton conductor for PEMFC for its excellent thermal and mechanical stability.

Division map: Fe concentration distribution map. Two very bright 'cracks' inside the Fe electrode and several 'bubble-like' brighter areas, resulting from localised corrosion.

The released Fe contributes to the gradually fainting darkness moving away from the electrode edge: diffusion of Fe species released from the electrode as a result of the electrochemical reactions

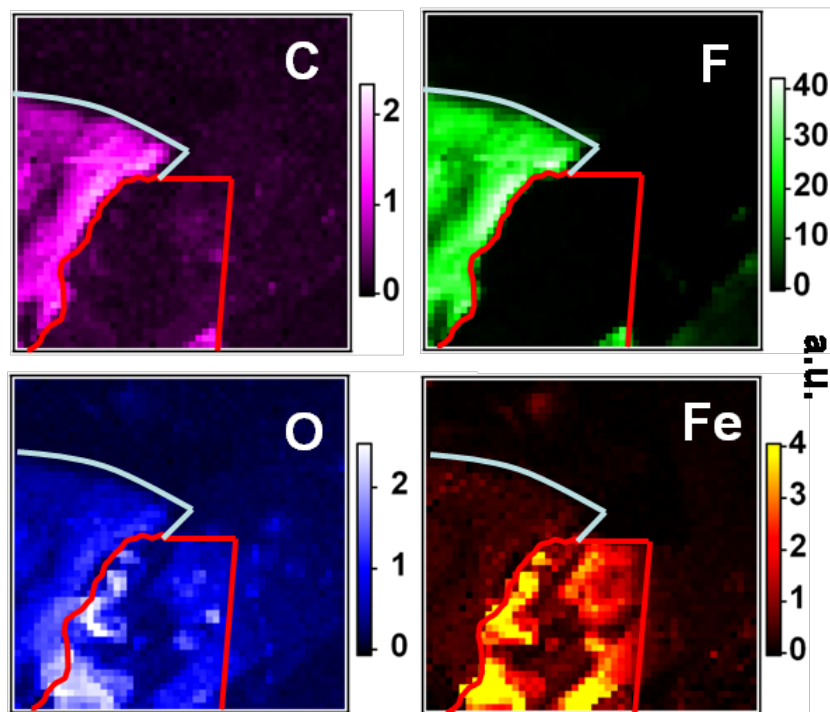
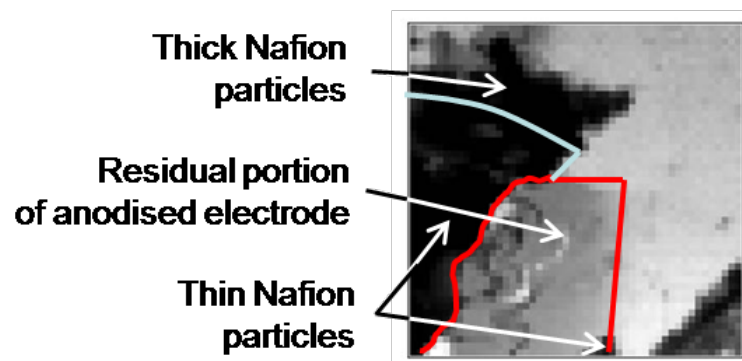


Electrochemistry: Development of fuel cells



*Benedetto Bozzini,
Lucia D'Urzo
Uni Lecce, I*

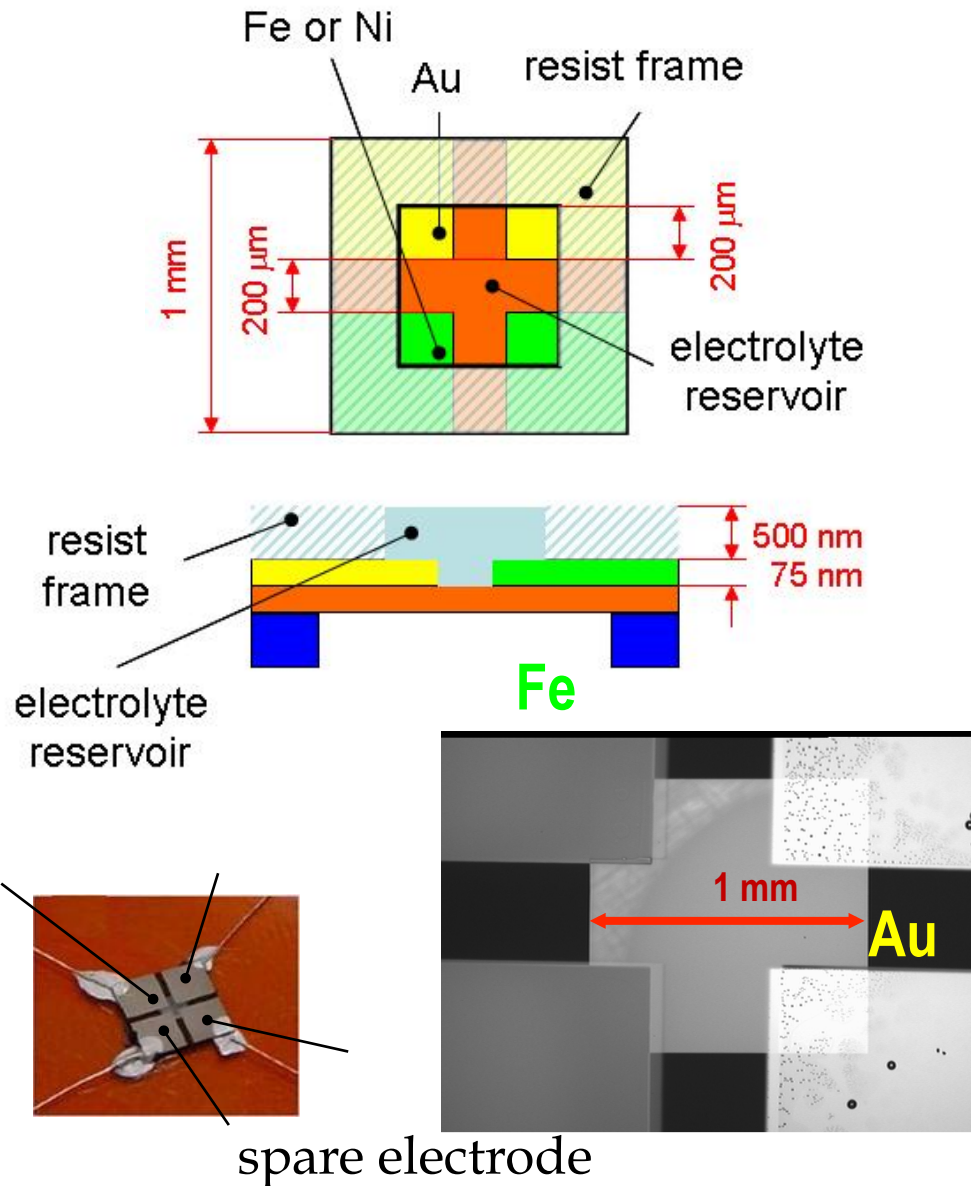
Understanding the electrocorrosion in fuel cells that is the main life-time limiting factor



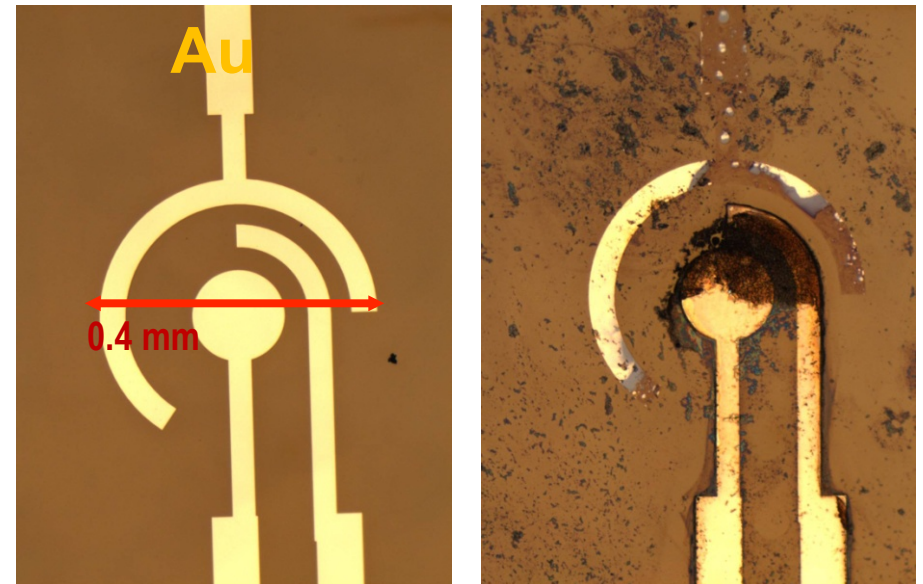
Three different spectroscopies: AAEI, XANES, LEXRF

80 x 80 μm^2 ,
50ms dwell/px,
5s dwell/ px

Through-mask evaporation



Electron-beam lithography



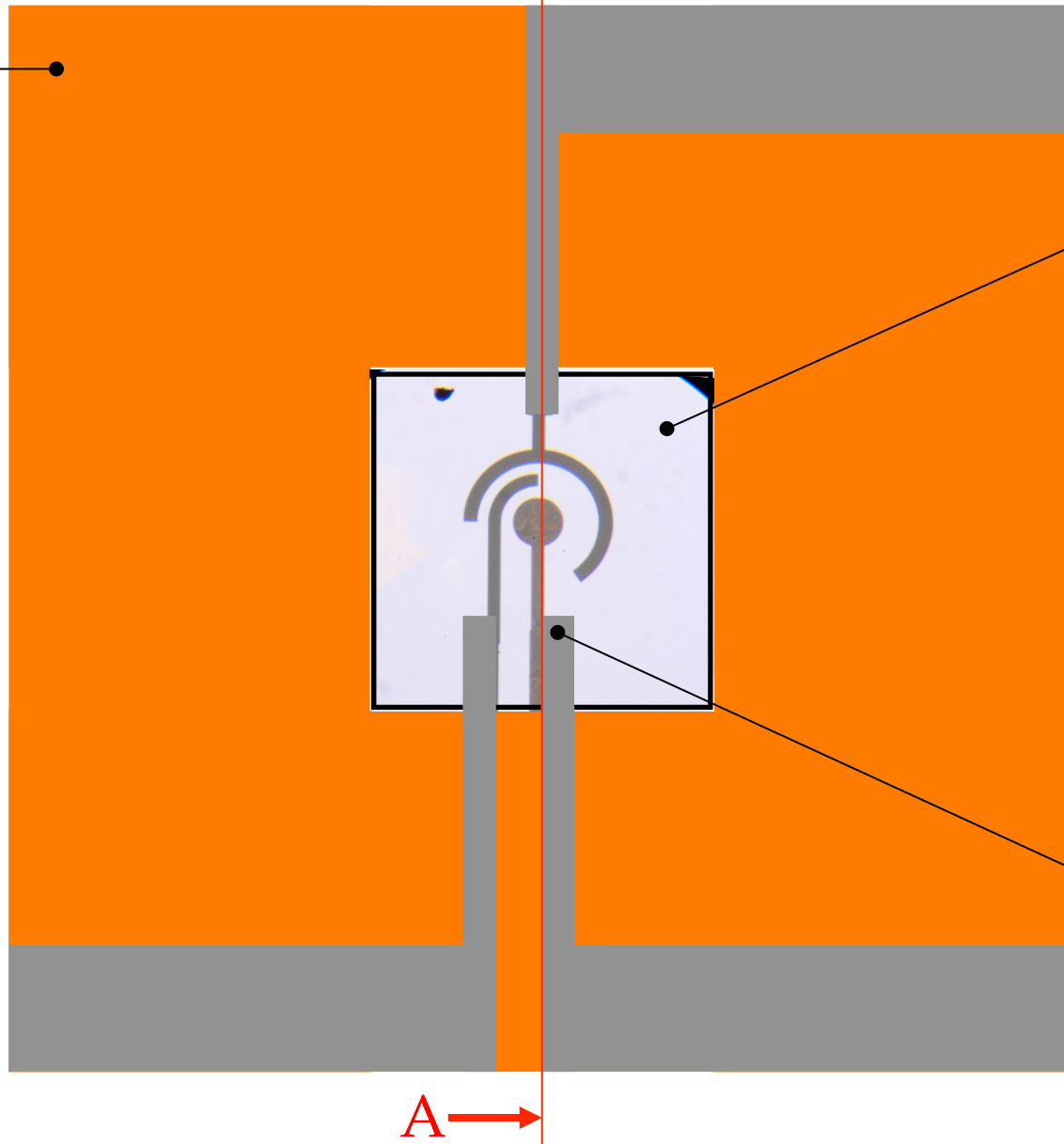
- 1) Improve the current density distribution
- 2) Localisation of the electrochemical processes



Elettra
Sincrotrone
Trieste

STXM: cell design and fabrication

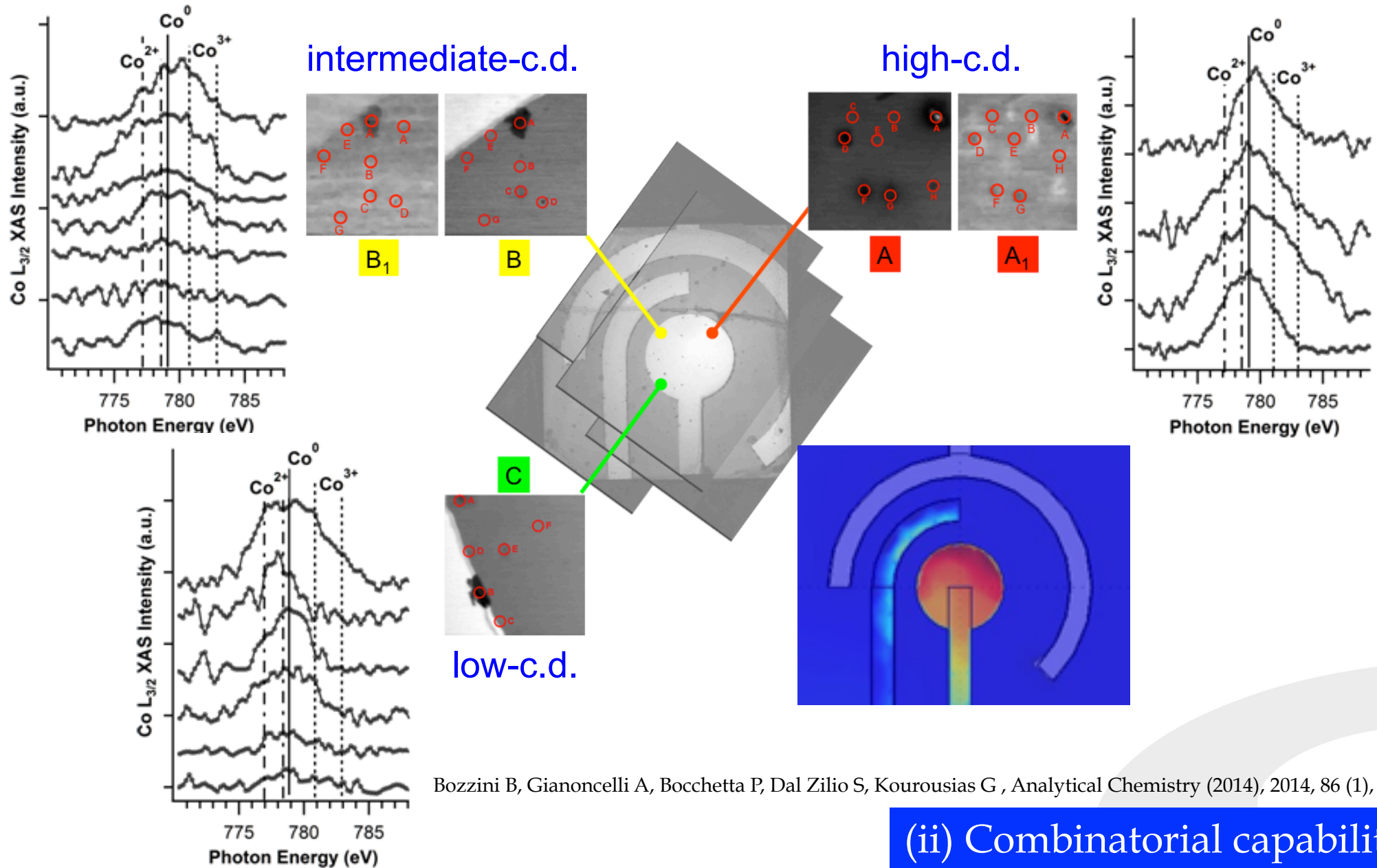
Si frame with
 Si_3N_4 film



Si_3N_4 film
(optical window)

electrode
system

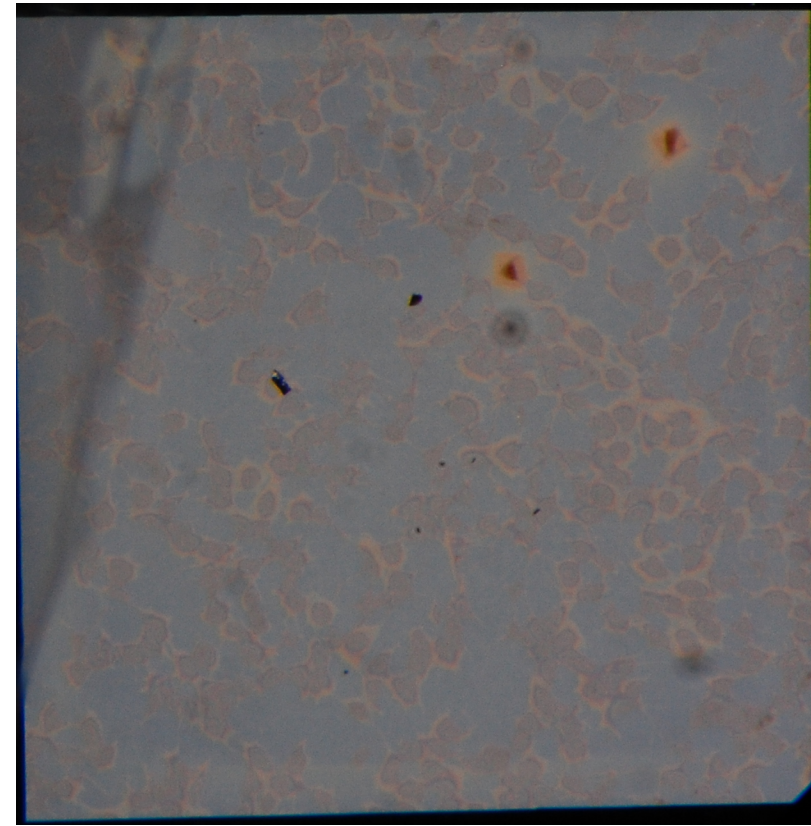
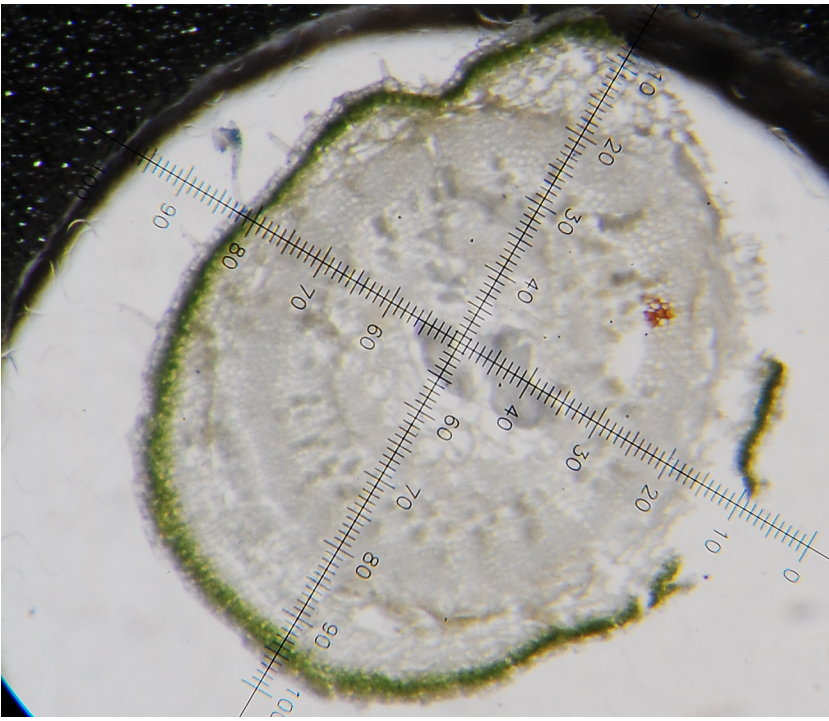
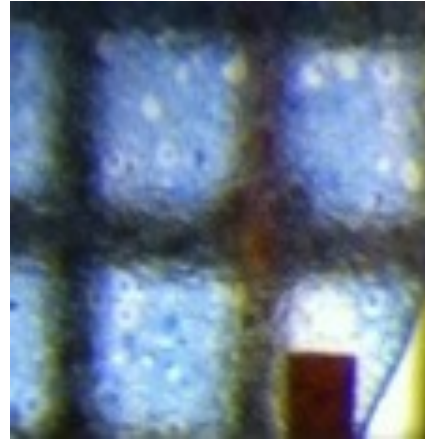
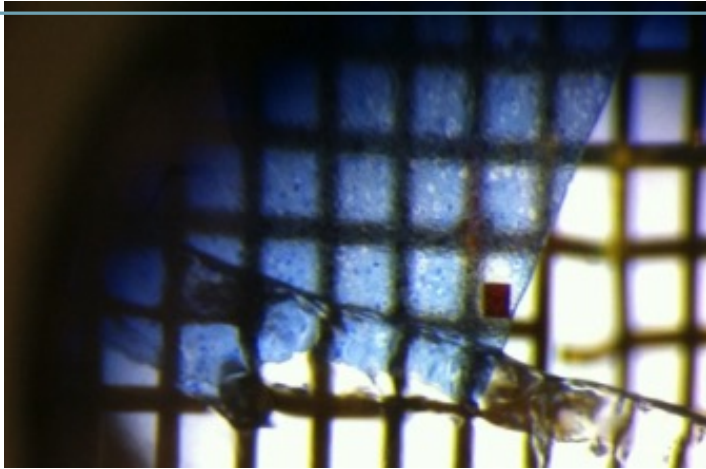
Definition of Co chemical state and distribution: micro-XAS





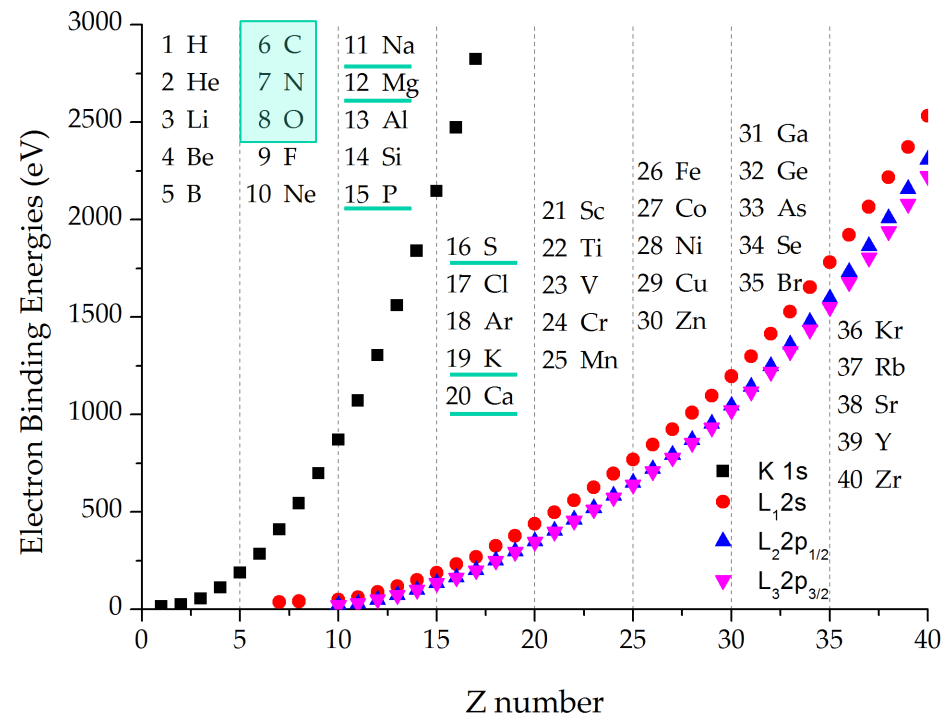
Elettra
Sincrotrone
Trieste

Radiation damage



X-ray radiation damage induced by soft X-rays

- Radiation damage induced by X-rays on biological samples is one of the remaining bottlenecks for their ultrastructural characterization by X-ray microscopy techniques
- X-ray nanofocusing is a today reality but the extent to which the lateral resolution can be pushed without unacceptable bio-sample degradation is still an open question
- The problem is even more pronounced in the soft X-ray regime

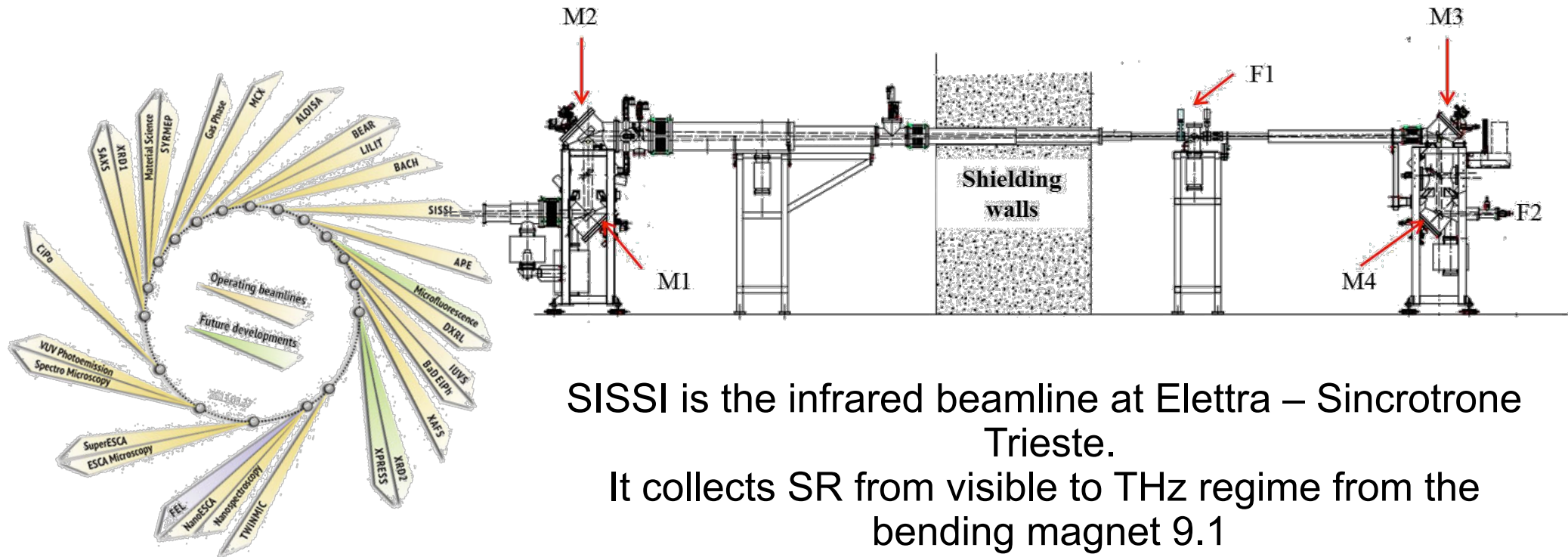




Elettra
Sincrotrone
Trieste

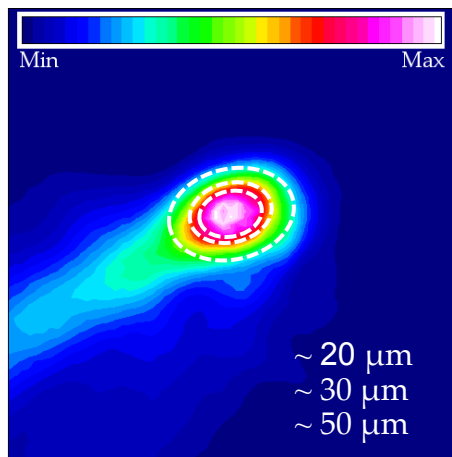
SISSI beamline

Synchrotron Infrared Source For Spectroscopy and Imaging



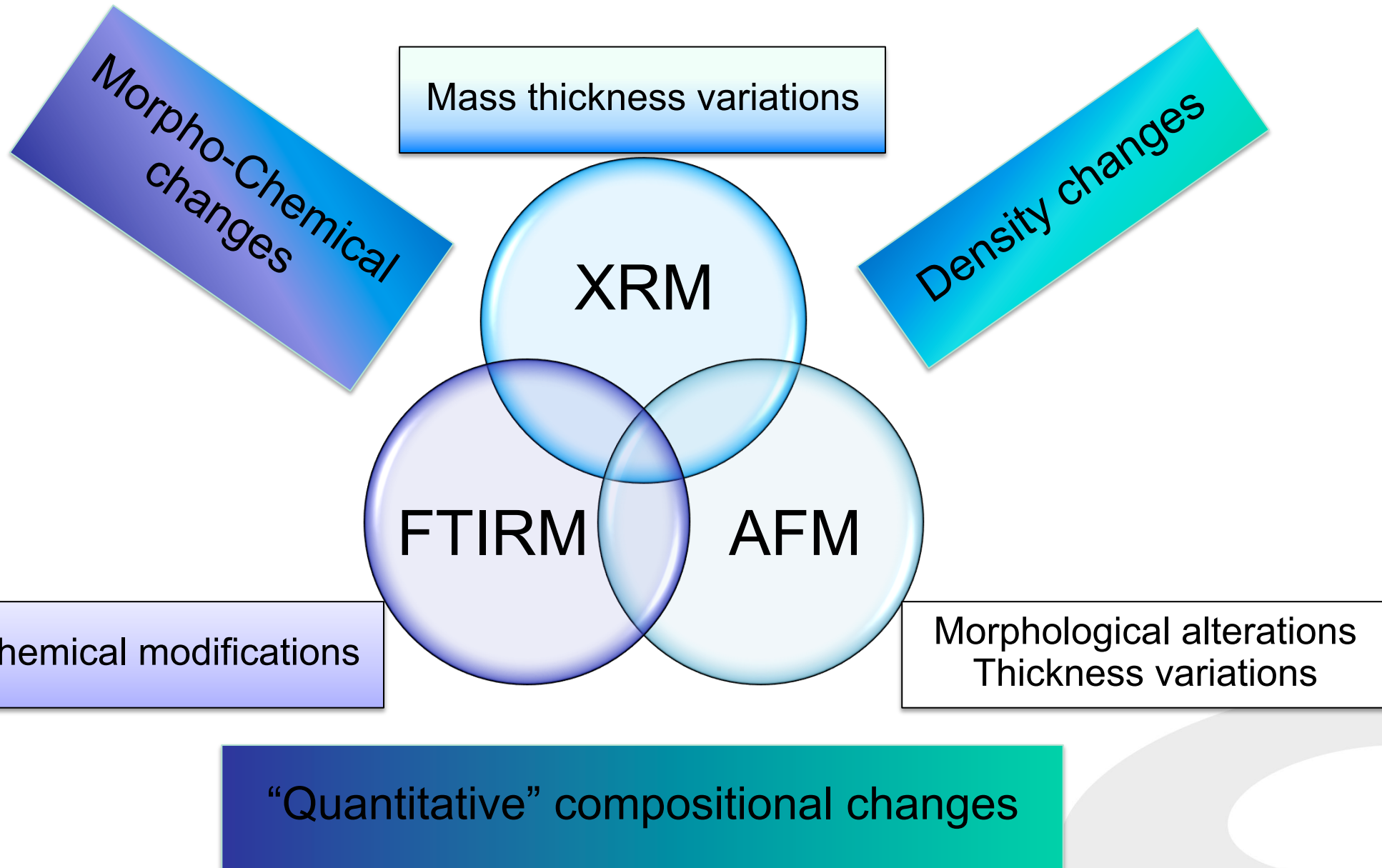
SISSI is the infrared beamline at Elettra – Sincrotrone Trieste.

It collects SR from visible to THz regime from the bending magnet 9.1



Broad-band nature and brightness advantage are exploited for spectroscopy, microscopy and imaging studies in a wide range of research fields, including surface and material science, high-pressure, life sciences, cell biology, cultural heritage and many others.

The methodological approach

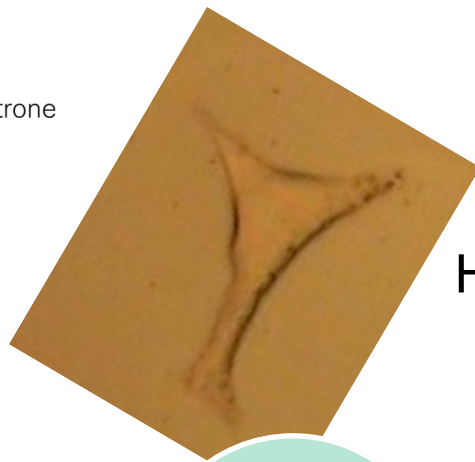




Elettra
Sincrotrone
Trieste

Experimental Design

Hek293T cells (human embryonic kidney)



Step
0

Cell growth on 100 nm Si_3N_4 membranes
Cell fixation with PFA 3.7% and overnight air drying

Step
1

Cell drying in vacuum @ TwinMic
($p < 10^{-5}$ mbar) for 1:30 hour

Step
2

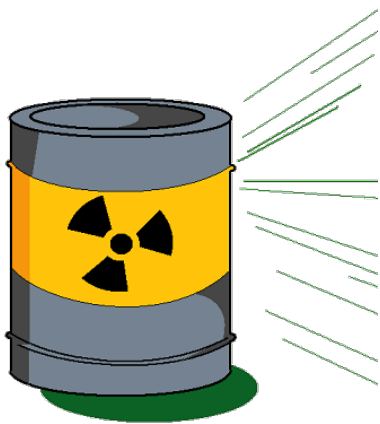
Low Dose STXM mapping @ TwinMic 1 keV
Estimated dose: $2 \cdot 10^6$ Gy

Step
3

High Dose STXM mapping @ TwinMic 1 keV
Estimated dose: $2 \cdot 10^7$ Gy
Cumulative estimated dose: $2.2 \cdot 10^7$ Gy

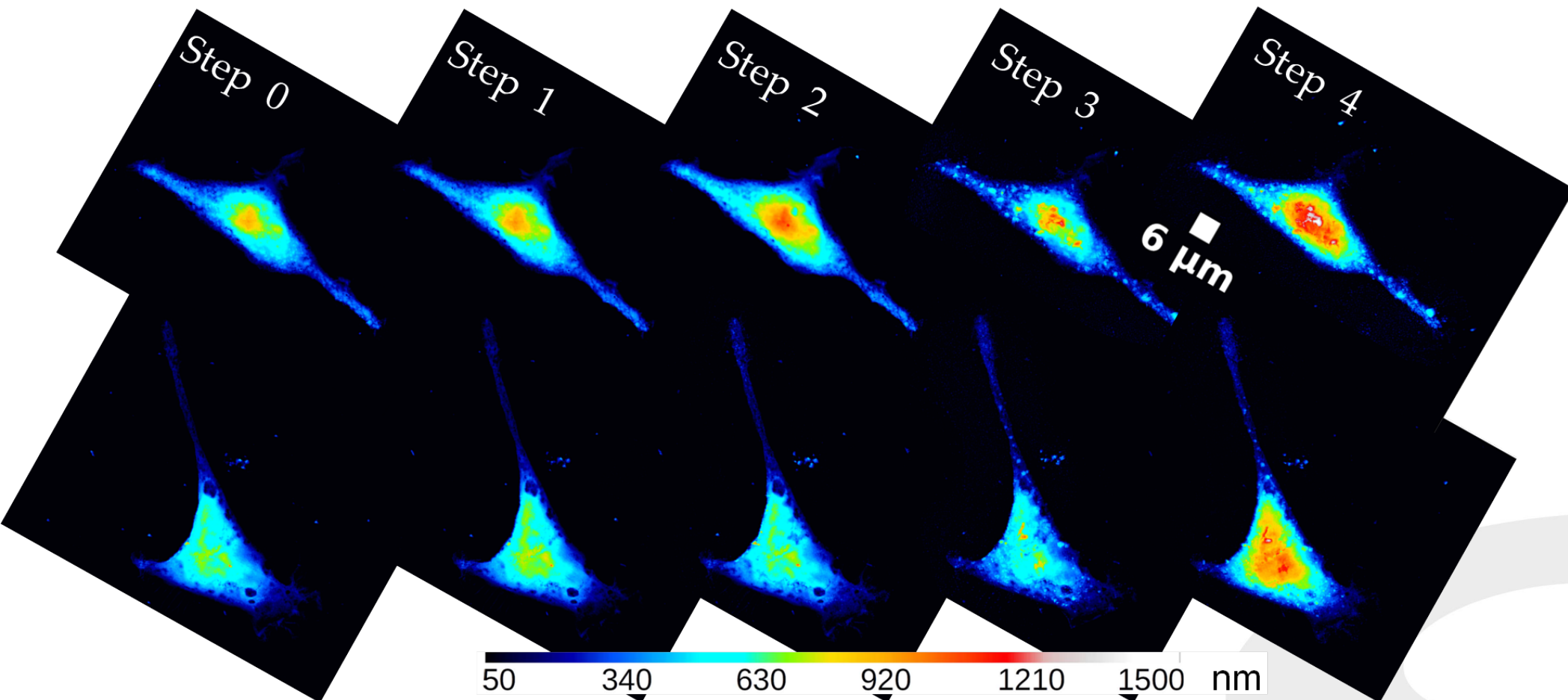
Step
4

Very high dose STXM mapping @ TwinMic 1 keV
Estimated dose: $6 \cdot 10^8$ Gy
Cumulative estimated dose: $6.2 \cdot 10^8$ Gy



Outcomes of AFM

- Minimal cell shrinkage
- Evident degradation/thinning of pseudopodia terminations
- Appreciable thickness variations, especially on the nuclear region at Step 4
- Outstanding topographical changes: nanometric pits and bulges increase in number and size when increasing dose



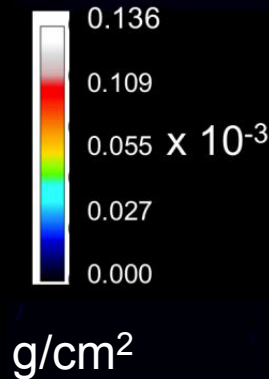
Outcomes of XRM

Mass Thickness $\rho t = -\ln \frac{(I/I_0)}{\mu^*}$

Step 2 ($\sim 10^6$ Gy)

Step 3 ($\sim 10^7$ Gy)

Step 4 ($\sim 10^8$ Gy)



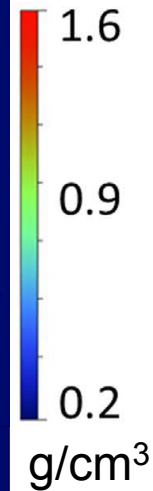
Mass absorption
coefficient

Element fraction	Mass
C	0.5
N	0.16
H	0.07
O	0.25
P+S	0.02

- Mass Thickness decreases with increasing dose

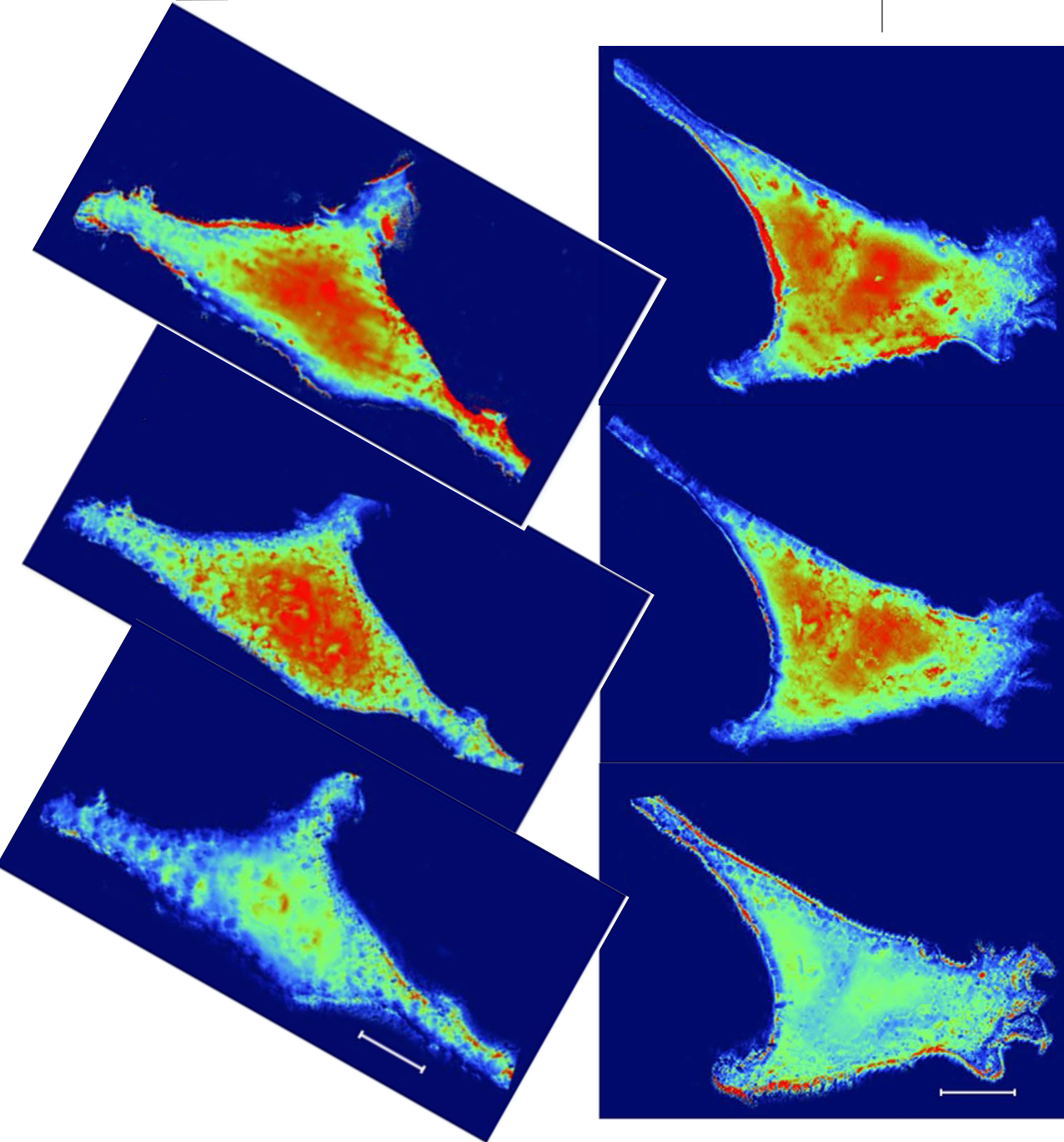
Combining XRM and AFM

**XRM cell images
normalized over
AFM cell thickness**



$$\rho = -\ln \frac{(I/I_0)}{\mu^* t}$$

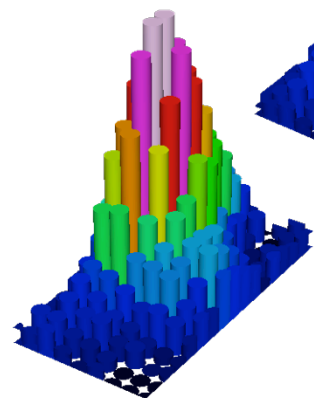
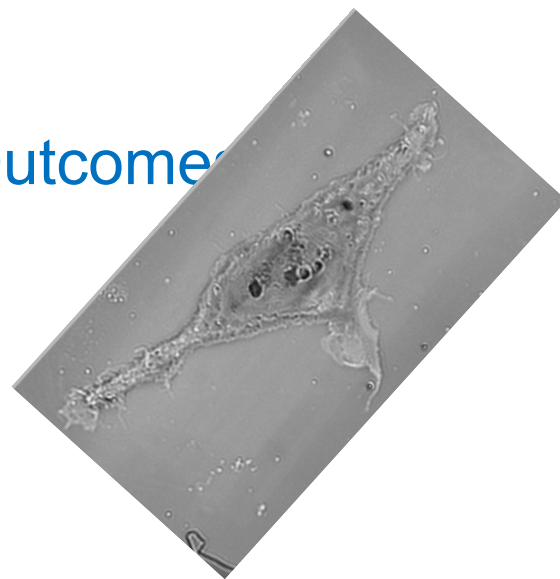
- Progressive reduction of the cell density with increasing X-ray dose



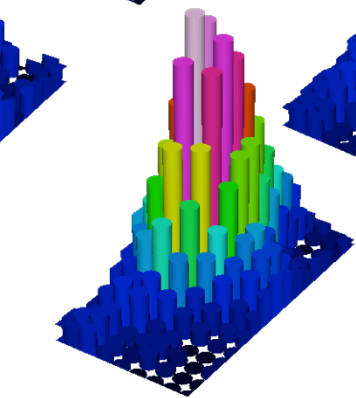


Elettra
Sincrotrone
Trieste

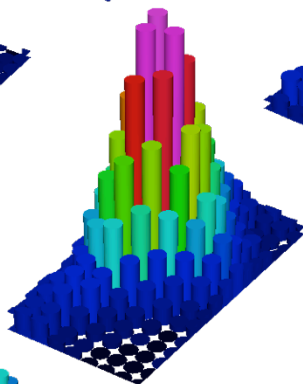
FTIRM Outcome



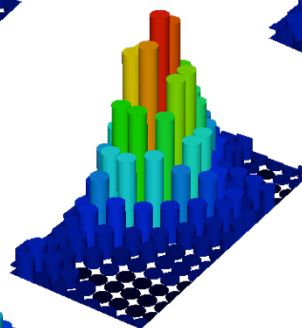
Step 0



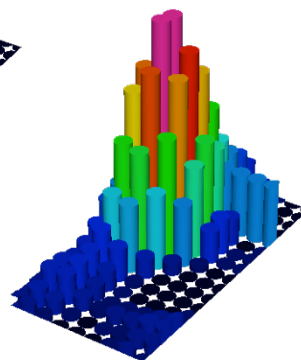
Step 1



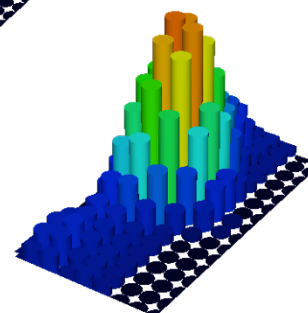
Step 2



Step 3

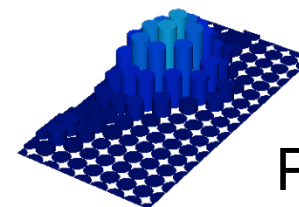


Step 4



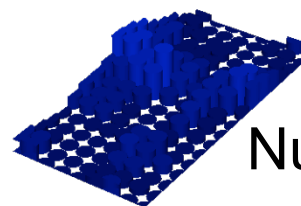
Lipids

2988-2830 cm^{-1}



Proteins

1702-1480 cm^{-1}



Nucleic acids

1270-1190 cm^{-1}

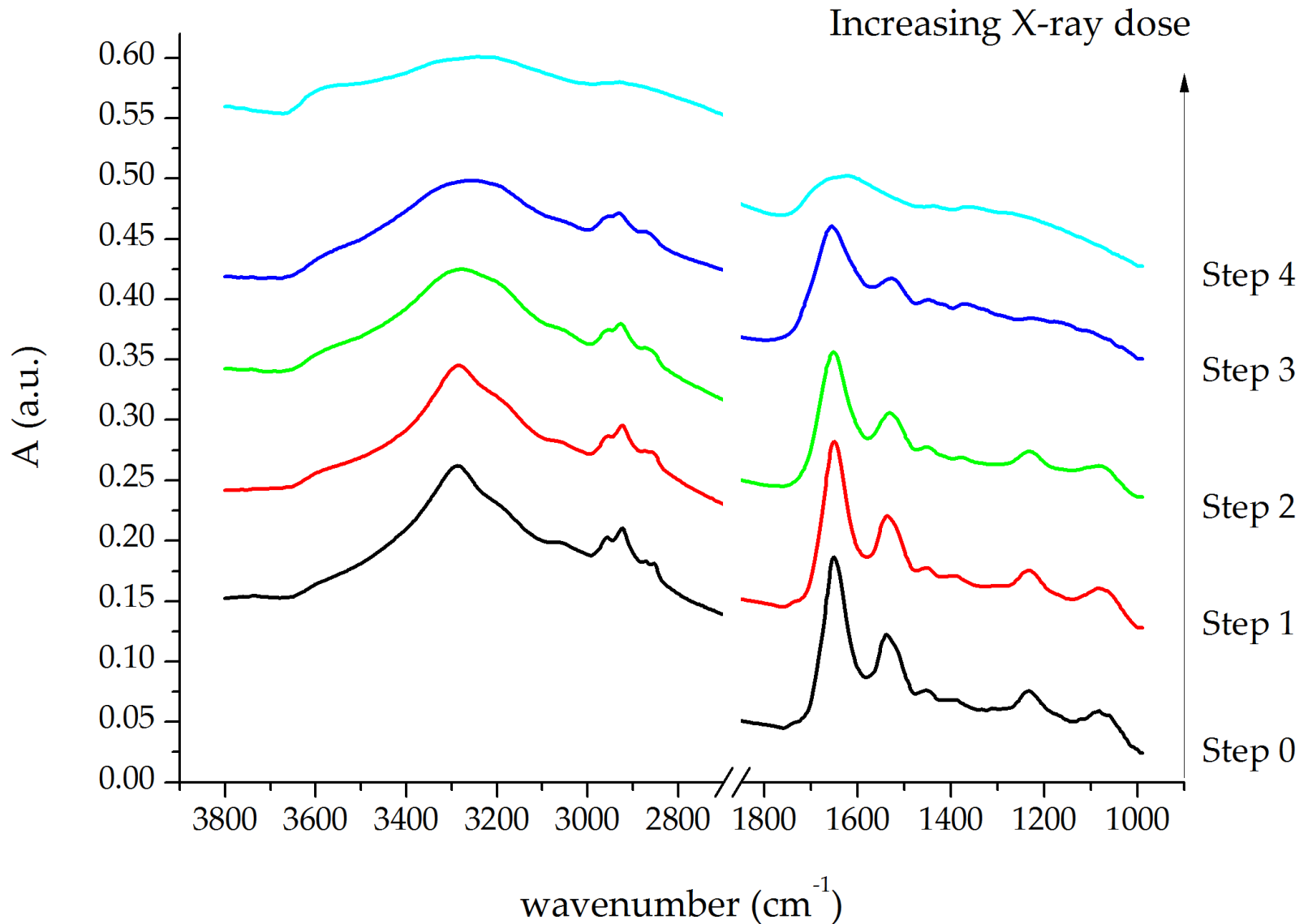
0

1



Min

Max

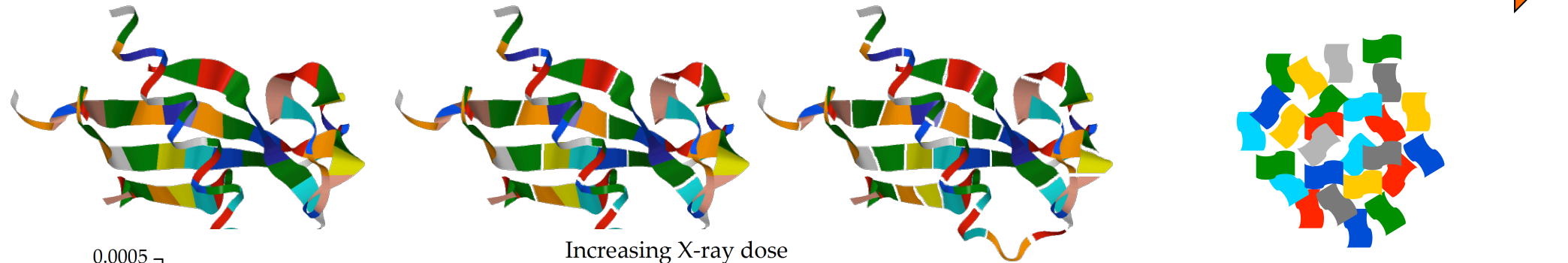


Dehydration

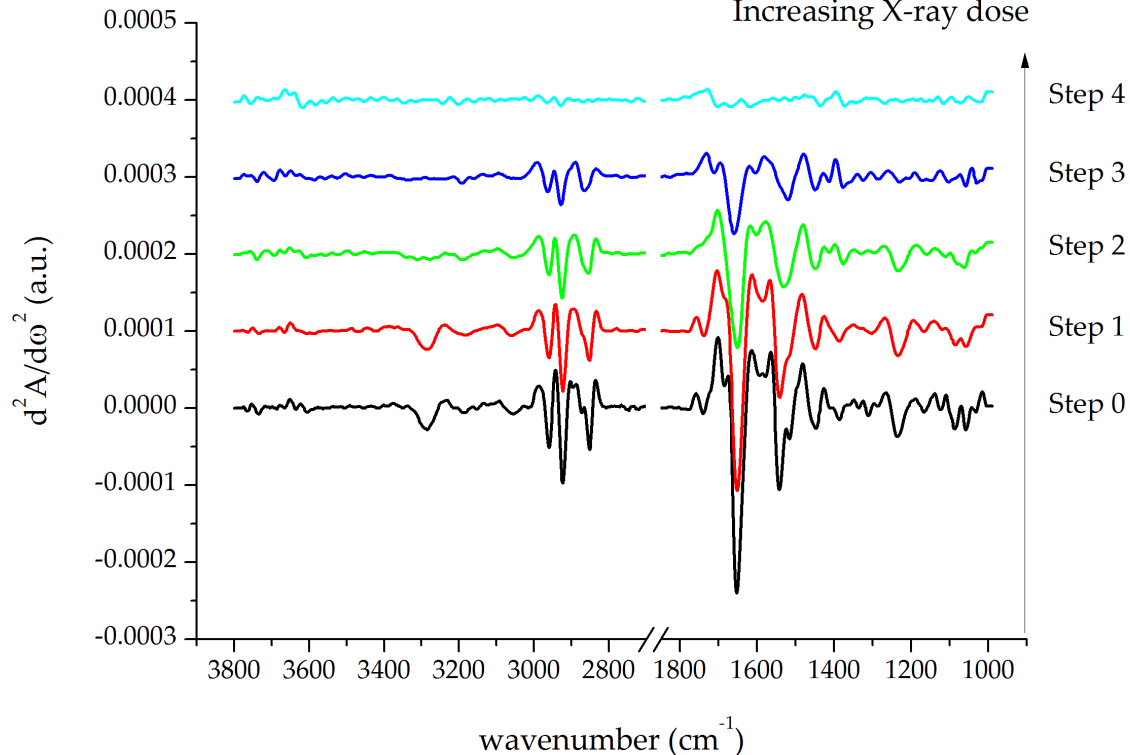
Low-Dose

Medium-Dose

High-Dose



Increasing X-ray dose



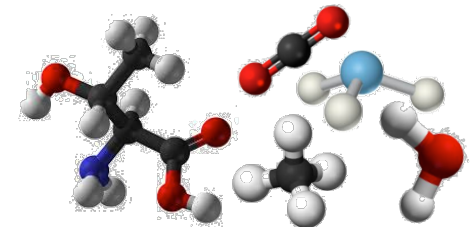
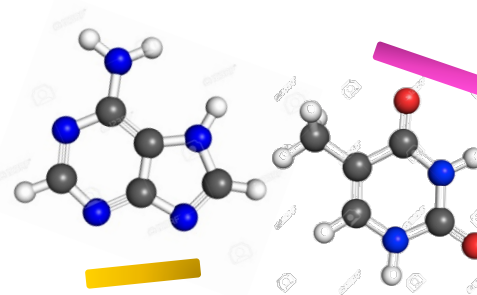
At Step 4 cellular lipids, proteins, carbohydrates and nucleic acids lose their structure and both backbone and lateral chains of these macromolecules undergo an extensive fragmentation

Dehydration

Low-Dose

Medium-Dose

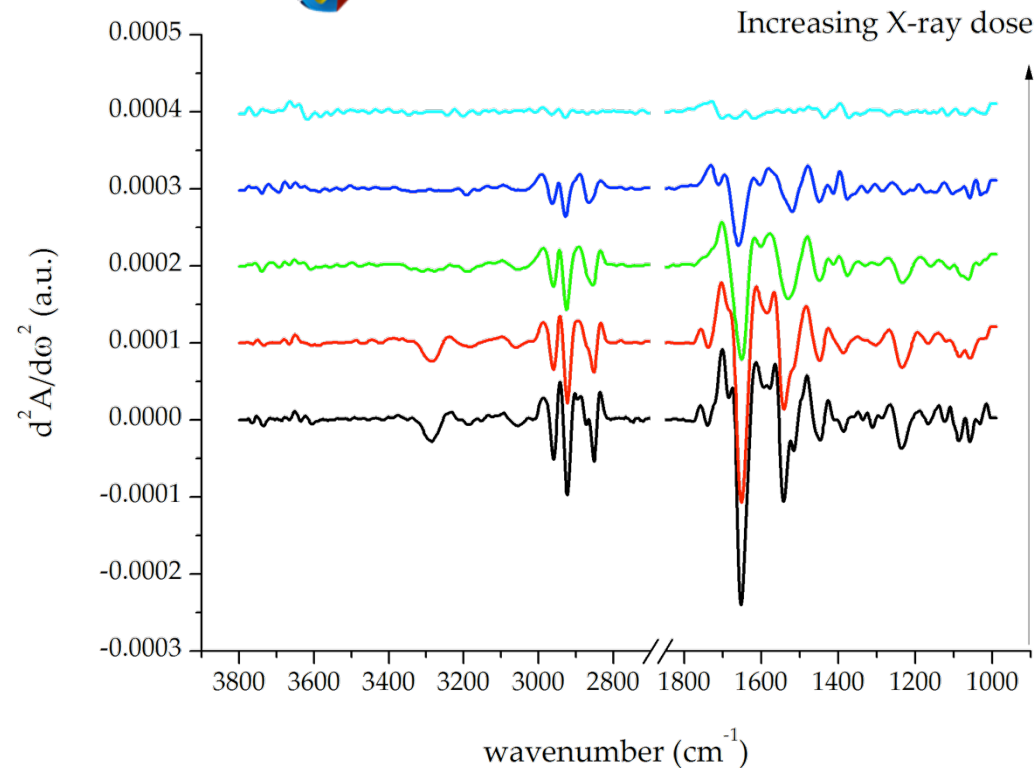
High-Dose



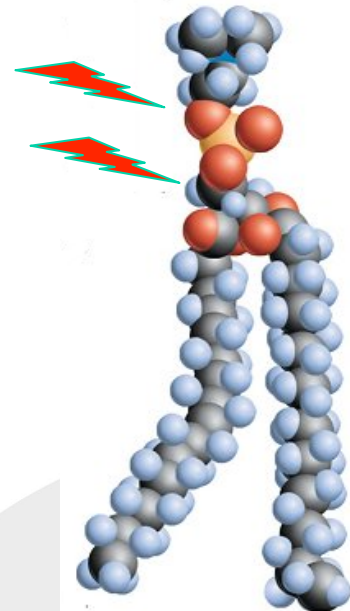
Comprehensive
disintegration
of the vibrational
architecture

Formation of possible
volatile compounds
(lower density)

Decarbonylation and
deamination reaction
products?



Step 4
Step 3
Step 2
Step 1
Step 0



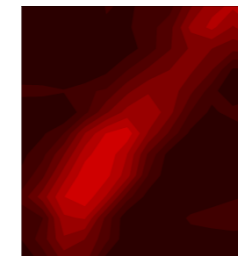
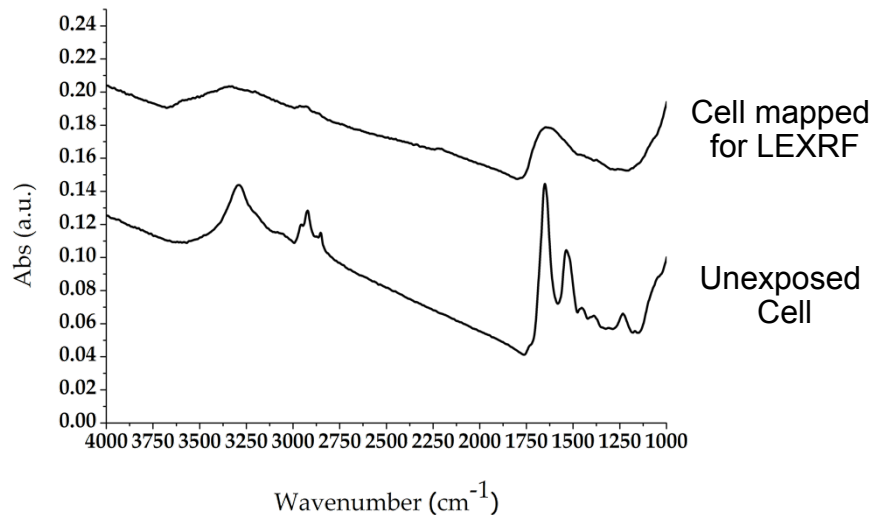
Open questions & Future plans

- Individual cell line susceptibility
- Effects of diverse fixation methods
- Effects of diverse sample architecture: cell, tissues
- Effect of physiological environment

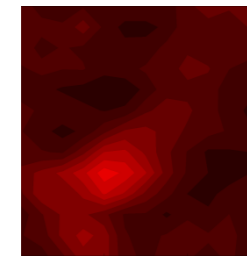
Open questions & Future plans

- Individual cell line susceptibility

Formalin fixed Balb/3T3 mouse fibroblasts



Amide I



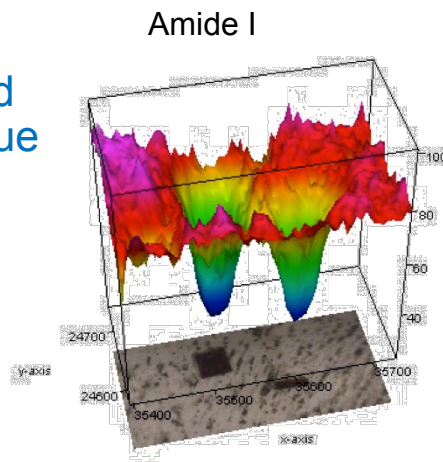
Lipids

Max

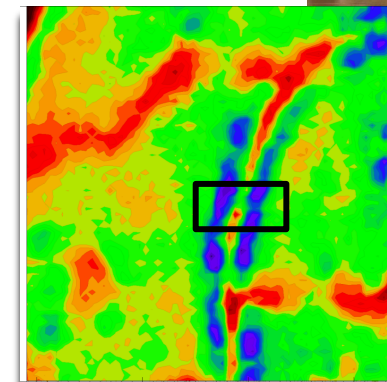
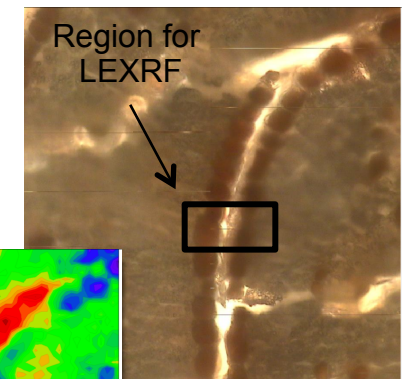
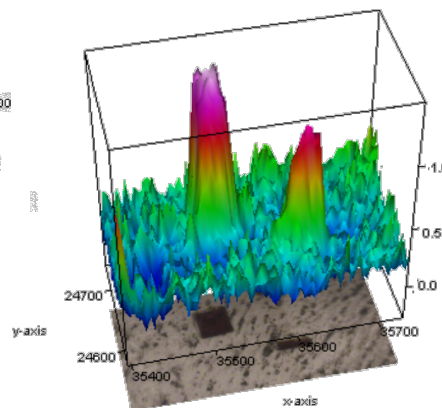
Min (0 a.u.)

- Effects of diverse fixation methods
- Effects of diverse sample architecture

Paraffinized
animal tissue



Protein β aggregates

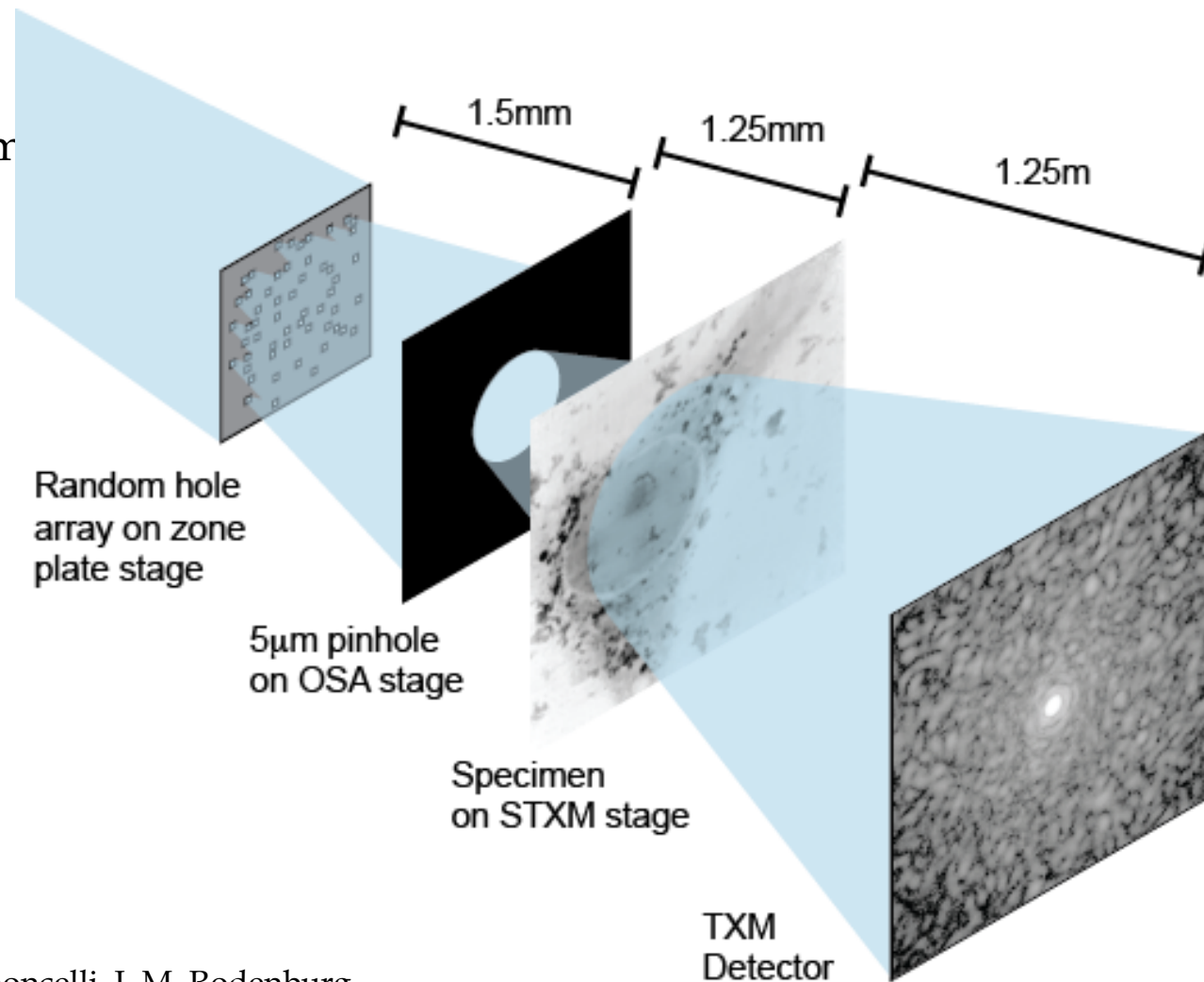


Plant tissue frozen
and lyophilized

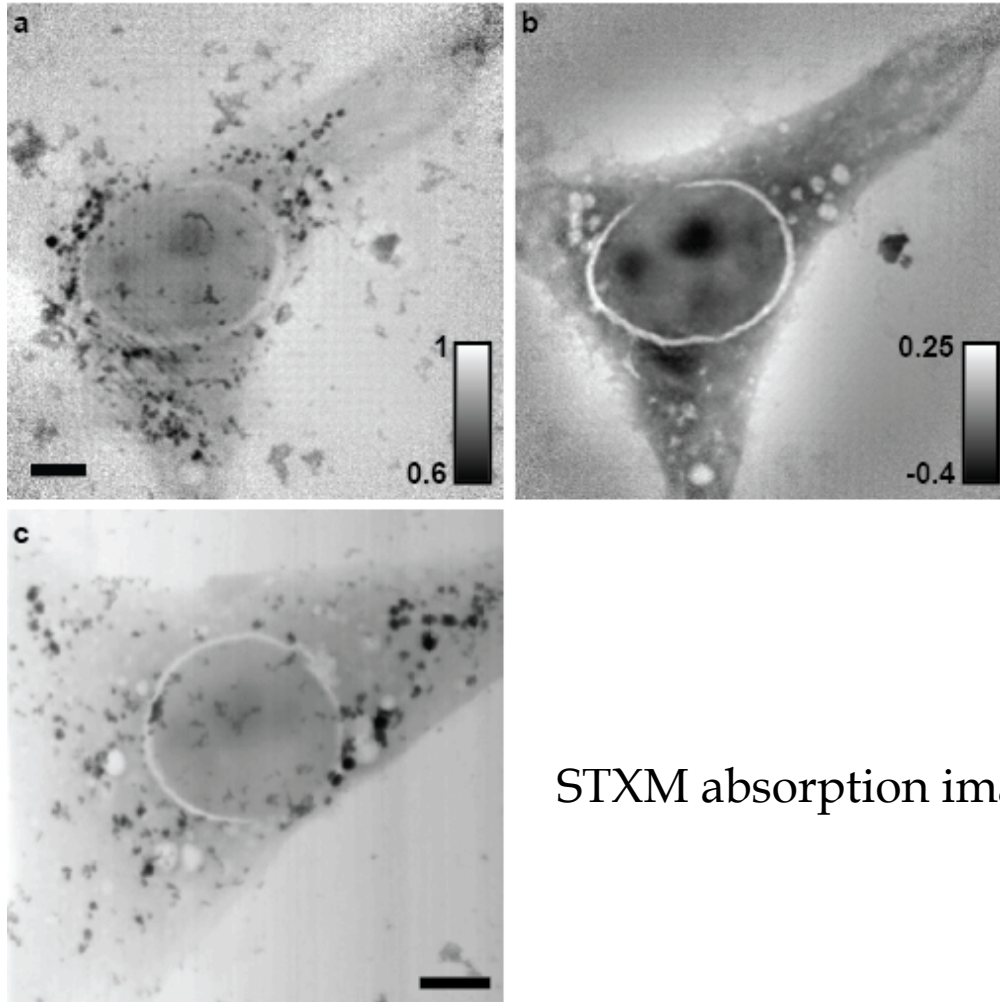
Soft X-ray spectromicroscopy using ptychography with randomly phased illumination

- Illuminated area defined by a 5 μm pinhole
- Sample was scanned with raster steps $\sim 1 \mu\text{m}$

To spread the illumination across the detector



Soft X-ray spectromicroscopy using ptychography with randomly phased illumination

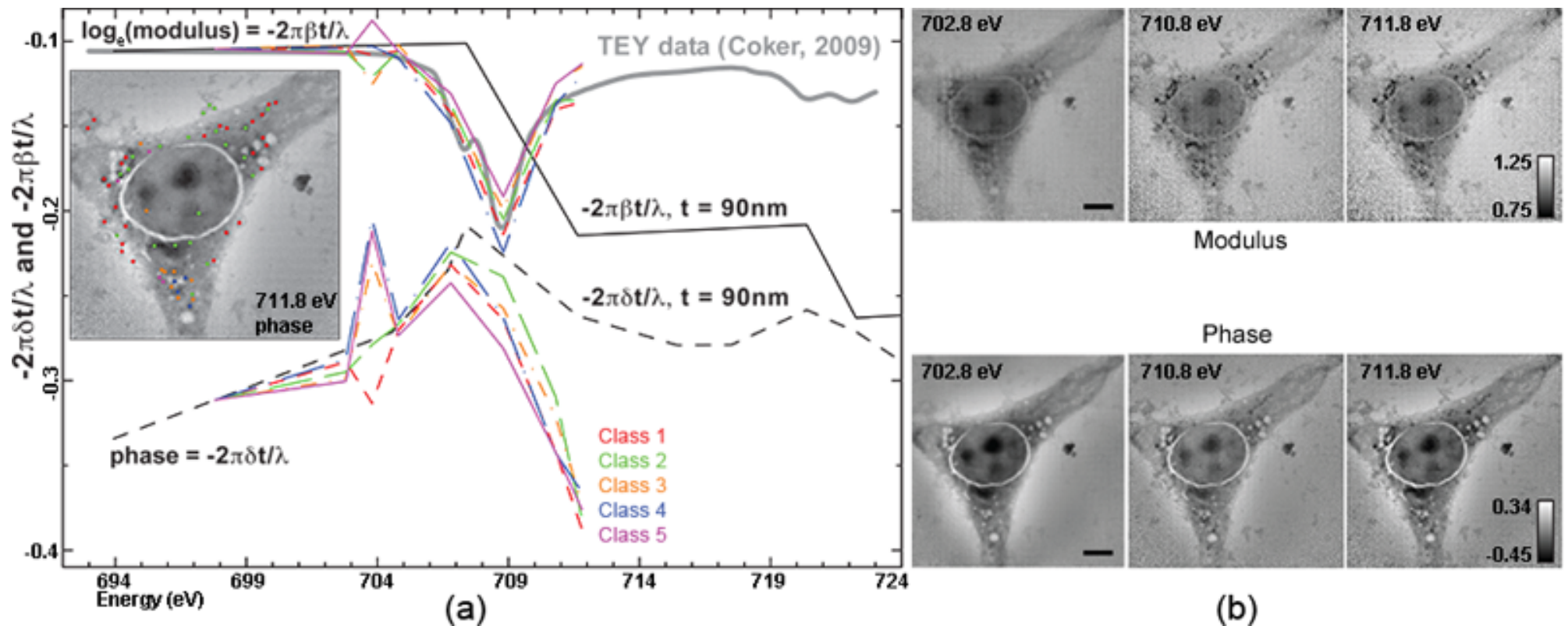


Balb/3T3 mouse fibroblast cells that had been exposed to cobalt ferrite (CoFe_2O_4) nanoparticles

Ptychography reconstruction using the ePIE algorithm (Uni of Sheffield)

STXM absorption image

Soft X-ray spectromicroscopy using ptychography

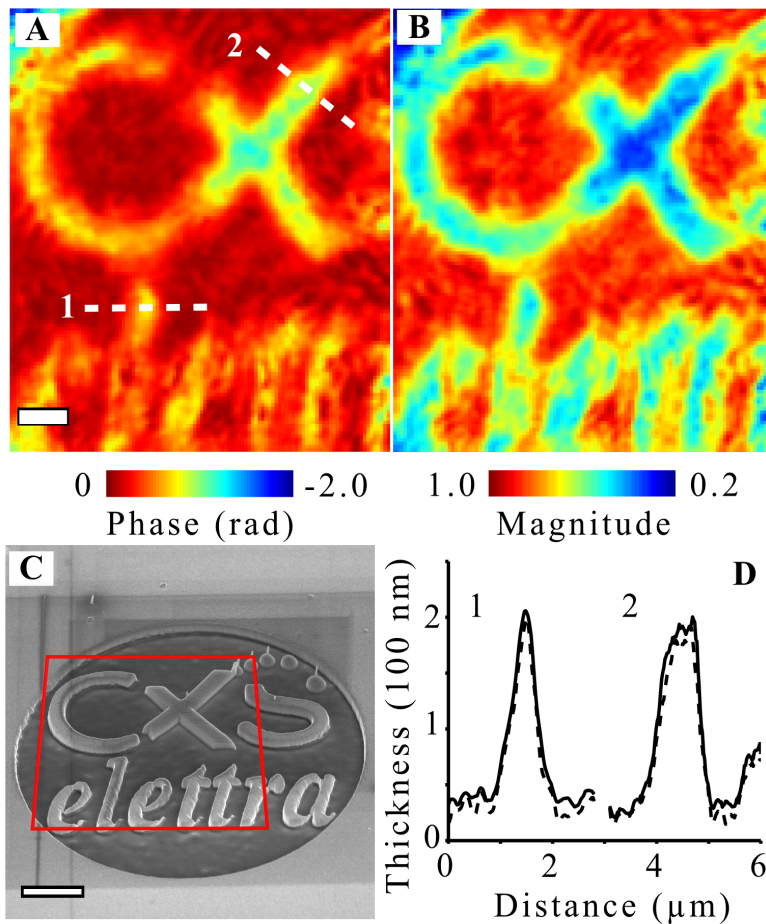


First direct measurements from cobalt ferrite nanoparticles of the phase variations across the iron L₃ edge, with the phase variations showing stronger and clearer features than the modulus data provided

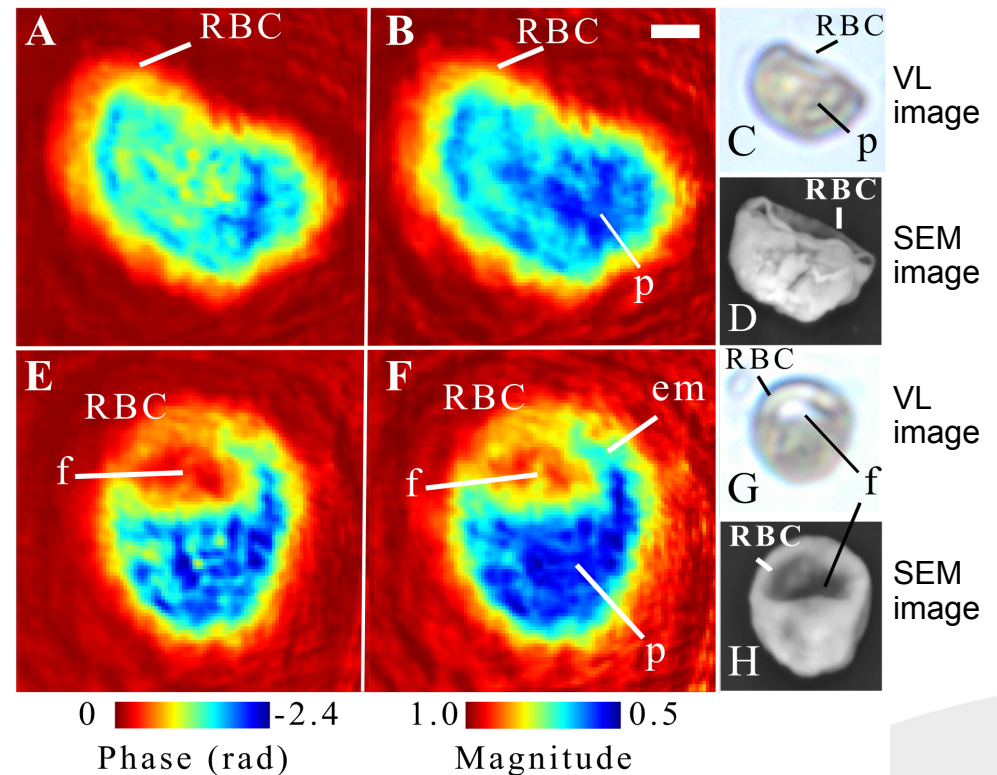
The observed variations in modulus contrast across FeL₃ edge are consistent with estimates based on total electron yield (TEY) data by J. M. Rodenburg and S. J. B. Cooper (University of Oxford, UK)

M.W.M. Jones, B. Abbey, G. Van Riessen, La Trobe University

CXS – ELETTRA test pattern



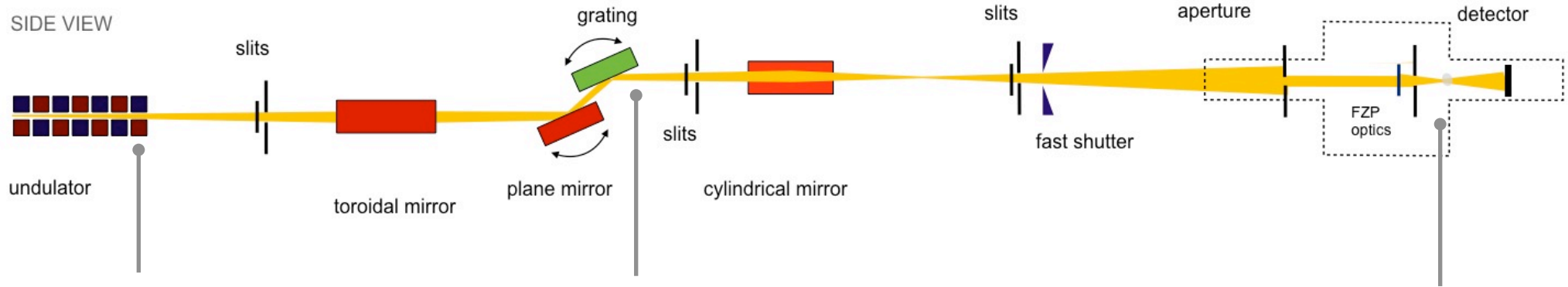
Blood cells infected with the malaria parasite *P. falciparum*





Elettra
Sincrotrone
Trieste

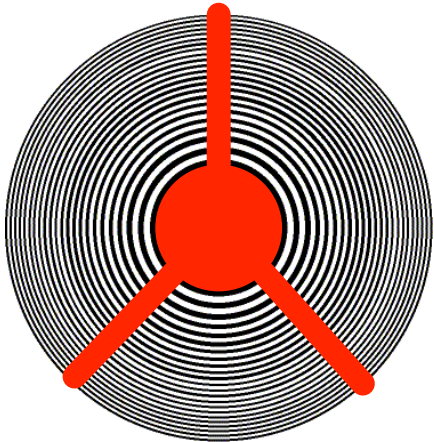
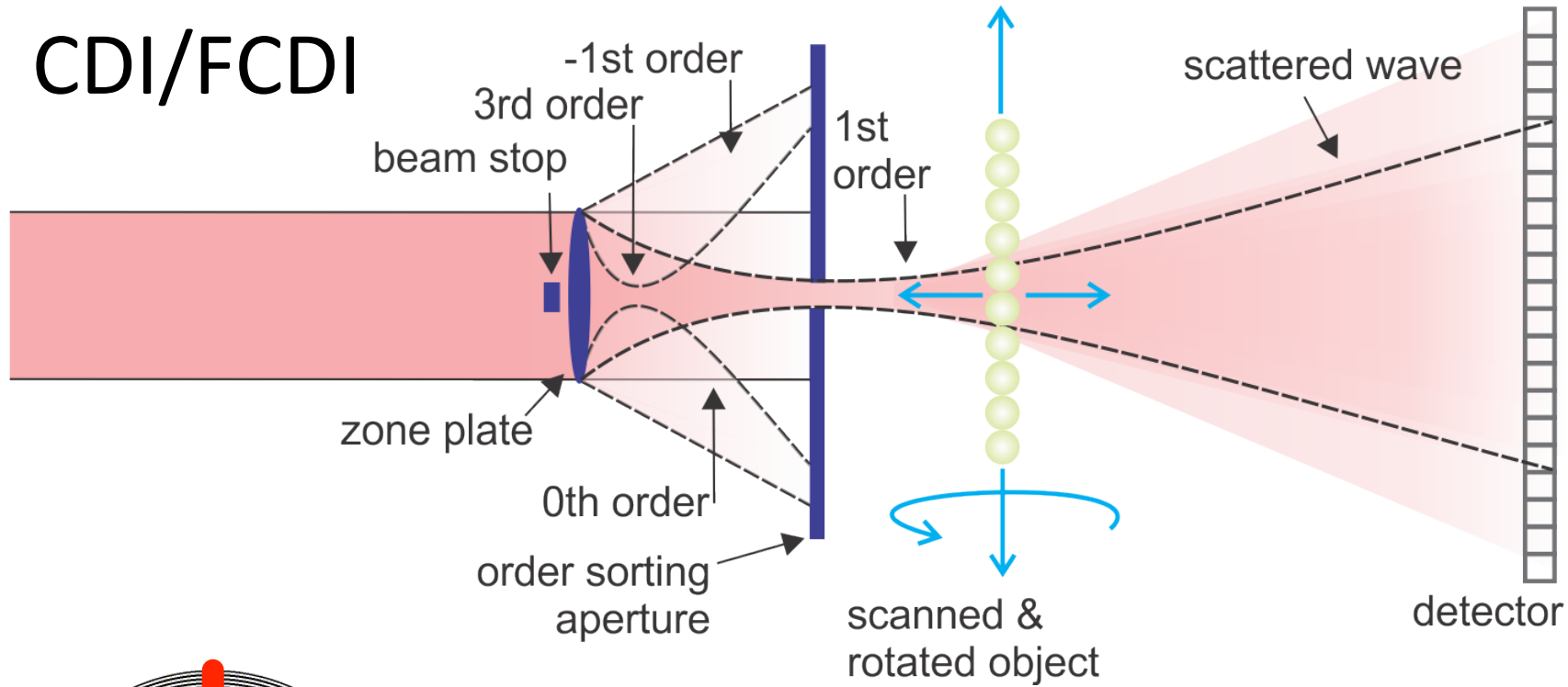
SXRI Beamline



Active position stabilisation: ~17 nm
RMS stability - no thermal drift

fCDI

CDI/FCDI

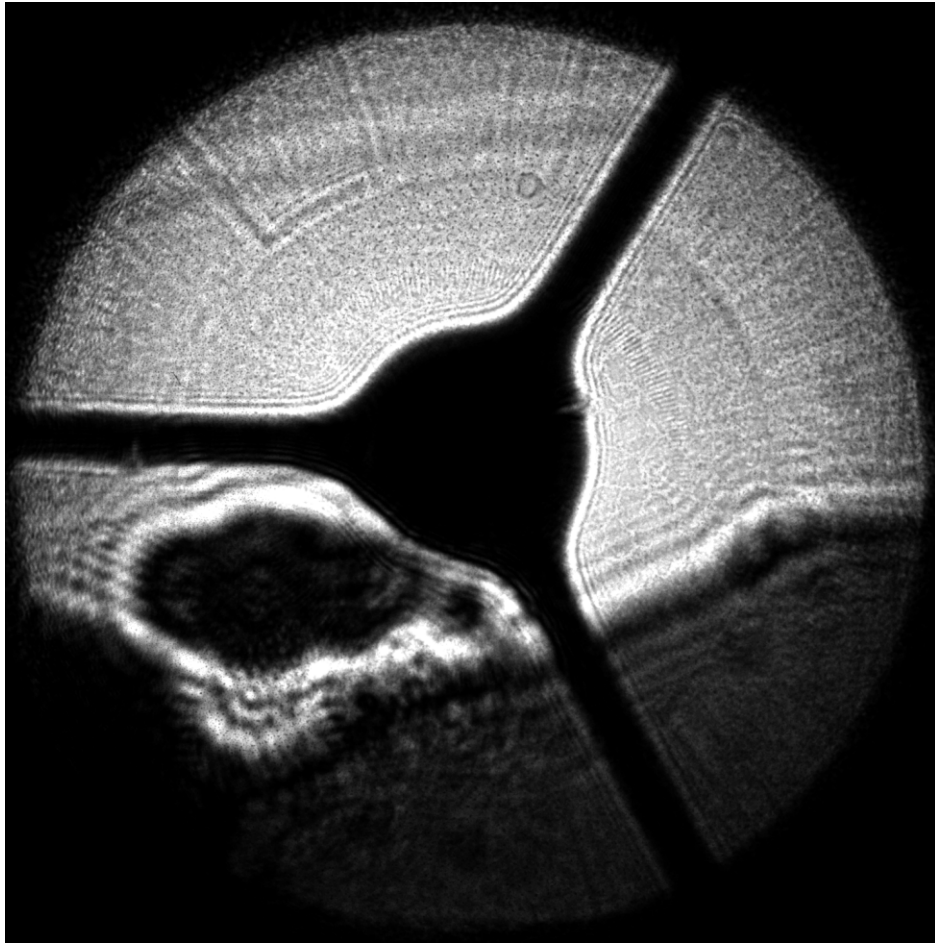


ZP: Diameter 160 μ m, Central stop 30 μ m, Outermost zone 30nm

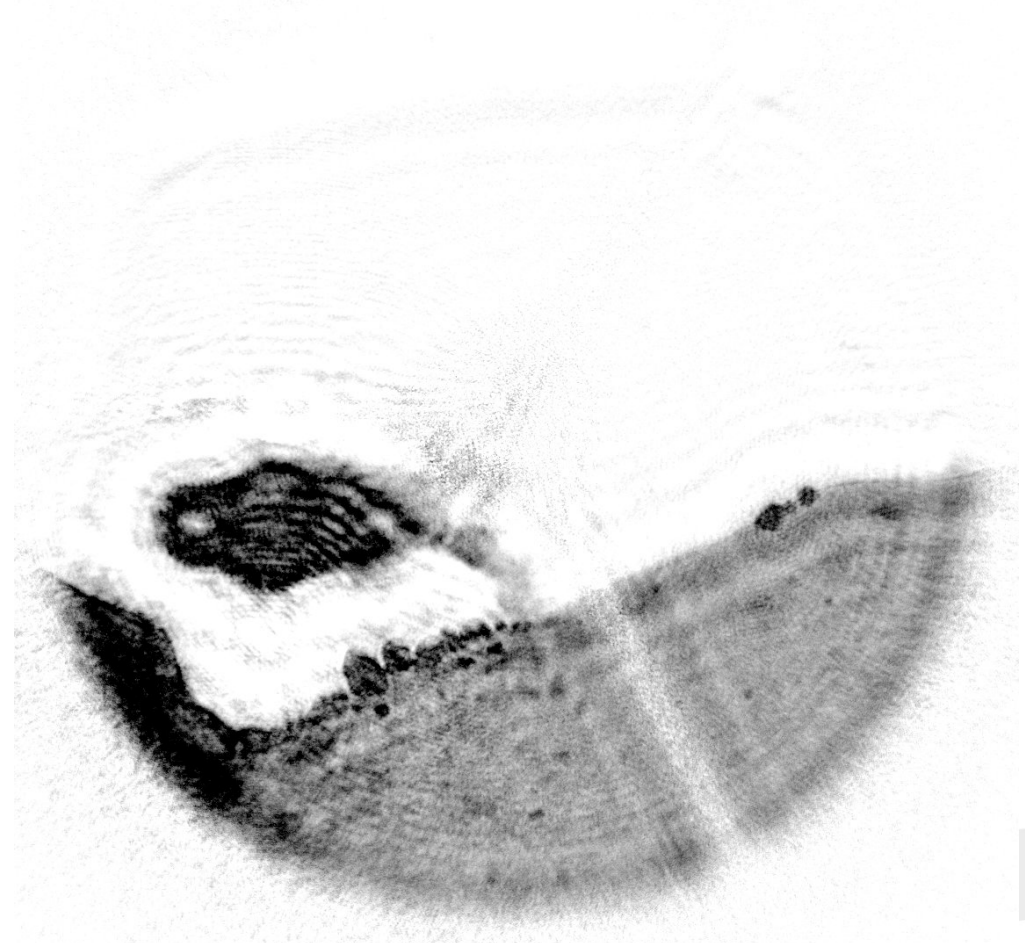
from the focus

Preliminary tests

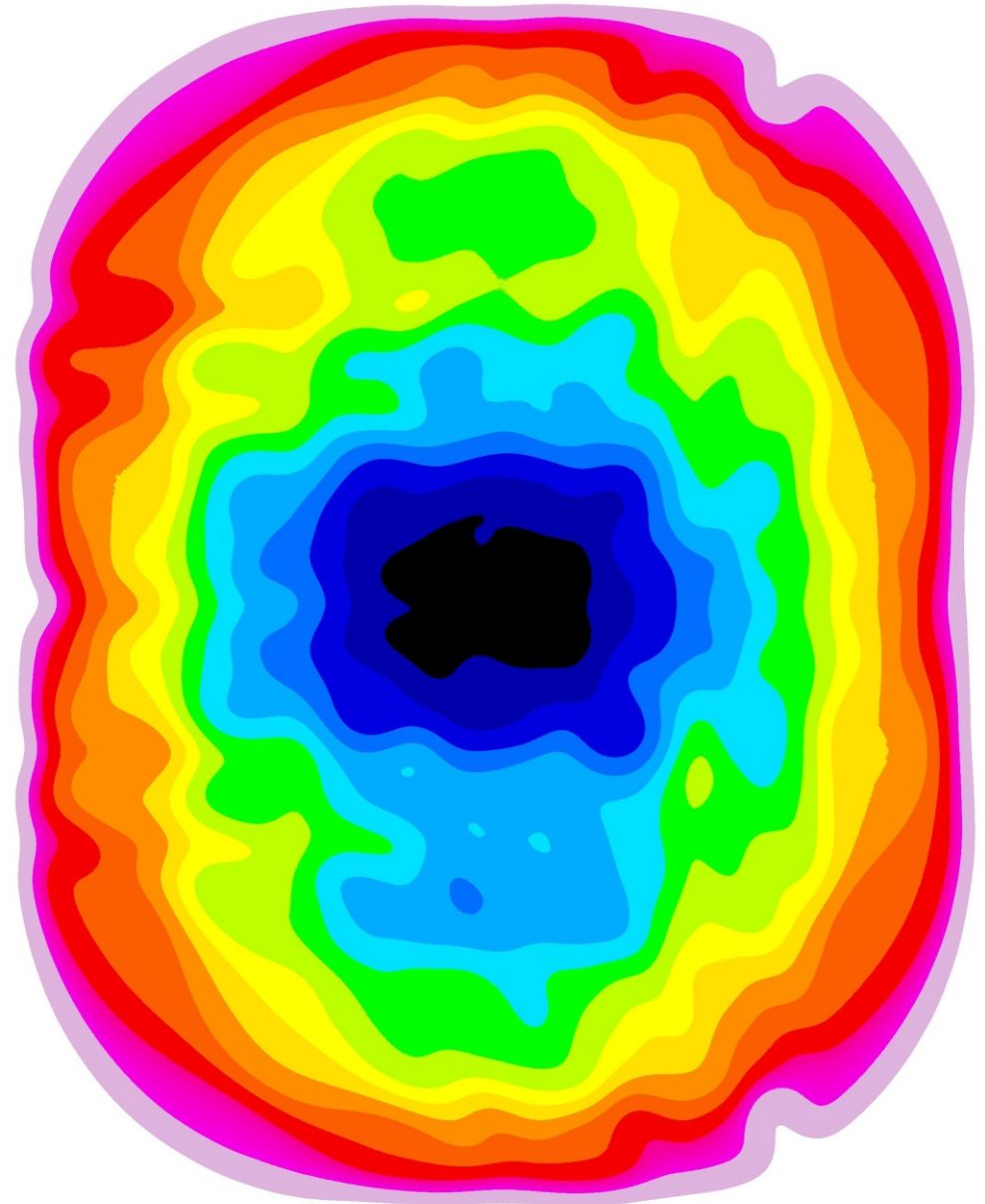
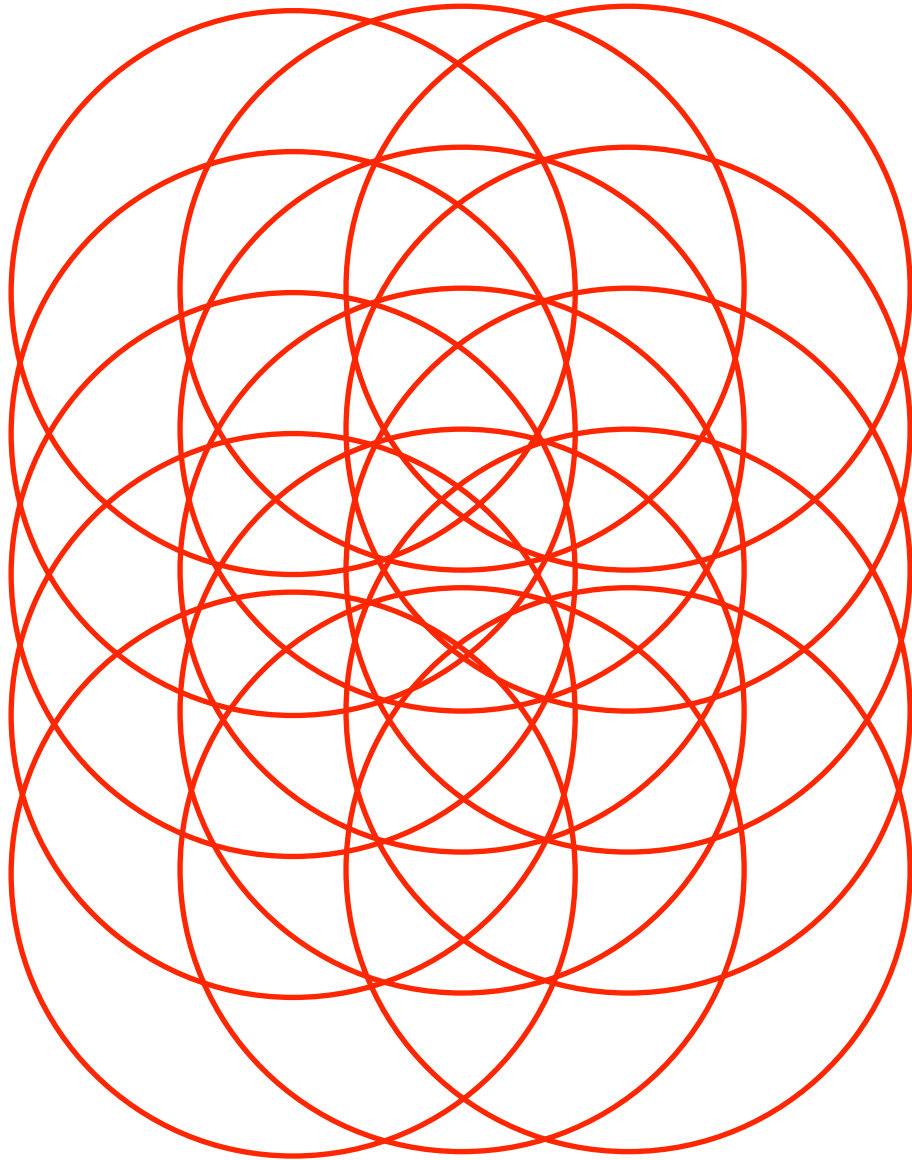
Diffraction pattern (through unfocused ZP)



Reconstruction

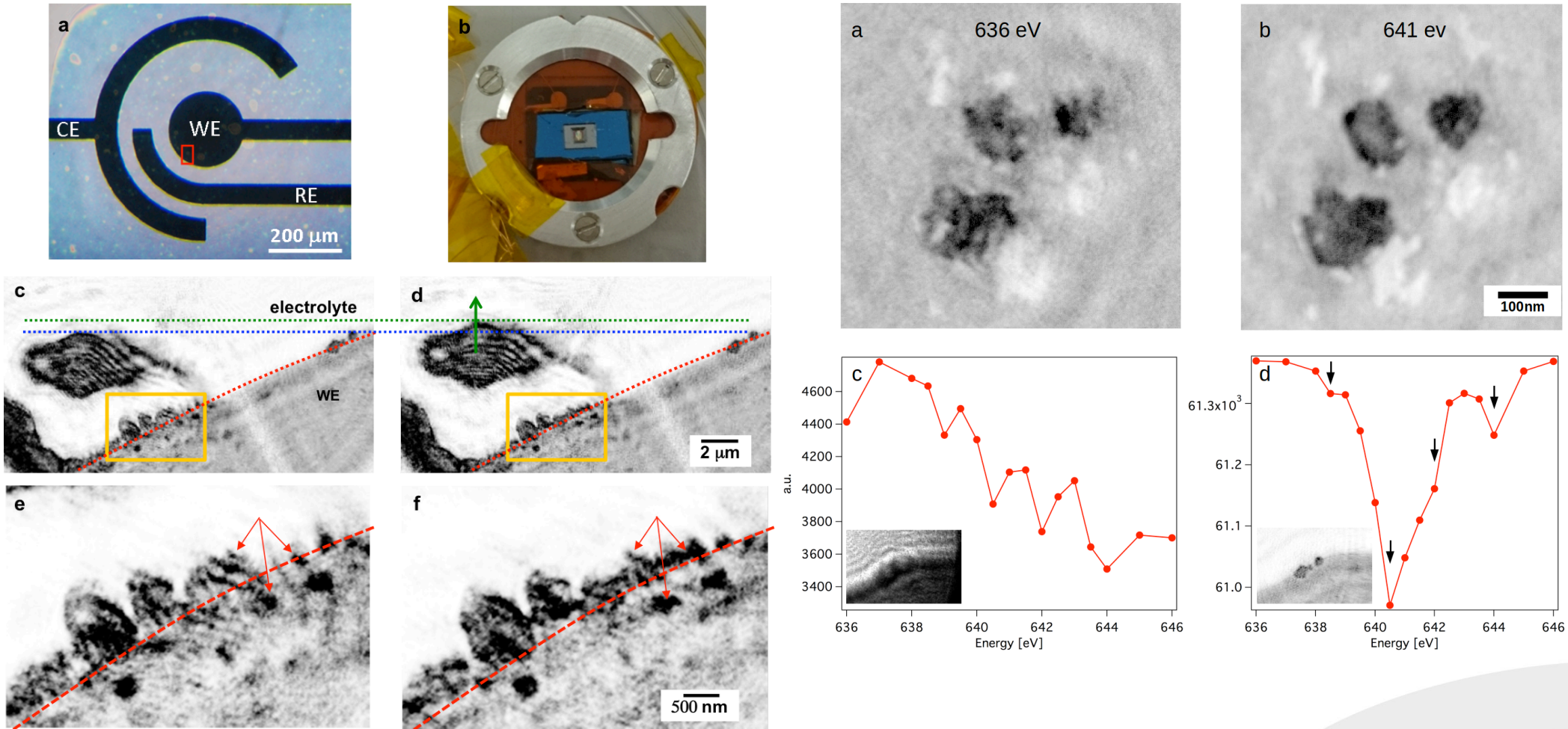


Scanning and oversampling

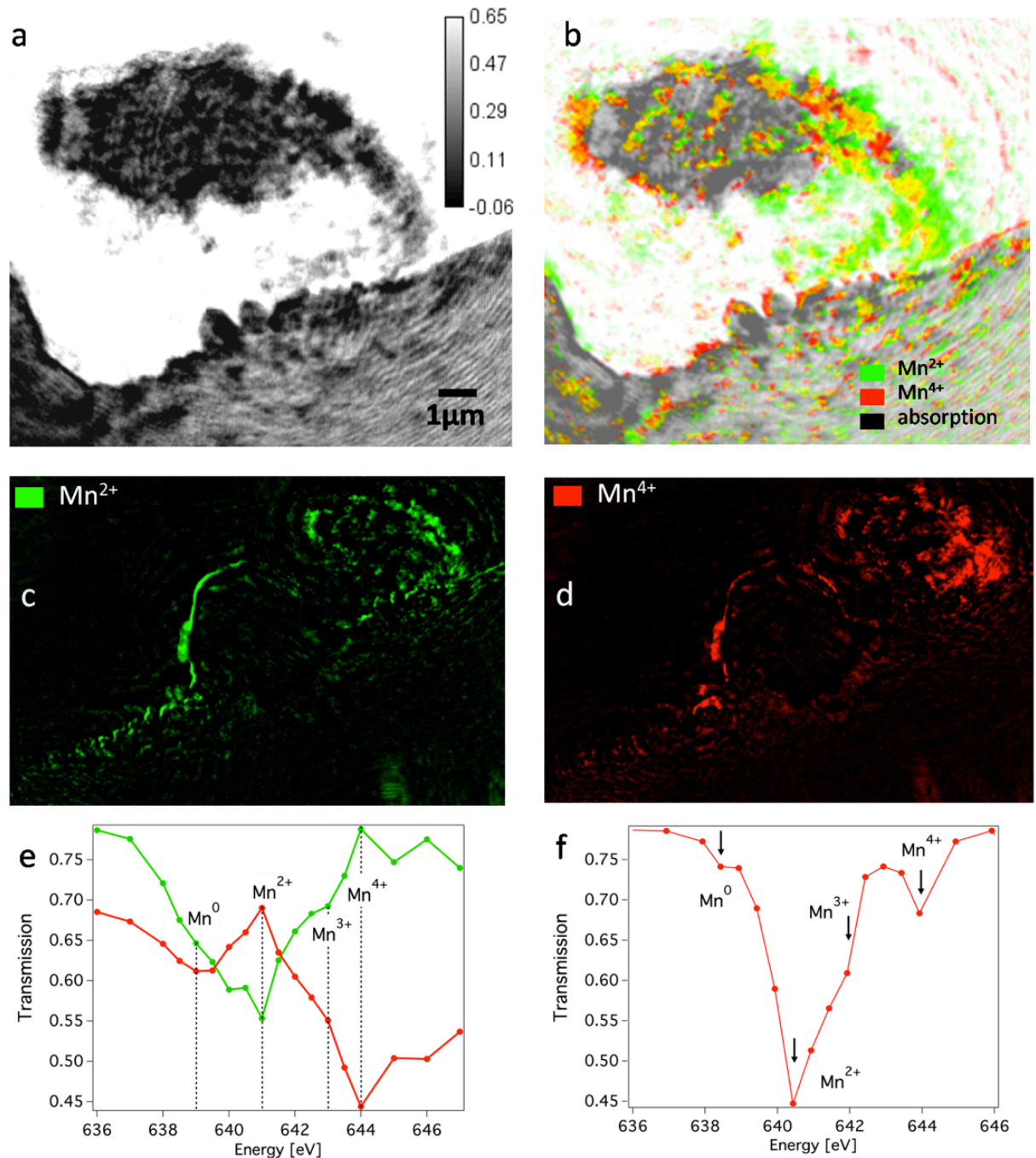


Electrochemical processes at local nanoscales by *in situ* soft FCDI imaging

TwinMic @ Elettra – SXRI @ Australian Synchrotron



Spectroscopy across Mn edge through Ptycography



Thank you!

